Particle Image Velocimetry for Microscale Blood Flow Measurement

Peter Vennemann

Particle Image Velocimetry for Microscale Blood Flow Measurement

Particle Image Velocimetry for Microscale Blood Flow Measurement

PROEFSCHRIFT

ter verkrijging van de graad van doctor
aan de Technische Universiteit Delft,
op gezag van de Rector Magnificus prof. dr. ir. J.T. Fokkema,
voorzitter van het College voor Promoties,
in het openbaar te verdedigen op maandag 21 april 2008 om 15:00

door

Peter Vennemann
Maschinenbauingenieur, Universität Duisburg-Essen,
geboren te Ascheberg (Westf.), Duitsland.

Dit proefschrift is goedgekeurd door de promotor:
Prof. dr. ir. J. Westerweel

Samenstelling promotiecommissie:

Rector Magnificus,	voorzitter
Prof. dr. ir. J. Westerweel,	Technische Universiteit Delft, promotor
Prof. dr. F.C.T. van der Helm,	Technische Universiteit Delft
Prof. dr. K.T. Kiger,	University of Maryland
Prof. dr. R.E. Poelmann,	Universiteit Leiden
Prof. Dr.-Ing. F. Peters,	Ruhr-Universität Bochum
Prof. dr. ir. A.A. van Steenhoven,	Technische Universiteit Eindhoven
Dr. N.T.C. Ursem,	Erasmus Medisch Centrum Rotterdam

The work presented in this thesis was supported financially
by the Technology-Foundation STW, project number DSF.5695.

ISBN 978-90-9022974-4

Printed by Gildeprint, Enschede

Contents

Preface iii

Summary v

Samenvatting vii

1 Introduction 1
- 1.1 Blood Flow and Fluid Mechanics . . . 1
- 1.2 Objectives and Scope . . . 4
- 1.3 Conclusions from this Thesis . . . 6

2 Blood Flow in Microvessels 9
- 2.1 Blood . . . 9
- 2.2 Microvessels . . . 11
- 2.3 Hemorheology . . . 12
- 2.4 Hemodynamics . . . 14

3 Measurement Techniques 17
- 3.1 Laser Doppler Velocimetry . . . 18
  - 3.1.1 Laser Doppler Imaging . . . 19
  - 3.1.2 Multi-Probes Laser Doppler . . . 20
  - 3.1.3 Profile Laser Doppler . . . 21
- 3.2 Laser Speckle Techniques . . . 22
  - 3.2.1 Laser Speckle Contrast Imaging . . . 22
  - 3.2.2 Time-Varying Speckle . . . 23
- 3.3 Particle Image Velocimetry . . . 25
- 3.4 Non-Optical Methods . . . 28
  - 3.4.1 Doppler Ultrasound Velocimetry . . . 28
  - 3.4.2 Ultrasound Particle Image Velocimetry . . . 30
  - 3.4.3 Nuclear Magnetic Resonance Imaging . . . 30
- 3.5 Conclusions . . . 32

4 Particle Image Velocimetry for Blood Flow **35**
4.1 Experimental Set-Up . . . 35
4.1.1 Accommodation of the Model Organism . . . 35
4.1.2 Optical components . . . 36
4.1.3 Illumination . . . 39
4.1.4 Seeding . . . 41
4.2 Triggered Measurement . . . 46
4.3 Non-triggered Measurement . . . 47
4.4 Image Evaluation . . . 48
4.5 Resolution Aspects . . . 52
4.6 Parallel Plane Measurement . . . 54
4.7 Reconstruction of the Third Velocity Component . . . 57
4.7.1 Method . . . 57
4.7.2 Accuracy and Sensitivity . . . 57

5 Applications **63**
5.1 Triggered Measurements . . . 63
5.1.1 Animals . . . 63
5.1.2 Experimental Set-Up . . . 63
5.1.3 Evaluation . . . 64
5.1.4 Results . . . 66
5.1.5 Discussion . . . 69
5.2 The Endothelin System in the Venous Clip Model . . . 69
5.2.1 The Venous Clip Model . . . 69
5.2.2 Measurements . . . 72
5.2.3 Results and Discussion . . . 72
5.3 Assessment of three Dimensional Flow . . . 75
5.3.1 Motivation . . . 75
5.3.2 Measurements . . . 75
5.3.3 Results and Discussion . . . 76

A Ethical Considerations **79**

Acknowledgments **103**

About the Author **107**

Preface

This thesis is based on collaborative research of the Laboratory for Aero- and Hydrodynamics (Delft Technical University), the Department of Anatomy and Embryology (Leiden University Medical Center), and the Department of Obstetrics and Gynecology (Erasmus Medical Center Rotterdam) from March 2003 to April 2007.

The results of this work were published in the following journal papers:

- P Vennemann et al., J Biomech, 39:1191-1200, 2006
- P Vennemann et al., Exp Fluids, 42:495-511, 2007
- BCW Groenendijk et al., J Vasc Res, 45:54-68, 2008

Summary

During the last two decades the influence of fluid mechanical forces on the development and regulation of the circulatory system came into focus of biomedical research. The further investigation of the mechanisms of blood flow triggering the development, the regulation, and also the pathology of the circulatory system requires detailed measurements of the wall shear stress. Wall shear stress can hardly be measured in vivo directly, but can be derived indirectly from spatial velocity data. Therefore, the principal goal of the research described in this thesis was the development and application of a new optical technique that would be suitable for measuring the velocity distribution in small blood vessels.

The method of particle image velocimetry uses the motion of small tracer particles to determine the fluid velocity with a high spatial and temporal resolution that is not found in other existing methods. Although blood contains particles in the form of red blood cells, it is shown that the requirements for the spatial resolution of the measurement and for a homogeneous distribution of the particles in the fluid make them unsuited as tracer particles in most cases. A novel approach was to use small, artificial, fluorescent particles, either in the form of solid particles or liposomes, with a diameter less than 1 μm and a hydrophilic coating that makes the particles "invisible" to the biological model. Using a fluorescence microscope it is possible to record only the optical signal emitted by the fluorescent tracer particles. This approach establishes a significant increase of the signal-to-noise ratio and improvement of the measurement accuracy.

The particle image velocimetry method was applied to measurements of microscale blood flow in both vitelline vessels and the heart of a chicken embryo. This biological model was chosen for its optical transparency and its relevance in biological and medical studies. The measurements demonstrated that quantitative measurements of the wall shear stress can be obtained. The wall shear stress is derived directly from the measured shear rate and local viscosity of the blood plasma (which is essentially a Newtonian fluid, i.e. with constant viscosity), whereas in other methods the wall shear stress is derived indirectly, from the measured (or estimated) volume flow rate or centerline velocity and vessel diameter, and typically received as an averaged quantity over an extended probe volume. It is demonstrated that particle image velocimetry yields quantitative results that are capable of detecting significant changes under varying physiological conditions.

The capability of particle image velocimetry to determine the flow field as a whole makes it very suited for measurements in complex geometries, such as the beating embryonic chicken heart. Measurements in a HH-stage 17 chicken embryo showed that the highest value of the wall shear stress occurs at the inner curved wall. Typically, the highest shear stress in curved tubes occurs at the outer curved wall, but it appears that the measurement result is in agreement with the theory of flow in a tube bend at low Dean numbers (dominance of viscous forces over inertia). Also, this observation is in agreement with expression data of shear-responsive genes. However, such expression data do not provide access to the flow, and therefore it was possible to provide an explanation of the gene expression in the inner curved wall. This demonstrates the significance of using particle image velocimetry which provides quantitative flow data that are temporally and spatially resolved.

Further research requires a volumetric measurement rather than a planar measurement. Therefore, this thesis closes with extended measurements in a volumetric domain by using a scanning measurement plane. A numerical reconstruction method is used for deriving the fully three dimensional velocity distribution in the beating, embryonic heart.

Samenvatting

Gedurende de afgelopen twee decennia heeft zich op het gebied van biomedisch onderzoek een grote belangstelling ontwikkeld voor de invloed die bloedstroming uitoefent op het cardiovasculaire systeem. Een voorwaarde voor vergaand onderzoek naar de wijze waarop de mechanische kracht van stromend bloed de ontwikkeling, regulatie en pathologie van het cardiovasculaire systeem bepaalt, is een nauwkeurige meting van de wandschuifspanning. In vivo kan de wandschuifspanning nauwelijks rechtstreeks worden gemeten, maar ze kan worden afgeleid uit een ruimtelijk snelheidsveld. Derhalve is de kerntaak van het hier beschreven onderzoek de ontwikkeling en toepassing van een nieuwe optische meetmethode die geschikt is voor het meten van de snelheidsverdeling in kleine bloedvaten.

De meettechniek "particle image velocimetry" is gebaseerd op het volgen van kleine deeltjes in een stroming. Deze techniek is in staat de beweging van een stroming met een ruimtelijke en tijdelijke resolutie weer te geven, die hoger is dan met andere bestaande methodes. Hoewel bloed al deeltjes in de vorm van rode bloedcellen bevat, wordt aangetoond dat deze meestal niet bruikbaar zijn om een hoge ruimtelijke meetresolutie te bereiken op iedere locatie in de stroming. Een nieuwe aanpak is het gebruik van fluorescente deeltjes, of in de vorm van vaste deeltjes of in de vorm van liposomen, met een diameter van minder dan 1 μm en met een hydrofiele laag die de deeltjes "onzichtbaar" maakt voor het biologische model. Met een fluorescentiemicroscoop is het mogelijk alleen het optisch signaal op te nemen dat door de deeltjes wordt verstrooid. Met deze methode wordt een duidelijk verbeterde signaal-ruisverhouding en een hogere meet-nauwkeurigheid bereikt.

De particle image velocimetry methode wordt toegepast bij metingen van een bloedstroming in vitellinevaten en in het hart van een kippenembryo. Dit biologisch model is gekozen omdat het optisch goed toegankelijk is en veel wordt gebruikt in biologisch en medisch onderzoek. Metingen tonen aan dat kwantitatieve meetresultaten voor de wandschuifspanning kunnen worden bereikt. De wandschuifspanning wordt direct afgeleid uit de gemeten afschuifsnelheid en de lokale viscositeit van het bloed-plasma (bij benadering een Newtonse vloeistof). Met andere methodes wordt de wandschuifspanning indirect afgeleid uit de gemeten volumestroom of de middellijnstroomsnelheid en de vatdiameter, hetgeen een middeling over het bloedvatvolume impliceert. Dit onderzoek toont aan dat particle image velocimetry significante veranderingen onder variërende fysiologische omstandigheden kan detecteren.

De mogelijkheid om met particle image velocimetry het stromingsveld in het geheel te bepalen maakt deze meetmethode bijzonder geschikt voor metingen in complexe geometrien zoals het kloppend embryonaal kippenhart. Metingen in een HH-stadium 17 kippenembryo laten zien dat de hoogste wandschuifspanning in de binnenbochten te vinden is. Hoewel de hoogste schuifspanning bij technisch relevante stromingen gebruikelijk in de buitenbochten te vinden is, blijken de meetresultaten overeen te komen met de theorie van stromingen door een buis bij lage Dean getallen (dominantie van viskeuze krachten over inertie). Deze observatie komt ook overeen met gen-expressie data van genen die voor schuifspanning gevoelig zijn. Gen-expressie data geeft echter geen toegang tot informatie over de stroomsnelheid. Dit onderstreept de relevantie van het meten van kwantitatieve stromingsdata met ruimtelijke en tijdelijke resolutie.

Voor verder onderzoek zijn bij voorkeur metingen in een volumen nodig in plaats van metingen binnen een meetvlak. Daarom wordt dit proefschrift afgesloten met een meting in drie dimensies. Door middel van een scanning methode zijn metingen in een aantal parallelle vlakken verricht. Een numerieke reconstructie methode wordt gebruikt om een complete driedimensionale snelheidsverdeling in een kloppend embryonaal kippenhart af te leiden.

Chapter 1

Introduction

1.1 Blood Flow and Fluid Mechanics

In recent years, fluid mechanical forces have been recognized as a major influential factor in several biomedical fields like atherosclerosis, angiogenesis and cardiogenesis. A keyword query at one of the largest biomedical databases for scientific journal publications (figure 1.1) stresses how fluid mechanics comes into focus of biomedical research. The fraction of articles that contain the word "blood" in the title or the abstract has remained almost constant over the last thirty years. In contrast, conjunctions of "blood" with flow related terms like "velocity" or "shear stress", match a strongly growing fraction of articles (figure 1.1a). Figure 1.1b illustrates the historical development of relating the fluid mechanical property "shear stress" to biomedical terms like "endothelium", "atherosclerosis", "gene expression", and "angiogenesis". The relation between fluid mechanics and biology was laid in the mid eighties and is a topic in a constantly growing number of publications.

In 1977, about ten years before the influence of fluid mechanics on the development and regulation of the circulatory system was realized by a wide range of scientists and the number of publications in this field started to increase, Bugliarello [24] introduced the term "bio-fluid mechanics" in a general sense. He identified a number of physiological systems and processes with significant flow implications, like: tissue formation, respiration, food processing, blood circulation, hearing, propulsion, joint lubrication, heat regulation, cell contraction, cytoplasmic streaming, gene readout, intercellular communication, and so forth. He also listed the interaction of groups of organisms like fish schools and plants. He further suggested a systematic organization of these topics and motivated to use bio-fluid mechanics in two directions: to understand biological processes and to inspire engineering (bionics).

Since then, blood flow related bio-fluid mechanics has attracted the most attention. This is not surprising. Searching the pubmed database for the term "cardiovascular" in the title or the abstract returns more than 14.000 hits for the year 2007 alone. This enormous scientific interest in the cardiovascular system in general becomes obvious when

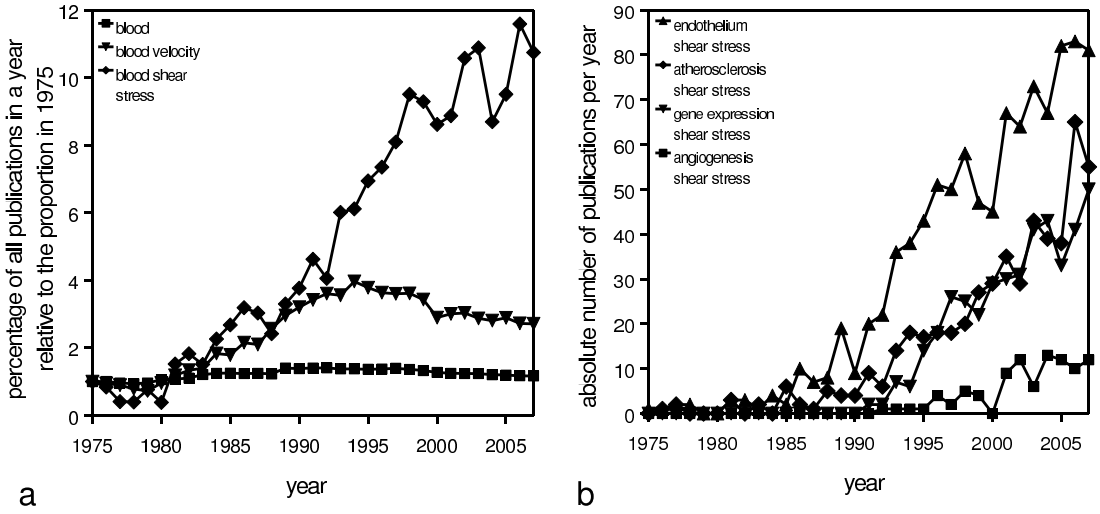

Figure 1.1: Results of a keyword query at `www.pubmed.gov`, limited to the fields "Title" and "Abstract". a) Results for the single word "blood" and for conjunctions with flow related terms "velocity" and "shear stress". The ordinate shows the percentage of all articles published in a particular year that match the query, divided by that percentage in 1975. b) Total number of articles per year that match queries with conjunctions of the fluid mechanical term "shear stress" and biomedical terms that are supposed to be affected by shear stress.

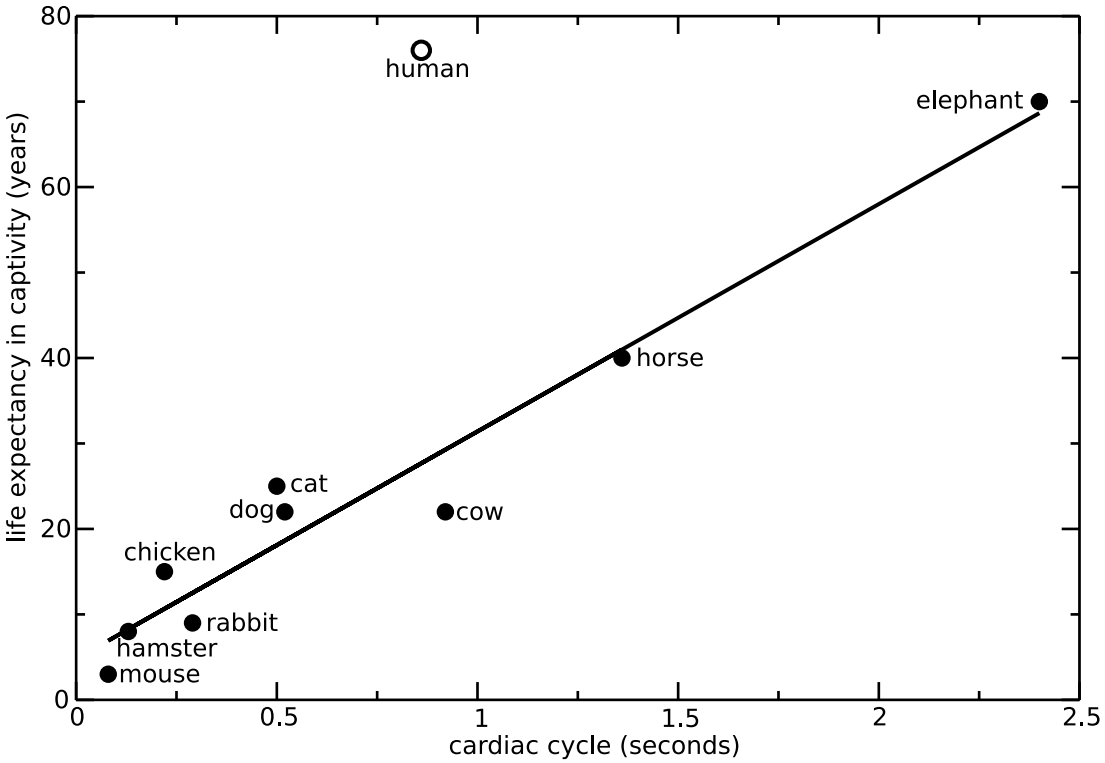

Figure 1.2: Relationship between the life expectancy (in captivity) of various animals and the duration of their cardiac cycle at rest [114]. Data for various animals appear to fall on a straight line, with humans clearly deviating with respect to other creatures. Life expectancy and heart rate are related to the body mass in the same manner as standard metabolic rate is related to body mass (Kleiber's quarter power law [89]).

we compare the demands on the human circulatory system with various animals. Figure 1.2 visualizes the relation between life expectancy (in captivity) and the duration of the cardiac cycle in a number of animals (mainly mammals) [114]. This relation implies that the total number of heart beats is approximately constant [93, 114]. Humans take a rather exceptional position in the diagram. This may indicate that the human circulatory system is extraordinarily burdened. Therefore it may not be surprising that cardiovascular diseases are presently the leading cause of death [123].

The investigation of the relation between fluid forces and the development of the cardiovascular system or its diseases, requires detailed knowledge of the blood flow. Especially atherosclerosis research needs spatially resolved measurements of blood velocity distributions to determine the influence of flow induced wall shear stress and instantaneous flow patterns. The derivation of shear stress is also inevitable for researching the role of fluid mechanical stimuli in cardiogenesis and angiogenesis. The assessment of wall shear stress in vivo is reviewed in detail by Reneman et al. [139]. Due to non-Newtonian blood properties, elastic vessels, pulsatile flow, and varying

geometry, Reneman et al. conclude, shear stress can not be calculated on the basis of diameter and centerline velocity using Poiseuille's law. They report that wall shear rate values derived from measured velocity profiles are substantially different from those calculated with the assumption of a parabolic profile. According to Reneman et al. mean wall shear stress is also far from constant along the arterial tree as predicted by Murray's law [122].

1.2 Objectives and Scope

This thesis focuses on the measurement of blood flow in small blood vessels and the embryonic chicken heart in particular. The chicken embryo is used for decades in descriptive and experimental embryology as well as in work on viruses and cancer [68]. In contrast to mammalian embryos, the handling of avian embryos is much easyer. Optical access can easily be created. Furthermore, chicken embryos are inexpensive and the early cardiac development of human and chicken embryos is comparable [155]. The main reason for choosing the chicken embryo as a test case for particle image velocimetry measurements is, that our cooperating research groups - the Department of Anatomy and Embryology (Leiden University Medical Center), and the Department of Obstetrics and Gynecology (Erasmus Medical Center Rotterdam) - are using the chicken embryo for their work on the hemodynamic effects of manipulated blood flow. Their utilization of the chicken embryo as an animal model traces back to the work of Hogers [74].

A direct link between physiological observations and flow induced mechanical forces can only be found by determining those forces. The principal aspect that needs to be measured is the wall shear stress, which is related to the differentiation and regulation of tissue cells. Values for the wall shear stress, τ, can be extracted from a velocity field by the calculation of the wall-normal velocity gradients, $\partial u/\partial n$:

$$\tau = \eta \frac{\partial u}{\partial n}, \tag{1.1}$$

where η is the dynamic viscosity of the fluid. The viscosity can be a function of the shear rate (as is the case for blood, see section 2.1). The accurate derivation of wall shear stress values from the velocity gradients near the flow boundary demands a high spatial resolution. Because blood is a non-Newtonian fluid, i.e. the viscosity is a function of the shear rate and the hematocrit value, the local value of the viscosity is a function of the distance from the wall (see section 2.3 about hemorheology and section 2.4 about hemodynamics), and therefore the derivation of the wall shear stress from equation 1.1 is strongly determined by the resolution of the velocity measurement. When absolute values for the wall shear stress are desired (in contrast to relative, or comparative measurements), at least two adjacent velocity measurement points within the cell free layer (section 2.4) are required. This claim leads to a resolution demand of the order of one micrometer. Among the measurement techniques applied to blood flow in

vivo, particle image velocimetry or related particle tracking techniques are presently the most promising techniques to achieve the required spatial resolution (see chapter 3). Particle image velocimetry is widespread in engineering applications, but requires special considerations and methodologies in order to be utilized for in vivo studies in medical and biological research. The adaptation and characterization of particle image velocimetry for biomedical research (chapter 4), as well as the application on actual biomedical problems (chapter 5) is the main subject of this thesis.

The remainder of this thesis is partially composed of previously published articles. Although substantially expanded and rearranged, the chapters 2, "Blood Flow in Microvessels", and 3, "Measurement Techniques", have their origin in a review article published in Experiments in Fluids [176]. Chapter 2 is meant to highlight special fluid mechanical issues related to blood flow. Cardiovascular flow differs from many laboratory and engineering applications especially by the complex fluid properties and the complex mechanics and surface properties of the blood vessels. For the correct interpretation of the measured velocity data, some awareness about the specific problems associated with blood flow is essential. In section 2.1, "Blood", the components of blood are characterized in a fluid mechanical sense. Also the advantages and limitations of different natural tracer particles such as platelets and erythrocytes will emerge in this section. This topic is deepened in section 4.1.4 when seeding for particle image velocimetry is treated. An example for using erythrocytes as tracer particles is given in section 5.2, "The Endothelin System in the Venous Clip Model", which is also part of a publication in the Journal of Vascular Research [65]. In section 2.2, "Microvessels", the inner surface of the vessel wall is addressed. It will become clear that the inner lumen boundary of a blood vessel can not be taken as a wall with a distinct surface, but that it should rather be understood as dynamic layer with radially variable axial permeability. Section 2.3, "Hemorheology", provides information about the origin and the mechanisms of the non-Newtonian behavior of blood. In section 2.4, "Hemodynamics", guidelines are collected for deciding how far non-Newtonian effects should be accounted for. Chapter 3, "Measurement Techniques", comprises a review of methods for the measurement of blood flow and their suitability for measuring wall shear stress. The remaining two chapters 4, and 5, form the main subject of this thesis, the combination of the advantages of correlation based image evaluation and various fluorescent tracer particles that are chosen to adapt to the individual demands of the particular application. Chapter 4, "Particle Image Velocimetry for Blood Flow", presents the progress made in the scope of the present work from a technical point of view[1]. In addition, chapter 5, "Applications", documents the application of various approaches on actual biomedical questions. Parts of chapter 4 and section 5.1, "Triggered Measurements", have their roots in a Journal of Biomechanics publication

[1] All necessary evaluation software was combined in an intuitively usable computer program. It can be started on any personal computer by executing the line `javaws http://www.jpiv.vennemann-online.de/jpiv.jnlp` in a terminal window (e.g. "cmd" for Windows or "bash" for Linux). The only prerequisites are a working internet connection and that a java runtime environment (JRE) is installed on the computer.

[175]. Section 4.3 about circumventing triggering, section 4.6 about scanning particle image velocimetry, and section 4.7 about the reconstruction of the three dimensional flow field in the embryonic heart cover recent results that have not been published. The corresponding application example is described in section 5.3.

1.3 Conclusions from this Thesis

Each of the chapters outlined above deals with a separate sub-topic and the end of each chapter summarizes the conclusions from that particular chapter. Here the main conclusions of the work in this thesis are summarized.

The principal goal of the research described in this thesis was the development and application of a new optical measurement technique that would be suitable for in vivo measurements of the local wall shear stress (section 1.2). From a review of methods for the measurement of blood flow and their suitability for measuring wall shear stress (chapter 3) it can be concluded that the key for achieving this goal is to combine the advantages of correlation based image evaluation and various fluorescent tracer particles that are chosen to adapt to the individual demands of the particular application. In section 4.1.4 and 4.5 it is shown that erythrocytes are unsuited as tracer particles in most cases to fulfill the requirements for the spatial resolution of the measurement and for a homogeneous distribution of the tracer in the fluid. A novel approach was to use small fluorescent particles, either in the form of solid particles or liposomes, with a diameter less than 1 μm and a hydrophilic coating that makes the particles "invisible" (or "stealth") to the biological model. This approach establishes a significant increase of the signal-to-noise ratio and of the measurement accuracy.

Chapter 4 documents continuous progress in two directions. Firstly, the mechanical complexity of the measurement system is reduced, and secondly, the usable data output is increased. Both are important steps from an experimental set-up that is used to prove the principle to a diagnostics tool for productive use. Circumventing triggering (section 4.3) decreased the technical complexity, and increased the data rate as well as the optical quality. The data rate could be increased, because the acquisition frequency was not limited by the heart rate anymore. For triggering, the tip of an ultrasound velocimeter had to be placed next to the dorsal aorta of the embryo (section 4.2). After dropping the triggering, the embryo could be covered with a glass slide instead of an oil layer, which improved the optical quality. As will be explained in section 4.1.1 the glass cover also enhanced control over desiccation and temperature, therefore extending the possible measurement duration. Improved seeding (section 4.1.4) also contributed to an extended maximum measurement duration.

The particle image velocimetry method was applied to measurement of micro-scale blood flow in both vitelline vessels and the heart of a chicken embryo (chapter 5). The measurements demonstrate that quantitative measurements of the wall shear stress can be obtained. The wall shear stress is derived directly from the measured shear rate and local viscosity of the blood plasma (which is essentially a Newtonian fluid, i.e.

with constant viscosity), whereas in other methods the wall shear stress is obtained indirectly, from the measured (or estimated) volume flow rate and vessel diameter, and typically obtained as an averaged quantity over an extended probe volume. In section 5.1 it is demonstrated that particle image velocimetry yields quantitative results that are capable of detecting significant changes under varying physiological conditions. The capability of particle image velocimetry to determine the flow field as a whole makes it very suited for measurements in complex geometries, such as the beating embryonic chicken heart. Particle image velocimetry in a HH-stage 17 chicken embryo (see section 5.1) showed that the highest value of the wall shear stress occurs at the inner curved wall. Typically, the highest shear stress in curved tubes occurs at the outer curved wall, but it appears that the measurement result is in agreement with theory for flow at low Dean numbers (section 5.1.5). Also, this observation is in agreement with expression data of shear-responsive genes. However, such expression data do not provide access to the flow, and therefore it was possible to provide an explanation of the gene expression in the inner curved wall. This demonstrates the relevance of using particle image velocimetry which provides quantitative flow data that are temporally and spatially resolved.

Further research requires the measurement of wall shear stress over extended domains. This requires a volumetric measurement rather than a planar measurement. The enhancements of the experimental set-up mentioned above (increased data rate, improved optical quality, and extended maximum measurement duration) in conjunction enabled successive measurements at multiple planes (section 4.6), and finally the reconstruction of a three dimensional flow field (section 4.7). This in turn forms the basis for deriving shear rate patterns of unprecedented accuracy [130] (section 5.3) that can be compared to gene expression patterns like published by Groenendijk et al. [64].

Chapter 2

Blood Flow in Microvessels

Fluid mechanically relevant characteristics of blood and blood flow are bundled in this chapter. Section 2.1 summarizes the composition of blood. Already having the application of particle image velocimetry in mind, the usability of different cells as tracer particles, and their influence on the hemorheology are anticipatorily addressed. In section 2.2 important background information about the flow boundary is summarized. To establish a clear border between the last two sections "Hemorheology", and "Hemodynamics" is difficult. Both disciplines deal with the movement of blood. Here, section 2.3, "Hemorheology", focuses on the material-specific properties of blood. This includes the origin and mechanism of its non-Newtonian behavior, for example. Section 2.4,"Hemodynamics" focuses on the consequences of the non-Newtonian properties on the flow, and how to deal with it.

2.1 Blood

Blood is a complex fluid that consists of a continuous phase, the plasma, containing proteins, nutrients, and hormones and larger particles of order one to ten micrometer (e.g. red and white blood cells, platelets). Compared to most technically relevant fluids, blood exhibits some intricate behavior. Blood as a whole reacts mechanically as well as chemically with its environment. At the same time the components of blood react mechanically and chemically with each other. The mechanically most relevant components of blood are the plasma and the red blood cells or erythrocytes.

Figure 2.1 shows photographs of unprocessed, human blood taken with a simple light microscope at a magnification of 0.16 μm per pixel. The left photo shows a layer of about 20 μm thickness. The tendency of the erythrocytes to stick together in aggregates is clearly visible. Those aggregates are widely referred to as rouleaux, because of their resemblance with a stack of coins. The right photo in figure 2.1 shows erythrocytes in a layer of about 5 μm thickness. Their diameter is around 7 μm. The rim of the flat, bi-concave shaped cells has a thickness of about 2 μm. The volume fraction of erythrocytes (hematocrit value) is about 45 % (this is around $5 \cdot 10^6$

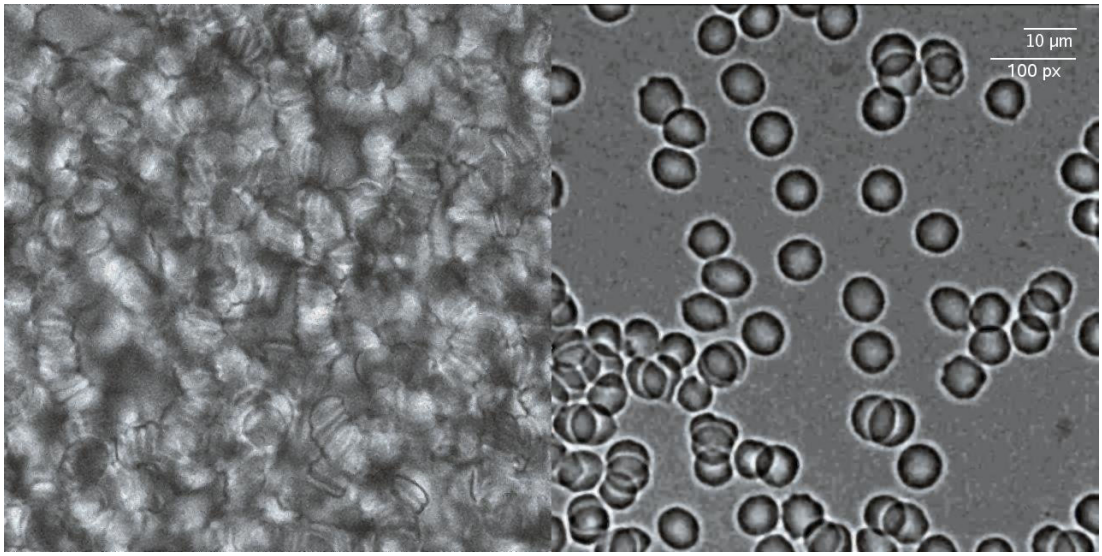

Figure 2.1: Unprocessed human blood (courtesy of P.V.) seen through a light microscope (40× magnification or 0.16 μm per pixel). The left photograph shows a layer of about 20 μm thickness. Rouleaux formation is clearly visible. The right photograph shows a layer of about 5 μm thickness.

cells per μl), but varies with age and gender [145]. Erythrocytes can be used as flow tracers. Section 3.3 gives examples for the use of erythrocyte tracers in the literature. Advantages and disadvantages are discussed in section 4.1.4. A practical example is given in section 5.2.

Blood contains a small number ($4 \cdot 10^3$ to $10 \cdot 10^3$ per μl) of white blood cells, or leukocytes, that are an essential part of the immune system [145]. Leukocytes are larger than erythrocytes. Of fluid mechanical interest is their ability to roll over and to stick to the inner surface of blood vessels [95].

Another essential component of blood are platelets, or thrombocytes. Thrombocytes have a length of 1 to 4 μm and a thickness of 0.5 to 0.75 μm [145]. Because of their small size and large number ($150 \cdot 10^3$ to $350 \cdot 10^3$ per μl) they can be used as tracer particles for velocity measurements [156, 163–165]. They are particularly useful for measurements in the plasma rich region near the vessel wall. This layer might be erythrocyte depleted due to the Fåhraeus-Lindquist effect [3, 7, 13, 136, 150]. Uijttewaal et al. [170, 171] showed that platelets experience a reversed Fåhraeus-Lindquist effect and concentrate in the erythrocyte depleted layer. While erythrocytes can be used as tracers right away, platelets are not that easily visualizable and need to be fluorescently labeled in vivo. They do not reach the visibility of artificial tracer particles, however.

Plasma consists mainly of water. A mass fraction of about 8 % of different proteins raise the viscosity of plasma to almost twice the viscosity of water [70]. Among the

Figure 2.2: Electronmicrographs of the glycocalyx layer in a rat left ventricular myocardial capillary (figure adapted from [173]).

plasma-proteins, fibrinogen can be of fluid mechanical relevance. The clotting-ability of blood rests on this protein that activates and attaches thrombocytes. Plasma also contains a number of electrolytes, mainly the ions of dissolved sodium chloride [145].

2.2 Microvessels

The geometry of the cardiovascular system is strongly three-dimensional (e.g. the heart and aortic arch) and involves multiple scales that range from the aorta (with a diameter of about 2 cm) over the arteries and veins (with diameters in the millimeter range) down to arterioles, venules, and capillaries with diameters of less than eight micrometers (see table 2.1). Blood vessels with a diameter significantly smaller than one millimeter are referred to as microvessels throughout this thesis.

The walls of blood vessels have a complex inner surface structure. The vessels are lined with endothelial cells that are covered with a gel-like permeable layer of sugar-like molecules, which is referred to as the glycocalyx layer [173]. The glycocalyx layer has an estimated thickness between 10 and 400 nm (figure 2.2). The function of the glycocalyx is presently unknown, but it may be involved in the regulation of the total blood flow and protect the endothelial cells against high flow shear rates that may rupture the cells. The glycocalyx may also play a role in reducing the friction of the transport of erythrocytes through very small capillaries [54].

The flow through microvessels can be rather complex. Not only are we dealing with non-stationary or pulsating flow, but also with flows through tubes with deformable

elastic walls. A detailed discussion of the fluid-structure interaction as a result of pulsating flow in flexible tubes would fall outside the scope of this work. Detailed information may be obtained from the book by Zamir [188].

2.3 Hemorheology

Regularly appearing review articles may be consulted as an entry point into this topic [37–39, 102, 133, 180].

Already Poiseuille investigated the flow of blood through capillaries. He tried to verify his law for laminar flow for different liquids including blood [131, 132]. Poiseuille used defibrinated blood for his experiments to prevent coagulation. The flow through his horizontal glass capillaries was irregular, however. Poiseuille (quoted by Ewald [53] and Lewy [94]) concluded, that fibrinogen is necessary to hold the erythrocytes apart, and thus defibrinated blood can not flow through capillaries. At the beginning of the twentieth century scientists related the varying viscosity of blood to the number of erythrocytes [48] or the hematocrit [39, 167]. Still, measurements did not verify Poiseuille's law. Chien in 1970 finally solved the irregularities by measuring a shear stress dependent viscosity and by relating this non-Newtonian behavior to the aggregation and deformation of erythrocytes [33]. Figure 2.3 illustrates this effect by comparing the shear dependent viscosity of normal blood with the viscosity of blood where the cells do not aggregate (by addition of albumin) and blood with cells that can also not deform (hardened cells). The increased apparent viscosity of normal blood at very low shear rates is therefore attributed to the agglomeration of cells, while the lowered viscosity at high shear rates is attributed to the deformability of the cells.

It should be mentioned that the tendency of red blood cells to aggregate varies among different species. For example, blood from horses show a stronger tendency to aggregate than human blood, while rat blood exhibits only negligible aggregation [8, 13]. Furthermore, avian blood exhibits a different rheology from mammalian blood. Due to a lower aggregation tendency, flow profiles are closer to profiles of Newtonian fluids than human blood flow profiles [81]. The lower aggregation tendency can be explained by the ellipsoidal shape of avian blood cells, in contrast to the biconcave shape of human erythrocytes. This in turn is due to the fact that avian erythrocytes are nucleated , in contrast to non-nucleated mammalian erythrocytes [61]. Additionally to the shear rate, apparent blood viscosity is a function of the tube diameter (figure 2.4). This effect is strongly related with the Fåhraeus-Lindquist effect [136]. In-vivo values for the apparent viscosity may be determined optically by calculating the hematocrit from the optical density of flow images [103]. The accuracy of those methods is discussed by Cokelet [36].

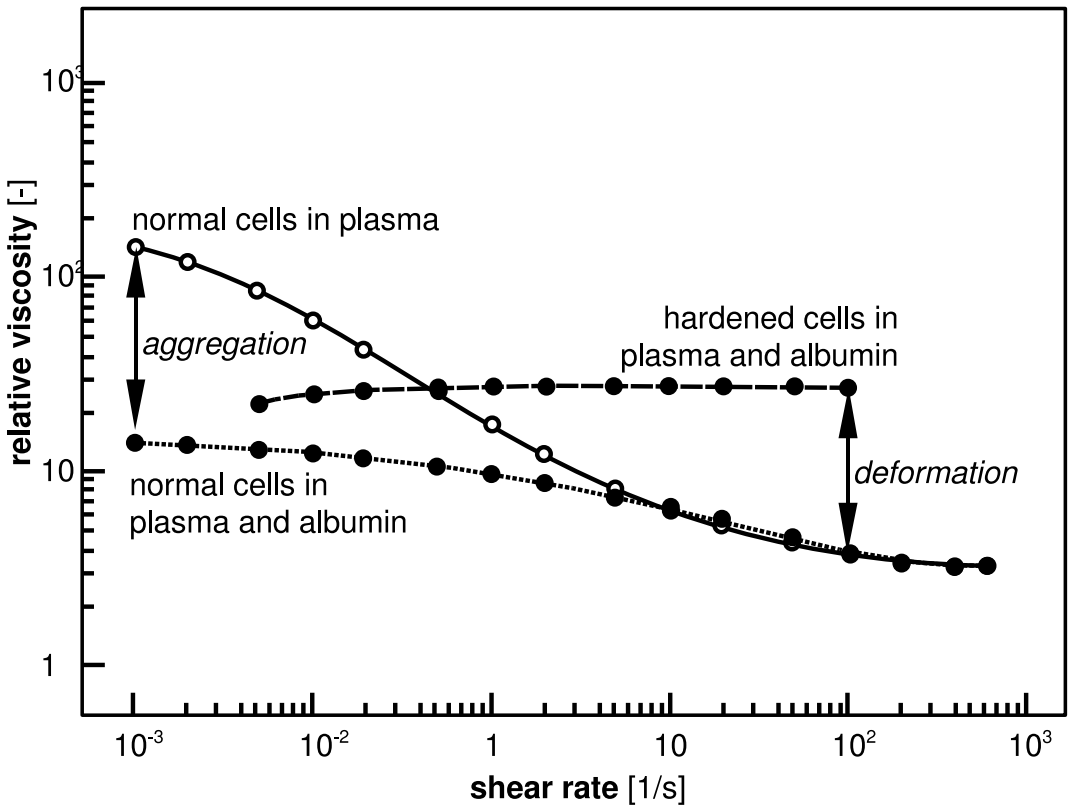

Figure 2.3: Relation between viscosity and shear rate for human blood (data from [33]).

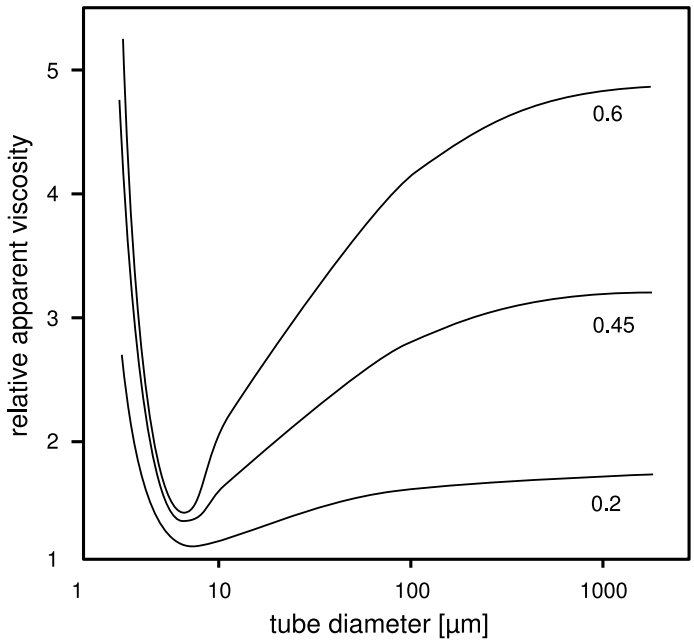

Figure 2.4: Apparent viscosity, relative to plasma viscosity, as a function of tube diameter at shear rates above 50 s^{-1} for hematocrit values of 0.2, 0.45, and 0.6 (data from [136]).

2.4 Hemodynamics

Reviews about hemodynamics appear regularly [24, 37, 96, 97, 102, 133, 180].

Pulsatile blood flow is primarily characterized by two dimensionless numbers: the Reynolds number, *Re*, and the Womersley number, α, defined as:

$$Re = \frac{d\bar{V}\rho}{\eta} \qquad \text{and} \qquad \alpha = d\sqrt{\frac{2\pi f\rho}{\eta}}, \tag{2.1}$$

where d is a characteristic length (equal to the diameter for circular ducts), $\bar{V}$ is the bulk velocity, ρ the density, η the dynamic viscosity, and f the characteristic frequency. Both, *Re* and α relate inertial forces to viscous forces, while in *Re* inertial forces scale with the velocity, and in α they scale with the frequency. In general the Reynolds number is below 2000 (table 2.1) in the human circulatory system. This implies that the flow in most blood vessels is laminar [140]. For low Womersley numbers the pulsating flow is dominated by viscous effects rather than momentum effects. The Reynolds number and Womersley number can be defined for the flow in blood vessels which have an approximately constant geometry over time. For the rapidly fluctuating geometry and flow patterns in the heart, the meaning of the Reynolds number and especially the Womersley number is restricted.

Table 2.1: Reference values for mean velocity $\bar{V}$, diameter d [31], shear rate $\dot{\gamma}$, Reynolds number Re, and Womersley number α in the human vascular network.

vessel		$\bar{V}$ [m/s]	d [mm]	$\dot{\gamma}$ [s^{-1}]	Re [-]	α [-]
	aorta	0.4	25	130	2500	260
	arteries	0.45	4	900	450	40
"micro-vessels"	arterioles	0.05	0.05	8000	0.5	0.5
	capillaries	0.001	0.008	1000	0.002	0.1
	venules	0.002	0.02	800	0.01	0.2
	veins	0.1	5	160	125	50
	vena cava	0.38	30	100	2800	310

The treatment of blood as a continuous or two-phase fluid and the consideration of non-Newtonian properties depend on the studied problem and the scale. At macro scale, when the ratio of blood cell size and characteristic length of the flow domain is small, one might treat blood as a liquid of continuous phase. Low shear rates in the center region of large vessels, however, lead to a radial viscosity gradient. This results in a flattened velocity profile, when compared to a Hagen-Poiseuille profile.

Flow through intermediate blood vessels can be further simplified. Arterioles and venules are still much larger than blood cells. Typical shear rates range between 800 and 8000 $s^{-}1$ and belong to the highest shear rates in the human vasculature (table 2.1). The low shear region in the center of the blood vessel is narrow, when compared to the typical size of erythrocyte aggregates. The radial viscosity gradient becomes less pronounced, and the blood viscosity might even assumed to be constant. Bishop et al. [12] measured parabolic blood velocity profiles in venules of 45 - 75 μm diameter when the mean shear rate is higher than 40 s^{-1}. Without erythrocyte aggregation, they always find the velocity profiles to be parabolic. Charm and Kurland [29, 31], and Charm et al. [32] suggest to treat blood as a Newtonian fluid when the dimensionless group $C/\left(\bar{V}^2\rho\right)$ is smaller than $5 \cdot 10^{-4}$, and the vessel diameter d is between 155 and 2000 μm. The yield stress of blood, C, is the critical stress that must be applied for the blood to start flowing. The yield stress is of order $20 \cdot 10^{-3}$ Pa, values for different temperatures are published by Charm and Kurland [30]. Further, $\bar{V}$ is the mean velocity and ρ the density. In accordance with this criterion, Singh and Prakash find flattened velocity profiles in 180 μm vessels at a mean velocity of $4.4 \cdot 10^{-3}$ m/s [154][1]. Baker and Wayland measure parabolic velocity profiles in vessels between 40 and 200 μm in diameter as long as the mean shear rate is above 6 s^{-1} [6]. Between

[1] $C/\left(\bar{V}^2\rho\right) \approx 1$ with $C \approx 0.02$ Pa from literature [30], $\bar{V} = 4.4 \cdot 10^{-3}$ m/s, $\phi = 35$ %, $d = 180 \cdot 10^{-6}$ m, and $\rho \approx 1000$ kg/m^3

6 s^{-1} and 2 s^{-1} they find slight flattening of the velocity profiles. Below 2 s^{-1} the effect becomes evident. They find the hematocrit value to be relevant only at shear rates below 6 s^{-1}.

At small scales, when blood cells and flow domain diameter are of the same magnitude, blood flow should be treated as a two-phase flow. For the smallest capillaries the flow becomes irregular and is determined by the transport of individual blood cells. Lubrication theory for the movement of single erythrocytes through capillaries that are smaller in diameter than the cells has been developed by Feng and Weinbaum [54].

At even smaller scale (e.g. the erythrocyte depleted layer near the vessel wall) we might treat blood cells and blood plasma domain separately. A cell free layer might not be observed in vivo, when the vessel length is small. According to Bishop [13], the vessels diameter to length ratio d/l should at least be 8 to 15 to observe a cell free layer.

Chapter 3

Measurement Techniques

This chapter contains a review of different diagnostics for the measurement of blood flow with emphasis on optical methods. Current technical possibilities as well as constraints are explored. At the end of this chapter the suitability of these approaches for measuring wall shear stress is discussed and particle image velocimetry is put into the context of the current state of the art.

The methods mainly treated in this review are the optical techniques laser Doppler velocimetry (section 3.1), various laser speckle techniques (section 3.2), and particle image velocimetry (section 3.3). Acoustic methods such as ultrasound Doppler velocimetry or radio wave based methods such as nuclear magnetic resonance imaging are just touched (section 3.4). Due to the utilized wavelengths the non optical methods currently do not qualify for the assessment of wall shear stress in microvessels. According to Reneman et al. [139] blood flow velocities cannot be measured closer to the wall than 250 to 300 μm with ultrasound techniques and with nuclear magnetic resonance imaging the minimal distance is even 1000 to 1200 μm. In contrast, the inner diameter of the embryonic chicken heart is about 200 μm at full dilatation.

Perfusion measurement techniques that merely allow conclusions on mean and time averaged velocities are not treated here. These would be, for example, radionuclide perfusion imaging such as single photon emission computed tomography and positron emission tomography that are reviewed by Lodge et al. [105] and Cuocolo et al. [40]. Positron emission tomography is also part of a review of Zhao et al. [189]. Ultrasonic and electromagnetic point velocity and volume flow rate measurement techniques as well as a microsphere reference sample method are reviewed by Tabrizchi and Pugsley [162].

Pure imaging methods, like orthogonal polarization spectral imaging [28], are not considered as separate measurement techniques in this overview. Nevertheless, such a method can be used as an alternative imaging component for quantitative measurement techniques like particle image velocimetry or particle tracking methods.

3.1 Laser Doppler Velocimetry

Laser Doppler velocimetry, in its original form, is a single point measurement technique with extraordinary temporal resolution. A detailed review of this technique was published by Tropea [168]. Systems that measure up to three velocity components are commercially available. Laser Doppler Velocimetry for spatial measurements is primarily implemented in three ways: scanning (section 3.1.1), simultaneous single point measurements with multiple probes (section 3.1.2), and differentiation of tracer particle position within the measurement volume (section 3.1.3). Full field laser Doppler systems generally provide only one velocity component.

The measurement principle of laser Doppler velocimetry is based on the optical Doppler effect: if a light source (or a light scattering tracer particle) is moved into the direction of a light-detector, the frequency of the reflected light is increased. If the light source moves away, the frequency is decreased. In practice this frequency shift is very small (10-100 kHz) when compared to the high frequencies of light (100 THz) and impractical to measure directly. The frequency shifted light is therefore combined with a non-shifted reference beam. The resulting beat frequency equals the frequency shift and is directly related to the velocity of the light scatterer.

Combining the scattered light and the reference beam takes effort and is sensitive to errors. The different light paths might be affected by changing refractive indexes, for example due to temperature variations. Therefore, most laser Doppler systems are implemented in such a way that both laser beams intersect at an angle. The intersection volume defines the measurement location. A tracer particle passing this volume is illuminated from two different directions. The frequency shift of the reflected light is different for the two laser sources. The resulting beat depends on the angle of the two laser beams and the tracer velocity perpendicular to the axis, z, that bisects the angle, θ, between the beams.

A different way of looking at the concept of the two intersecting beams is to study the interference pattern within the measurement volume. The wave-fronts of the laser beams form interference fringes parallel to the optical axis of the focusing lens system (represented by the Moiré pattern in Figure 3.1). When a tracer particle moves through the dark and bright spaces of the fringe system, it will reflect light at a frequency that depends on the fringe spacing and the particle velocity component, v perpendicular to the fringes. Both perceptions lead to an identical relationship between particle velocity and measured frequency-shift, Δf:

$$v = \frac{\lambda}{2 \cdot sin(\theta/2)} \cdot \Delta f \tag{3.1}$$

Here, λ is the wavelength of the incident light. The penetration depth of light in tissue depends on its wavelength. Near infrared light ($\lambda \approx 1\mu$m) penetrates several mm, red light ($\lambda \approx 650$nm) up to about 2 mm and green light ($\lambda \approx 540$nm) hardly at all [21].

It should be mentioned that real laser beams are slightly diverging when they leave the laser cavity. This is related to the curved (focusing) cavity mirrors at the ends

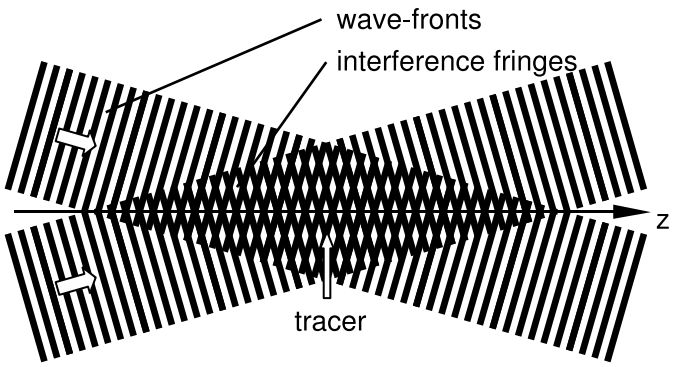

Figure 3.1: Interference pattern of two crossing laser beams.

of the laser rod [71], that in turn is related to the Gaussian wave propagation [50]. Lenses focus the diverging beams in the measurement spot to reduce the size of the measurement volume. The Moiré pattern in Figure 3.4 represents a more realistic fringe system than the one in Figure 3.1. The smallest diameter of the laser beam is called the beam waist. The distance over which the cross section of the beam doubles is referred to as the Rayleigh length [71]. In section 3.1.3 the presence of a short Rayleigh length is exploited for measuring a velocity profile.

3.1.1 Laser Doppler Imaging

Essex and Byrne [52] described a scanning laser Doppler velocimetry system with continuously moving laser beams. The scanned measurement data is usually visualized as an image with color-coded velocity information. The relative motion between laser and tissue, however, can give rise to significant artifacts. Wardell et al. [179] circumvented this problem by using stepping motors for moving the scanning mirror. The scan time was 4 minutes for 4096 image points. Meanwhile, commercial scanning laser Doppler velocimetry systems (laser Doppler imagers/flowmeters) are available that, for example, map skin perfusion over areas of 50×50 cm^2 with 256×256 pixel resolution in about five minutes (Moor Instruments Ltd.). Retina perfusion can be measured with a spatial resolution of up to 10 μm and a temporal resolution of 2 seconds for a scan of 256×64 pixel (Heidelberg Engineering GmbH) [119]. The scanning devices lack a reference beam. Instead, Doppler shifted light from moving blood cells beat with reflected light from stationary tissue. Depending on the spatial resolution, there might be several blood cells in the measurement volume with different velocities. This results in a frequency distribution around a frequency representing the mean velocity rather than a single beat frequency.

Scanning laser Doppler velocimetry has become a standard tool in diagnostics. Figure 3.2 shows a laser Doppler scan. The number of publications on this topic is quite large. Briers [21] identified various fields of applications in his review. One

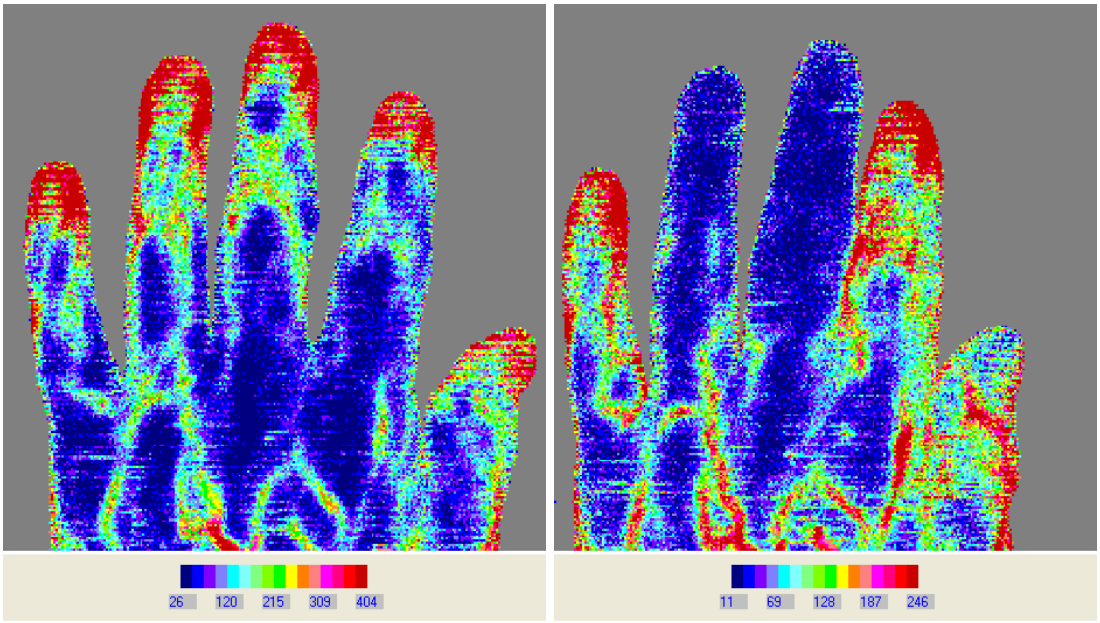

Figure 3.2: Laser Doppler scan of a hand visualizing the Raynaud's disease phenomenon, a perfusion disorder related to temperature changes. The left scan shows the baseline measurement, the right scan shows the hand after cold water immersion (scans are kindly provided by Moor Instruments Ltd.).

of the most important applications might be the diagnosis of burn depth. Pape [127] published an audit of the use of laser Doppler imaging in the assessment of burns of intermediate depth. Superficial burns show an inflammatory response, which is indicated by high perfusion. This diagnosis can be used to distinguish superficial burns from deeper burns that need surgical treatment. Basically similar to scanning laser Doppler velocimetry is the time-varying speckle technique (section 3.2.2).

3.1.2 Multi-Probes Laser Doppler

Serov et al. [147, 148] avoid scanning by replacing the widely used avalanche photo detector by a complementary metal oxide semiconductor (CMOS) image sensor. In contrast to charge coupled device (CCD) sensors, some CMOS sensors allow the continuous conversion of photocurrent into output voltage. The Doppler shift ranges typically between 0 and 20 kHz for the microcirculation. To attain a corresponding sampling rate, the area of interest had to be reduced to 64×8 pixel. A perfusion map of 256×256 pixel could be obtained by sampling 128 sub-windows one after the other. The repetition rate for measuring the full area is 90 s including signal processing (mainly determined by the FFT) and screen display. Typical results are shown in Figure 3.3.

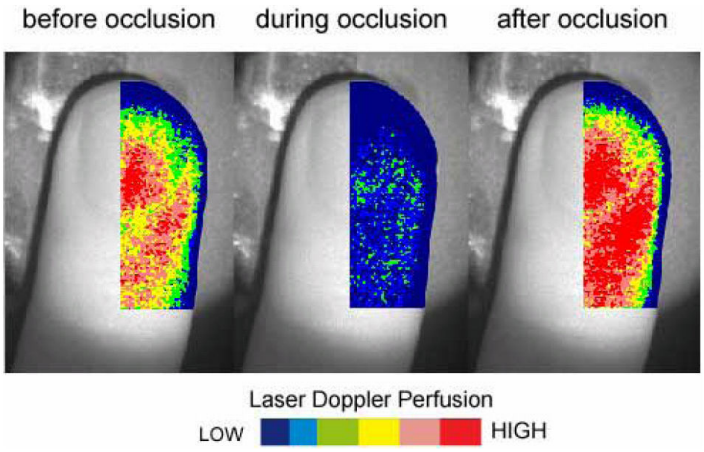

Figure 3.3: Multi-probe Doppler perfusion images of the finger-tip obtained before, during, and after ligation of the upper arm (figure from Serov et al. (2005) [148]).

3.1.3 Profile Laser Doppler

Czarske [41] introduced a system that differentiates the position of the tracer particle within the measurement volume. The set-up measures the velocity profile within the elongated laser Doppler measurement volume, along the optical axis of the focusing lens system. The system exploits the curvature of the Gaussian laser wave fronts (see also section 3.1). Because of this curvature, the distance of the interference fringes varies along the optical axis (figure 3.4). To determine the position of a tracer particle in the measurement volume, a second pair of laser beams with a different frequency (color) is added to the set-up. Due to (intended) chromatic aberration of the focusing lens system, the beam waists of both beam pairs are shifted longitudinally with respect to each other. In this way, one of the fringe systems in the measurement volume is convergent, while the other one is divergent. A particle that passes through the measurement volume will thus reflect two burst signals of different frequency. The quotient of the two monochromatic burst frequencies, f_i, equals the quotient of the different interference fringe distances, d_i, at this position. This quotient is unique for the position along the optical axis. The particle position, z, is then determined by means of a calibration function ϕ:

$$z = \phi\left(\frac{f_1(z)}{f_2(z)}\right) \tag{3.2}$$

Once the position of the particle is determined, one of the monochromatic burst signals is used to determine the velocity. The length of the measurement volume is adjusted to the individual application (5 mm [42], 1.2 mm [41], 0.7 mm [27]). The spatial resolution is reported to reach the sub-micrometer domain [27]. Alternative methods of generating two suitable fringe systems are reported by Büttner and Czarske [25] and

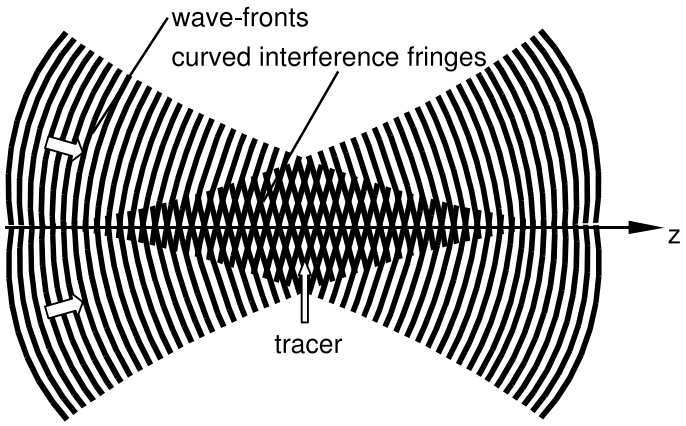

Figure 3.4: Interference pattern of two Gaussian laser beams-waists.

Shirai et al. [149]. The two velocity components perpendicular to the optical axis can be measured by aligning two fringe systems orthogonally to each other. Additionally, the axial velocity component can be determined from the temporal frequency variation of the Doppler burst signal [26]. The technique has not yet been applied to in vivo blood flow.

3.2 Laser Speckle Techniques

Laser speckle is a grainy, stationary interference pattern [118]. It is produced when coherent light is scattered at a diffuse surface or a number of individual scatterers (like particles in a fluid). Interfering wavelets of different optical path lengths fill the surrounding space with a random pattern [63]. Individual speckles are very small close to the diffuse surface and grow in size at larger distance. When scatterers move in a uniform manner, the speckle pattern moves at the same rate. Small displacements of scattering particles slightly change the speckle pattern. Large displacements alter the pattern entirely, so that it becomes completely uncorrelated.

3.2.1 Laser Speckle Contrast Imaging

Laser speckle contrast imaging is based on so called image speckle. This occurs when a larger area is illuminated by a laser and projected on an image plane. A time-integrated image of stationary particles, where the dimension of the particles and the distance between them is less than the light wavelength, shows a speckle pattern of high contrast. Moving particles reduce the contrast due to the averaging of the non-stationary speckle pattern over time. An equation can be deduced that links flow velocity to reduction in speckle contrast [55]. Speckle contrast is reduced by particle

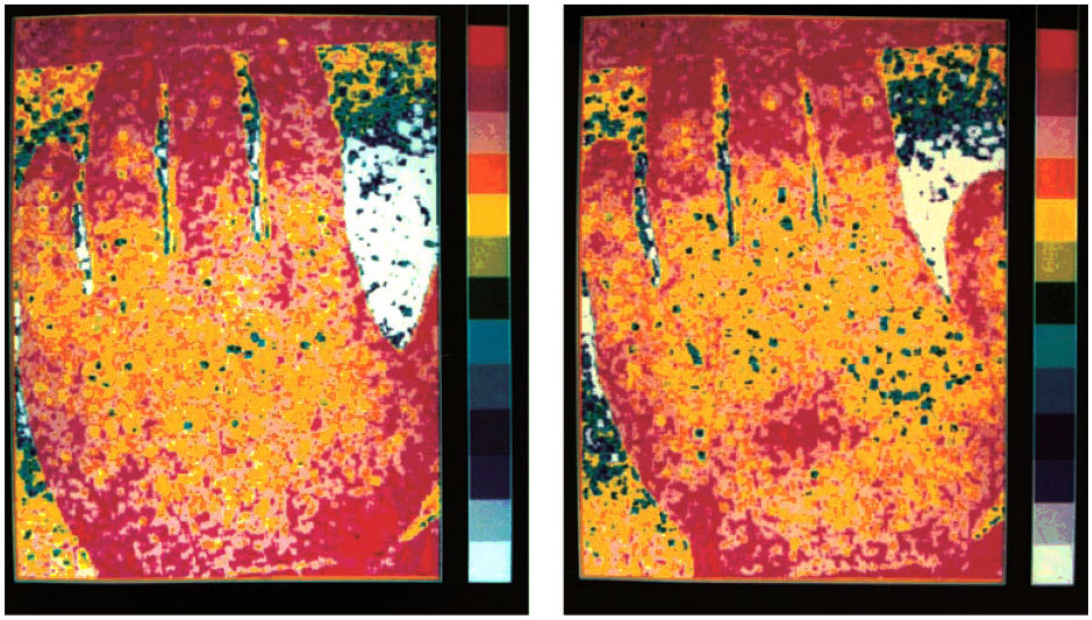

Figure 3.5: Laser speckle contrast image before (left) and after (right) gently scratching the back of a hand (figure from Briers (2001) [21]).

movement in any direction. This makes the technique sensitive for motion parallel as well as perpendicular to the measurement plane. The speckle pattern change due to motion along the line-of-sight is such that a relative movement of half a wavelength causes a full cycle of intensity change. The sensitivity to in-plane motion is significantly weaker, because it is only determined by the size of the speckle pattern [20]. The directional difference in sensitivity is the main reason why the relationship between flow velocity and contrast reduction must be deduced for different types of velocity distributions. Therefore the type of velocity distribution must be known a priori [22].

Briers et al. [22] advanced the development of laser speckle contrast imaging and concisely reviewed the technique. Figure 3.5 shows a laser speckle evaluation. At present, laser speckle contrast imaging has developed into a standard perfusion measurement technique for animal models [187] that can be combined with other techniques to monitor blood flow, hemoglobin concentration and oxygenation simultaneously [49]. Zhao et al. [189] included laser speckle imaging in a review about skin blood flow imaging. The latest effort aims on the reduction of noise [177].

3.2.2 Time-Varying Speckle

Time-varying speckle is based on the evaluation of temporal statistics of speckle fluctuations in a single point. In comparison to laser speckle contrast imaging (section

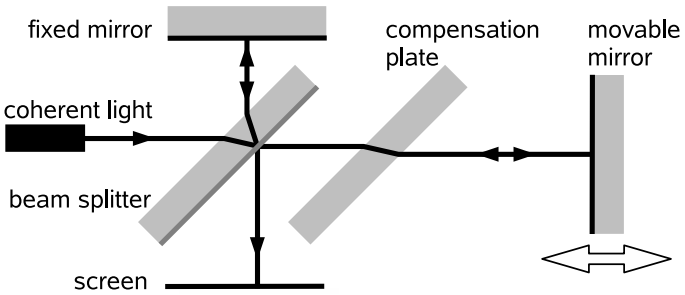

Figure 3.6: Michelson interferometer.

3.2.1) that is based on image speckle, so called far-field speckle is utilized. A collimated laser beam illuminates a small spot in the flow. Light from all points within this area interferes in the image plane and forms the speckle pattern. When the scatterers move, individual speckles at a fixed position fluctuate. The frequency spectrum of these fluctuations can be related to velocity information.

Briers [20] showed that the interference-based perception of far-field speckle can be interpreted in terms of the Doppler effect. To show the equivalence of the Doppler and the interferometric explanation, he considers a Michelson interferometer (figure 3.6). When the mirror in the measurement arm of the interferometer is moved, a small detector in the detection plane recognizes a temporal intensity fluctuation. This fluctuation can be interpreted as the beat of the reference beam and the light that is reflected by the moving mirror. The frequency of the light that comes from the moving mirror is altered due to the Doppler effect. The detected intensity fluctuation can also be explained by the variation of the optical path length, without considering the Doppler effect. The optical path-length of the beam that is reflected by the moving mirror is continuously altered due to motion. Depending on the actual mirror position constructive or destructive interference is recorded at the detector. The relation between intensity fluctuation frequency and mirror velocity can be shown to be identical in both cases.

The main difference between laser Doppler velocimetry and time-varying speckle is the absence of a separate reference beam. A Doppler spectrum is still present when there is interference of scattered light from particles with different velocities (different beat frequencies). This spectrum, however, just provides information about the variation of velocities in the measurement volume rather than the mean velocity. When there are stationary tracers present in the measurement volume, the variation of velocities is a measure for the mean velocity. It now becomes obvious that this technique is basically identical to the laser Doppler imager (section 3.1.1). Aizu and Asakura [2] reviewed different statistical methods to extract the mean blood cell velocity from speckle fluctuations.

3.3 Particle Image Velocimetry

Particle image velocimetry relies on the visualization of flow by means of small tracer particles. In general, the movement of the particles is recorded in two sequential, digital images. The displacement of the particles in the second image, relative to the position of the particles in the first image, divided by the time delay between the exposures, is a measure for the velocity of the fluid. The displacement of the particles is calculated by means of a two-dimensional cross-correlation [85]. Therefore, a small interrogation window of the first image is correlated with different sections of the second image until the maximum correlation magnitude between the image areas is found. This position is the most probable displacement of the particle pattern in the interrogation window [1, 83, 84, 137]. The local velocity is approximated by dividing the displacement of the particle pattern by the given time difference between the two images. In contrast to speckle methods it is not the grade of decorrelation that contains the velocity information. Decorrelation only occurs due to particles leaving the measurement volume or due to shear within the interrogation area [182], but not due to the movement itself [85]. Particle image velocimetry therefore does not rely on the correlation peak height, but rather on the correlation peak position to obtain the velocity magnitude.

For typical macroscale particle image velocimetry applications, a two-dimensional measurement plane is formed by illuminating a thin plane of the flow with a narrow laser light sheet, whereas for microscale applications the strongly limited depth-of-focus of the microscope objective is used to sample a thin plane in which the particles are sharply imaged [15, 16, 115, 116, 125, 143]. More detail about the thickness of this plane is given in section 4.5. Details about how to improve the correlation result (correlation averaging) are given in section 4.4.

Closely related to particle image velocimetry are particle tracking techniques. Here the movement of individual particles is tracked manually or by appropriate computer programs. In contrast to particle image velocimetry, particle tracking velocimetry requires the distance between the tracer particles to be larger than the displacement [181]. Otherwise it is not possible to unambiguously identify matching particle pairs. This restriction limits the resolution of pure particle tracking velocimetry. The combination of particle image velocimetry in a first step and particle tracking within the correlation window in the second step, however, reaches utmost spatial resolution [86]. Ji and Danuser [82] and Danuser [43, 78] use a correlation averaging method - like introduced by Meinhart [117] and explained in section 4.4 - in combination with sub interrogation window particle tracking to measure actin flow in an epithelial cell at a spatial resolution in the order of 100 nm.

Another closely related term is optical flow. In general, optical flow algorithms [75, 107], aim to calculate the shift of intensity gradients between two images for every pixel. The displacement of a single pixel can not be calculated independently of neighboring pixel [75]. This leads to comparable spatial averaging effects as in particle image velocimetry, where blocks of pixel are correlated with each other.

Single camera particle image velocimetry set-ups measure the two velocity com-

ponents parallel to the image plane. Using two cameras in a stereoscopic configuration one can also measure the out-of-plane velocity component [5, 135].

Several research groups used particle image velocimetry or related particle tracking techniques to study blood flow. The probably first quantitative, optical measurement of erythrocyte velocities in vivo dates back to 1918 [9]. Basler used a self-made light conductor for back-illumination of a straight blood vessel in the sartorius muscle of a frog. A microscope was used to project the erythrocyte movement onto a film that was driven perpendicular to the erythrocyte movement (figure 3.7). The erythrocytes produce streaks on the film. The angle of the streaks relative to the film is determined by the speed of the film and by the velocity of the erythrocytes. Developments based on this technique are discussed by Monro [121]. Wayland [180] developed a technique that is based on the passage time of erythrocytes between two lines of photosensitive elements. The signals of two elements are correlated with each other to determine the velocity profile of erythrocytes over the blood vessel diameter [60]. Baker and Wayland [6] later showed, that the heavily flattened velocity profiles, that were found with the double slit technique, are an artifact due to spatial averaging. Schmidschönbein and Zweifach [144] used a high speed film camera to analyze the erythrocyte motion in arterioles, venules, and postcapillaries[1] in the peritoneum of a rabbit. A series of more than 100 instantaneous cell velocity profiles were determined as exemplarily shown in figure 3.8. Tangelder et al. [164] enhanced the spatial resolution of the tracking technique by labeling blood platelets with a fluorescent dye to measure flow velocities in arterioles (17 to 32 μm diameter) of the rabbit peritoneum. Dual flash video images were used to capture the platelet motion. The velocity profiles were assembled by a number of individual measurements at different radial positions of the vessel. The illumination flashes were triggered my means of an electrocardiogram (ECG). Smith et al. [158] and Long et al. [106] adapted this technique by using artificial, fluorescent tracer particles of 470 nm diameter to further enhance the spatial resolution. The velocity gradient in the near wall region of a mouse cremaster muscle venule could be estimated by manually tracking the movement of tracer particles at irregular distances from the flow boundary. A typical particle tracking result is shown in Figure 3.9. Velocity data can be acquired at high spatial resolution by this method. The manual evaluation, however, is highly dependent on the operator and limits the amount of processable data. Sub-pixel accuracy is not achieved.

Singh and Prakash [154] used optical flow algorithms to determine velocity profiles in 180 μm vessels of frogs and mice. Hitt et al. [72] applied a correlation technique to video images of the venous flow in the hamster cremaster muscle. Tsukada et al. [169] and Sugii et al. [160, 161] used particle image velocimetry to measure red blood cell velocity profiles in peritoneum vessels of rats (figure 3.10). Hove et al. [77] and Hove [76] followed the motion of small groups of erythrocytes through the heart of a zebrafish embryo (figure 3.11). Recently Lee et al. [92] investigated the flow through vitelline vessels by means of particle image velocimetry. References men-

[1] Vessels that are located just to the venous side of a capillary.

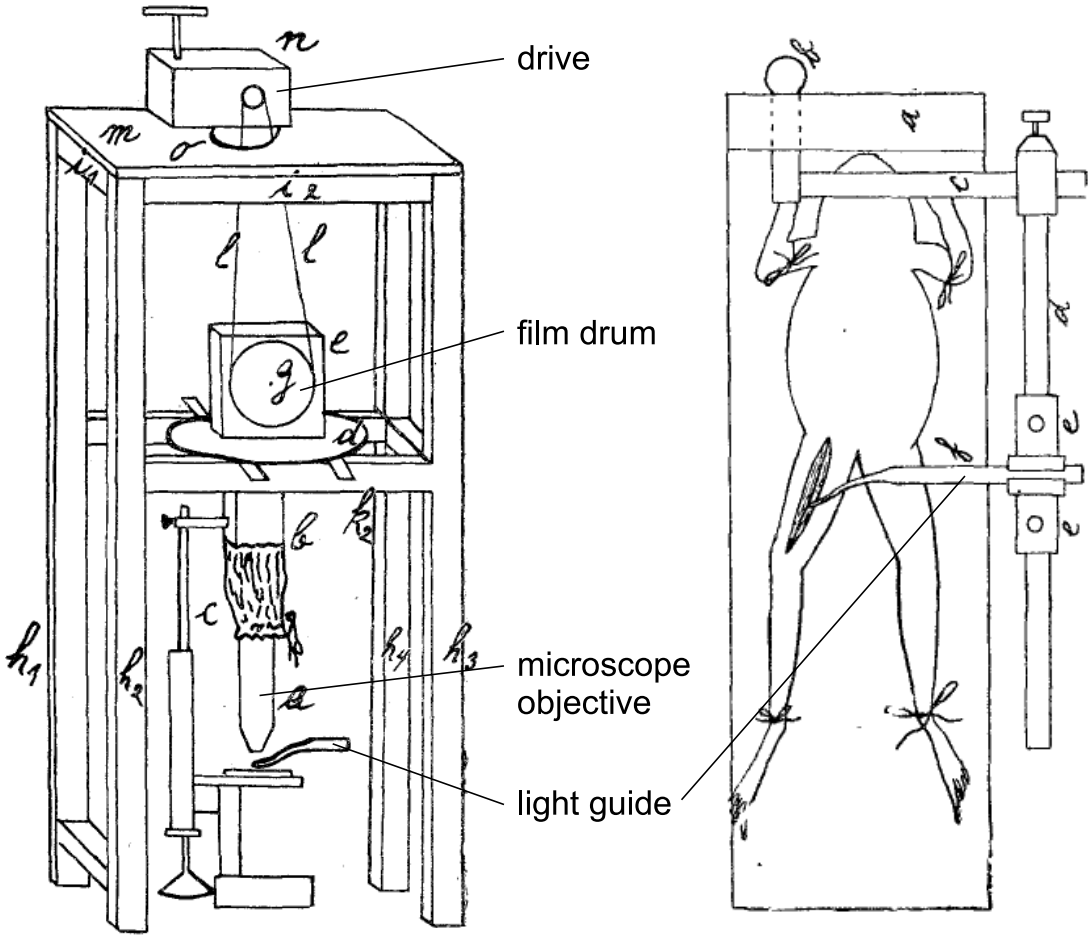

Figure 3.7: The set-up published by Basler in 1918 [9] to measure erythrocyte velocity profiles. The light of an arc lamp is focused into the light guide for back illumination of the blood vessel.

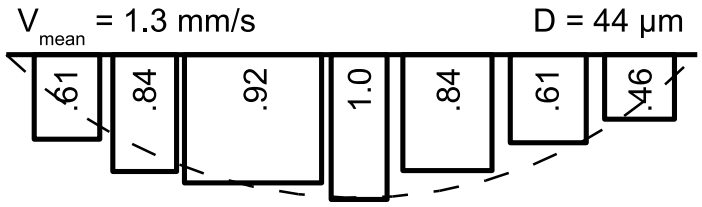

Figure 3.8: Blunted red cell velocity profile in a venule of the rabbit peritoneum. The image is reproduced from Schmidschönbein and Zweifach (1975) [144].

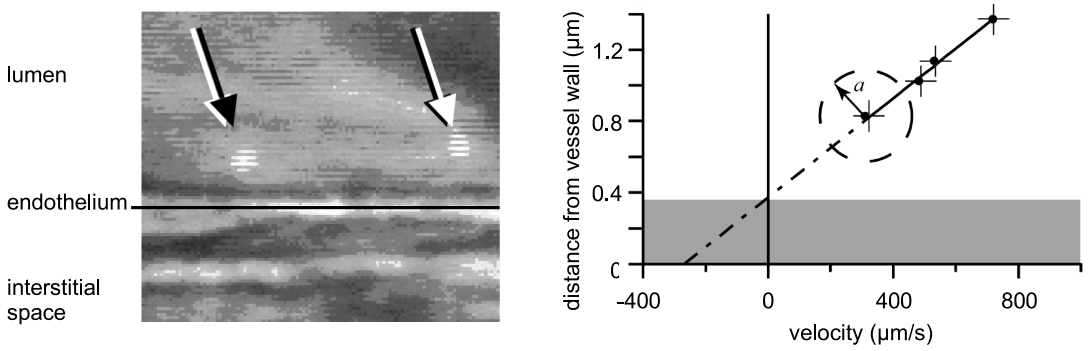

Figure 3.9: Particle tracking in a mouse cremaster muscle venule (figure adapted from Smith et al. [158]). Left: Double stroboscopic image of a single microsphere in a venule of 21 μm diameter. The black arrow points to the first, the white arrow to the second image of the sphere. Right: Cumulative particle tracking data in a vessel of 32.8 μm diameter. The velocity becomes zero at a finite distance above the vessel wall, indicating the presence of a glycocalyx layer. The non-parallel movement of the tracer particle in the example image is not addressed in the original article.

tioned in this paragraph have in common that erythrocytes are used as tracer particles, so the physiological disturbance is limited to a minimum. Associated disadvantages of erythrocyte tracer particles are discussed in section 4.1.4. The measured erythrocyte velocity might also deviate from the plasma velocity (section 2.4). Conclusions on the wall shear stress distribution are therefore difficult to deduce.

Debaene et al. [46] showed how to derive wall shear rate fields in artificial vessels from a single particle tracking measurement. They determined the depth position of the tracer particles from their brightness in a hazy fluid.

3.4 Non-Optical Methods

3.4.1 Doppler Ultrasound Velocimetry

Doppler ultrasound techniques utilize the acoustic counterpart of the optical Doppler effect which was already described in section 3.1. For the measurement of blood velocities, basically three variants have been established. Continuous wave Doppler velocimetry, pulsed Doppler velocimetry, and so called color Doppler.

Continuous wave Doppler sensors contain a separate emitter and receiver which are both constantly operated. The Doppler frequency spectrum can be evaluated continuously and provides information about the velocity band along the beam. Spatial information is not provided.

Pulsed Doppler systems additionally give information about the measurement lo-

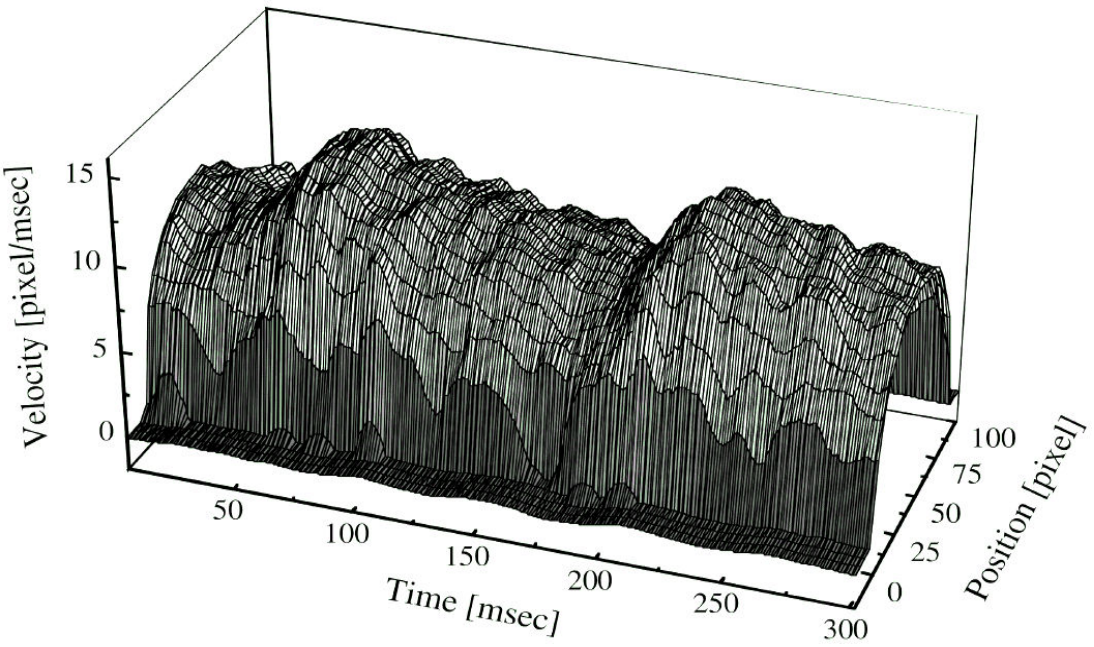

Figure 3.10: Time series of cross sectional blood velocity profiles obtained by particle image velocimetry in an arteriole in the rat peritoneum (figure from Sugii et al. [161]). The vessel is about 25 μm wide. Erythrocytes were used as tracer particles. A high speed camera (512×512 pixel, 1000 frames per second) was used for image acquisition.

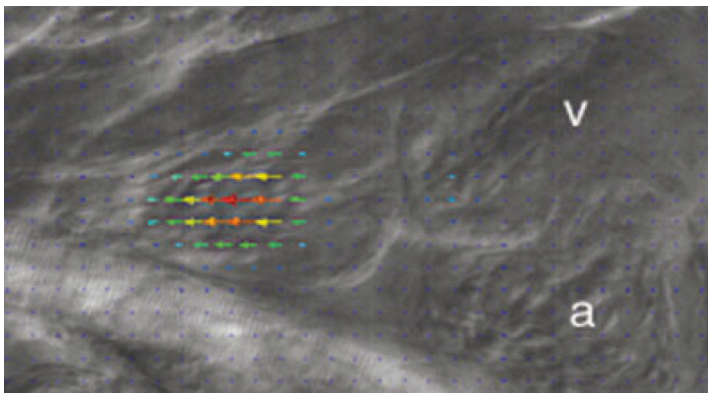

Figure 3.11: Particle image velocimetry field in the bulbus arteriosus of a zebrafish embryo during systole (a, atrium; v, ventricle). The flow domain is about 50 μm wide. The images were acquired at 256×256 pixel in real time. The figure is modified from figure 2d in the paper by Hove et al. [77].

cation by determining the runtime of the reflected wavetrains by defining time gates. Multi-gate techniques can be used to measure velocity profiles along the vessel diameter. Short wavetrains increase the spatial resolution, but hamper the accurate determination of the Doppler shift. A more detailed description is given by Hoeks et al. and Gill [62, 73]. The derivation of shear rates in larger arteries and the integrated detection of vessel walls is given by Brands et al. [18, 19]. Unbiased measurements are only possible in straight vessel sections [90]. Ferrara et al. [56] report measurements in microvessels with diameters above 40 μm in the ciliary body of the rabbit eye. Velocities could be detected from 0.4 mm/s upwards.

A multi-gate, pulsed Doppler system can be equipped with an automatically pivoting sensor. The Doppler shift of every measurement point (determined by depth and scanning angle) is usually plotted as a color coded two dimensional image. Such a system is widely referred to as a color Doppler system.

3.4.2 Ultrasound Particle Image Velocimetry

Particle image velocimetry is not restricted to optically acquired images. Lin et al. [98] used ultrasonic imaging to measure the velocity distribution in the left ventricle of a pig. Kim et al. [87, 88] and Zheng et al. [190, 191] determined flow profiles in artificial models of arteries and in a rotating flow apparatus. In contrast to optical imaging, an ultrasound image is composed by scanning the field of interest. Small gas bubbles act as scattering sites for the acoustic waves. The intensity of the echo depends on the reflective property of the tracers. The time of flight is used to determine the scanning depth. The time difference between two images in optical particle image velocimetry is replaced by the time difference between identical beam positions in two successive echo scans. Due to high seeding densities and small tracer diameters, when compared to the utilized wavelength, ultra sound images resemble a speckle pattern rather than single particle images. The speckle pattern stays fairly stable and moves with the flow [98]. The spatial resolution of ultrasound particle image velocimetry is effectively about three orders of magnitude lower than with optically acquired images (table 3.1). Zheng et al. [191] report a spatial resolution of up to 0.4 mm and a temporal resolution of up to 0.5 ms (2 kHz frame rate).

3.4.3 Nuclear Magnetic Resonance Imaging

Nucleons have an angular momentum which leads to a quantized magnetic momentum or spin. In case of a hydrogen atom the nucleus is composed of a single (unpaired) proton. The magnetic moment is thus not counterbalanced. The potential energy of the magnetic momentum in an homogeneous, external magnetic field depends on the direction of the momentum. The potential energy is minimized when momentum and external field vectors point into the same direction and is maximized when they point into opposite directions. In case of the hydrogen nucleus, quantum mechanics permits just two possible orientations for the magnetic momentum: parallel and anti parallel

with the outer magnetic field. The magnetic momentum of a hydrogen atom of low potential energy (parallel momentum vector and field vector) can be flipped into the high energy state (anti parallel vectors) by absorbing a photon of sufficient energy. Flipping a nuclear spin into this excited state is called nuclear magnetic resonance. The nucleus flips back into its normal state by emitting a photon. The frequency of this photon depends on the energy difference between the normal and the excited state, which is determined by the strength of the outer magnetic field.

Hydrogen atoms are usually bound into molecules. The atoms in the immediate vicinity of a hydrogen atom interfere with the outer magnetic field and in this way change the energy difference between normal and excited state. The frequency of a resonance photon can therefore identify different chemical environments.

In nuclear magnetic resonance tomography, a second, inhomogeneous magnetic field is superimposed on the homogeneous magnetic field. The inhomogeneous field is shaped in a way that small resonance frequency bands can be assigned to a specific volume element of the measured object.

First investigations to exploit the nuclear magnetic resonance technique for measuring blood velocities date back to Singer [151]. Blood flow influences the nuclear magnetic resonance signal in several ways. The signal from fast flowing blood, for example, vanishes. This is explained by the displacement of the protons between excitation and detection and is referred to as spin wash-out. This effect can be exploited for velocity measurements by measuring the signal amplitude at varying time periods between excitation and detection [152]. A wash-out curve is produced that can be related to the flow velocity.

Phase velocity cine magnetic resonance imaging exploits the phase shift of radio waves emitted by hydrogen in flowing blood [134]. Photons emitted by stationary tissue, in contrast, show no phase shift. The magnitude of the phase shift can be related to the flow velocity. The velocity component perpendicular to the measurement plane and the direction of the flow is determined. Measurements in orthogonal planes allow for the determination of all three velocity components [113]. Frydrychowicz et al. [57, 58] quantify the three dimensional flow in a Dacron graft repair and show the hydrodynamic influence of pathological geometric alterations of the thoracic aorta [59].

Numerous other techniques for extracting flow velocity information from nuclear magnetic resonance imaging are reviewed by Smith [157]. Bradley and Waluch [17] describe the effect of different flow phenomena on standard magnetic resonance images. Bauer et al. [10] demonstrated myocardial perfusion measurements in isolated rat hearts at a spatial resolution of $140\times140\times1500\ \mu\text{m}^3$ and a temporal resolution of 40 seconds. Cuocolo et al. [40] review the application of magnetic resonance imaging on the visualization of myocardial perfusion. Magnetic resonance imaging can also be used for the visualization of skin blood flow [189].

3.5 Conclusions

Table 3.1 concisely summarizes the reviewed methods in terms of spatial and temporal resolution. The table serves as an overview rather than a comparison, because most of the discussed measurement methods are complementary. The methods listed in this table cover three distinct application ranges with almost no overlap.

- Laser Doppler imaging and speckle methods compete in the field of skin and retina perfusion imaging.
- Particle image velocimetry and particle tracking techniques cover research in blood flow at small scales and high spatial resolution.
- Ultrasound particle image velocimetry, ultrasound Doppler, and magnetic resonance imaging compete in the field of flow measurements in the heart and in larger and intermediate blood vessels.

These three application ranges define different technical boundary conditions. Particle image velocimetry and particle tracking techniques are designed to satisfy the demands of biomedical researchers. Characteristic parameters are basically spatial and temporal resolution. Perfusion imaging systems based on laser Doppler and speckle techniques are primarily designed as diagnostics tools and are less suitable for quantitative measurements. Safety and ease of use are the most important parameters. Alone the profile approach (section 3.1.3) might provide higher spatial resolution, but up to now this technique was not used for blood flow measurements. Nuclear magnetic resonance and ultrasound systems are readily available in most hospitals and are already approved for human use. Velocity measurement capabilities are implemented as an additional feature.

The reviewed measurement techniques leave a gap in the application range. Large scale internal flows can be quantified as well as superficial microscale flows. The flow through the small blood vessels of the muscles, the inner organs, and the connecting tissue, however, remains immeasurable[2]. Another gap of about six orders of magnitude can be observed between the wavelengths of the electromagnetic spectra that are utilized by the discussed measurement techniques. This gap is bounded by the radio waves on the one side and the visible spectrum on the other side. The unused microwave and infra-red spectra might provide a good trade-off between resolution and penetration depth in future technologies (e.g. terahertz imaging).

From this review of measurement methods it is also noticeable that the capabilities of particle image velocimetry are not fully exploited, yet. Correlation based measurements have been done using erythrocytes as tracer particles. Compared to much smaller, fluorescent tracer particles, a lower signal to noise ratio and limitations in spatial resolution have to be accepted (section 4.1.4). Small, fluorescent tracer particles

[2] If we do not consider indirect measurement methods like radionuclide perfusion imaging.

Table 3.1: Spatial and temporal resolution of in vivo full field blood velocity measurement techniques.

method	velocity components	spatial resol. [μm]	measurem. duration [seconds]	remarks
scanning laser Doppler	1	10^1 [a]	10^0 [b]	diagnostics [c]
multi-probe laser Doppler	1	10^2 [d]	10^2 [e]	development
profile laser Doppler	1 [f] to 3 [g]	10^{-1} [h]	10^{-3}	development
laser speckle contrast imaging	1	10^2 [i]	10^{-3}	animal research [j]
particle image velocimetry	2 to 3 [k]	10^{-1} [l]	10^{-3}	animal research
Doppler ultrasound	1	10^1 [m]	10^{-3}	human research
ultrasound particle image velocim.	2	10^2 [n]	10^{-2} [o]	animal research
nuclear magn. resonance imaging	1 to 3 [p]	10^2 [q]	10^{-2} [r]	human research

[a] Retina perfusion measurements [119].
[b] For a 256×64 pixel area [119].
[c] [21, 127]
[d] Typical value for skin perfusion measurements. Systems are optimized for large imaging areas.
[e] For a 256×256 pixel area inclusive data processing [148].
[f] [42]
[g] Two components [26]. Three components presented at GALA Fachtagung 2006, Göttingen.
[h] [27]
[i] Typical value for skin perfusion measurements.
[j] [187]
[k] Three components can be measured with a two camera set-up [5].
[l] [158]
[m] [56]. Limited by the wavelength of ultrasound.
[n] [191]. Limited by the wavelength of ultrasound.
[o] [191]
[p] [113]
[q] [10]
[r] Per slice [113, 124].

on the other hand, have been used to increase the signal to noise ratio and the spatial resolution, but only in particle tracking experiments that were manually evaluated. Manual evaluation implies high dependency on the perception of a human operator, as well as strong limitations in the amount of processable data. Sub-pixel accuracy is not achieved. The key for exploiting all the capabilities of particle image velocimetry is to combine the advantages of correlation based image evaluation and various fluorescent tracer particles that are chosen to adapt to the individual demands of different applications.

Chapter 4

Particle Image Velocimetry for Blood Flow

The basic idea of cross correlation based particle image velocimetry has been introduced at the beginning of chapter 3.3. There are basically three associated technical domains that need to be adjusted to the present measurement task. These are the set-up that accommodates the biological system and is used to acquire the digital images (section 4.1), the seeding (section 4.1.4), and the image evaluation method (section 4.4).

4.1 Experimental Set-Up

To adjust the experimental set-up to the biomedical flow conditions, various aspects need to be addressed. At first, the living organism has to be accommodated in a way that the influence of the set-up on the organism is reduced to a minimum and natural behavior is guaranteed (section 4.1.1). Secondly, the optical parameters of the image acquisition system need to be adjusted to the flow domain and the resolution demands of the biomedical question (section 4.1.2). Further, the particularities of pulsating or non-stationary flow have to be considered (sections 4.2 and 4.3).

4.1.1 Accommodation of the Model Organism

With regard to the application of the measurement technique on actual biological questions, as explained in the introduction of this thesis, the chicken embryo was chosen as a model organism. The development stage of the chicken embryo is characterized by the staging criteria of Hamburger and Hamilton (HH-stages) [68]. The applied measurements (chapter 5) demand embryos between HH-stage 15 and 22. This corresponds to an incubation time of about $2\frac{1}{2}$ and $3\frac{1}{2}$ days, respectively. Figure 4.1 shows a chicken embryo at HH-stage 15. The embryo is surrounded by vitelline vessels that

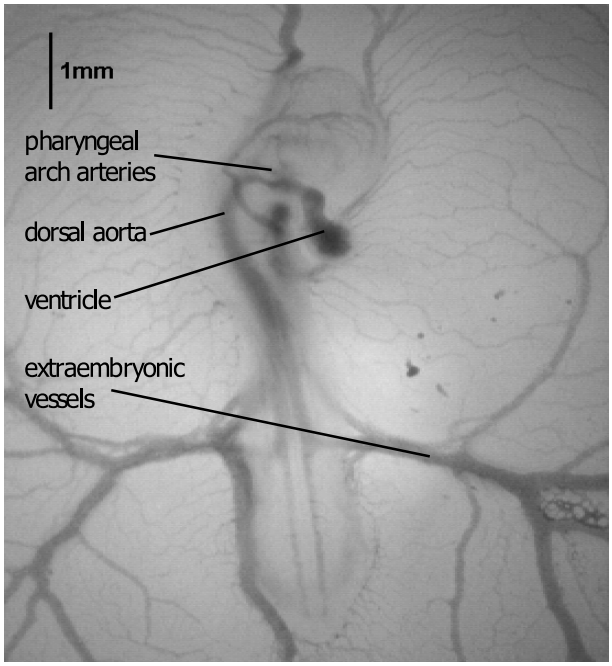

Figure 4.1: HH-stage 15 embryo.

are used to nourish the developing animal. Optical access is established by cutting a window into the egg shell (figure 4.2).

The heart rate of the embryo is sensitive to changes in temperature. To maintain a constant temperature of 37 degrees Celsius the egg is partially immersed in a constant temperature water bath. To prevent desiccation by evaporation, the complete window is filled with phosphate buffered saline (PBS). A cover glass prevents cooling by evaporation of the PBS and assures a distortion free, optical surface (figure 4.2). Alternatively, one may use inert purified mineral oil (paraffinum subliquidum) to prevent desiccation. Glass offers higher optical quality, although mineral oil has the advantage that the embryo is still accessible with tweezers or micro-pipettes.

4.1.2 Optical components

Microscope

The biomedical researcher must be impaired as least as possible by the particle image velocimetry system. It must be possible to manipulate the embryo by micro-surgical interventions and injections. For the placement of tweezers and micro-pipettes, a stereoscopic view is indispensable. Therefore a stereo-microscope is used for the preparation and manipulation of the embryo. Unfortunately, the stereoscopic optics are not sufficient for particle image velocimetry measurements in terms of resolution, light sensitivity and depth of focus. To circumvent transporting the embryo between a

Figure 4.2: Preparation of a fertilized and incubated white leghorn egg for measurements. From left to right: Cutting the shell, removing the window, removing membranes, and protecting the embryo with a layer of phosphate buffered saline and a cover glass.

stereo microscope and a microscope that is optimized for particle image velocimetry, a combined microscope was acquired (Leica MZ 16FA with FluoCombi III).

The standard stereo objective of this microscope offers a working distance of 55 mm which provides ample room for the application of tweezers or micropipettes. Its nominal resolution is 423 line pairs per mm, and the specified numerical aperture is 0.14. For the particle image velocimetry measurement, the holder of the objective can be turned. In this way, the stereo objective is swapped with an objective of higher magnification and resolution. At the same time, the body of the microscope is shifted a little, to center the zoom section of the microscope on the optical axis of the higher resolution objective. The working distance of the higher resolution objective is 19 mm, the resolution is 1500 line pairs per mm, and the numerical aperture is 0.5. Originally, the light captured by this objective was split on both eyepieces by a beam splitter. Unfortunately, the camera mount is located behind this beam splitter, so that only fifty percent of the light reached the camera. To improve the light effectiveness of the set-up, the beam splitter was removed. In turn, only one working eyepiece had to be accepted. The stereo mode is not affected by this alteration.

The magnification of the higher resolution, planapochromat[1] is $5\times$. To adjust the field of view to the diameter of the microscope body, the optical path contains another lens with a magnification factor of 0.8. A zoom section in the microscope body allows one to chose an additional magnification factor between $0.7\times$ and $11.5\times$. Thus, the final magnification range on the CCD chip of a mounted camera varies from $2.8\times$ to $46\times$. The eyepieces add another magnification factor of 10. The standard stereo objective has a magnification of $1\times$, resulting in magnification ranges of $0.7\times$ to $11.5\times$ on the CCD chip and $7\times$ to $115\times$ on the eyepieces.

The microscope is equipped with the necessary filters to utilize fluorescence (see also section 4.1.4). In stereo mode, a separate light path is used for illumination,

[1] A planapochromat objective is corrected for chromatic aberrations at three light wavelengths, typically red, green, and blue, and that additionally has a planar image field.

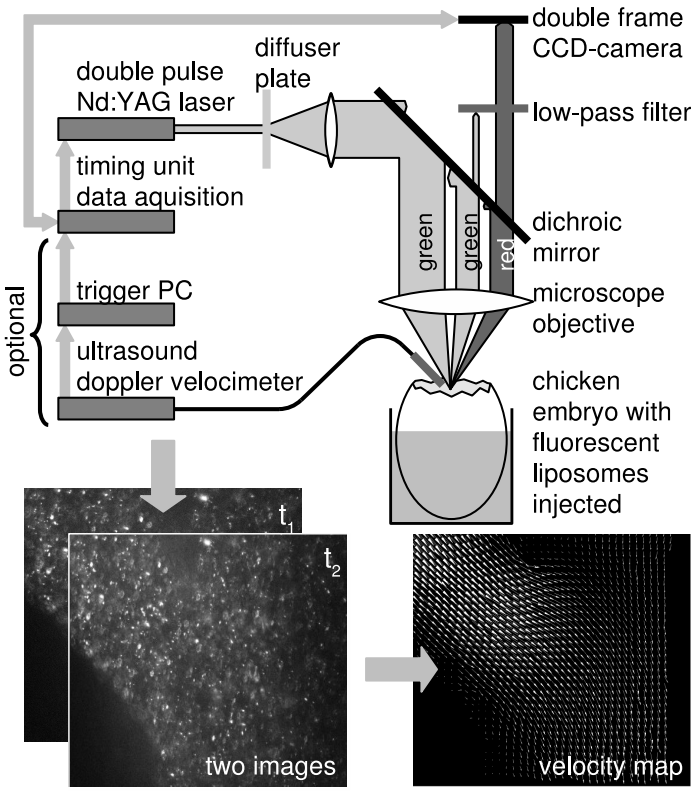

Figure 4.3: Micro particle image velocimetry set-up, using a fluorescence microscope. A dichroic mirror and a low-pass filter allow only the light emitted by the fluorescent tracer particles to reach the camera. The optional components are used in section 4.2, the set-up without the optional components is used in section 4.3.

in addition to the two viewing paths. Appropriate filter combinations (one filter for excitation and two for emission) can be shifted into the light paths. When the higher resolution objective is used, all optical components are aligned along a single, optical axis. Observation and illumination is done via the same optical path. In this mode, the illuminating light is coupled into the light path by means of a dichroic mirror. The emitted light (of longer wavelength) passes the dichroic mirror straight through. Figure 4.3 illustrates the illumination and the separation of reflected and emitted light in the measurement mode.

Camera

There are three main arguments to choose a camera with the highest light sensitivity currently available[2]: 1. The higher the light sensitivity of the camera, the smaller

[2]Products that provide enhanced sensitivity at the cost of resolution (large pixel) are not considered. Cameras that are combined with a phosphorescent image intensifier are also not favored. The quality of

may be the tracer particles (see section 4.1.4). 2. The higher the light sensitivity, the shorter might be the exposure time. Short exposure times are necessary to avoid motion blur when the displacement of the particles relative to the CCD-chip is high[3]. 3. The brightness of fluorescent particles is limited by the excitation-saturation of the fluorescent substance. Further increase of the illumination intensity does not increase the particle image brightness[4], but higher light efficiency of the optical system does.

To take advantage of a cross-correlation based particle image velocimetry evaluation, a double frame camera is required. This demand strongly restricts the number of suitable alternatives. A CCD camera by PCO (sensicam qe double shutter) turned out to be appropriate. The quantum efficiency is specified to be 62 % at a wavelength of 500 nm. The root mean square (rms) noise level is reported to be 4 elementary charges (e^-). The CCD-chip size is 1376×1040 pixel, and the pixel size is $6.45\times 6.45\mu m^2$. In double frame mode the repetition rate is 4.95 Hz at full resolution and 9.9 Hz at 2×2 hardware pixel binning. The minimum interframing time[5] is 500 ns.

Compared to the typical HH-stage 15 chicken embryo heart rate of 2.3 Hz, the cameras repetition rate is relatively low. Faster cameras were tested (MegaPlus ES2020 by Redlake, pco.1200 by PCO), but unfortunately showed insufficient light sensitivity. The tracer particles could not be distinguished from noise. Two approaches have been implemented to tackle the problem or low camera frequency. The first one is to trigger the particle image velocimetry system on the heart rate of the chicken embryo (section 4.2). Triggering allows taking measurements at predefined moments of the heart cycle, i.e. phase-averaged measurements. A full pulse can be reconstructed from a series of slightly shifted measurements at successive heart beats. In the second approach, a non-triggered series of measurements is taken with the highest possible repetition rate. Every measurement is assigned to a specific cardiac phase angle solely based on the heart rate information of the measurement series (section 4.3).

4.1.3 Illumination

In the previous section, the necessity of short exposure times was discussed. For the current application, an exposure time below three microseconds keeps motion blur below one pixel (in case of the highest possible magnification and the highest expected velocity; also see footnote 3 on page 39). To implement high luminance at the same time, a pulsed laser is chosen as a light source. Another advantage of laser light is that it can be easily guided and shaped. This is fortunate for coupling the light into the microscopes illumination path.

---

successive images is generally affected by the relative long decay time of the phosphorescence, which is typically of order one millisecond for a decay down to 10 percent of the initial luminosity.

[3]Example: At a pixel size of 6.45 μm, a magnification of 46$\times$, and a velocity of 50 mm/s (see table 2.1), an exposure time of 3 μs already leads to motion blur of more than one pixel.

[4]During experiments at moderate magnifications using a Nd:YAG laser, the fluorescence image intensity was observed to stagnate above a pulse energy of approximately 4 mJ.

[5]Time between the two exposures for cross correlation.

An important condition for choosing the proper wavelength combination for illumination and fluorescent emission is the penetration depth of light in tissue. Light with a short wavelength, like blue light, does not appreciably penetrate into tissue. Light with a longer wavelength can penetrate up to several millimeters[6]. In terms of penetration depth, a fortunate combination of excitation and emission wavelengths would be red light and near infra red light below 1000 nm wavelength[7]. Another, practical criterion for the selection of the illumination is compatibility with other particle image velocimetry applications in the laboratory and the availability of double pulsed systems for cross correlation. Therefore, somewhat shorter wavelengths were used, namely 527 nm (New Wave Pegasus, Nd:YLF[8]) and 532 nm (New Wave Solo PIV, Nd:YAG[9]) for excitation and 565 nm for peak emission. Both lasers are frequency doubled solid state lasers. The Nd:YAG laser is flash-lamp pumped and the Nd:YLF laser is diode pumped. From the applications point of view, the main difference is the laser pulse length. The nominal pulse duration of the Nd:YAG laser is about 6 to 10 ns, for the Nd:YLF laser it is between 100 and 180 ns. Both pulses are short enough to avoid significant motion blur. The Nd:YLF laser is preferably used, because the typical fluorescence lifetime[10] of the utilized fluorophore rhodamine B is 1.7 ns [109]. Using the Nd:YLF laser, a single fluorophore-molecule can be excited more often and can therefore be induced to emit a multiple amount of light.

Another property of laser-light is that the emitted light is coherent. Coherent light can cause a so called speckle pattern (see section 3.2), which can be very disturbing when uniform illumination is desired. To reduce the coherence length of the laser light[11], a diffuser plate is inserted into the illumination path of the microscope. The plate is placed in the holder for the excitation light filter. The holder is unused, because an excitation light filter is not necessary in case of monochromatic laser illumination (figure 4.3). The tissue itself also reduces the coherence length by multiple light scattering.

Illumination may have some side effects on a biological system. The signaling of the retina or the pigmentation of our skin are popular examples for reactions of cells to light. A sunburn is an example for the destructive impact of intense light. To estimate whether any side effects can be expected by the utilized laser illumination, we compare its properties to laser applications that intentionally impact a biomedical system. Figure 4.4 maps four different physical processes to the optical variables interaction time and power density [14]. The hatched boxes indicate the operational range of the illu-

[6]The exact penetration depth is also dependent on the pigmentation and the density of the tissue.

[7]Fluorescent dyes are commercially available (for example at Atto-Tech GmbH) for absorption wavelengths covering the whole visible spectrum and near infra-red. The excitation efficiency of quantum-dots rises with decreasing wavelength.

[8]short for neodymium-doped yttrium lithium fluoride

[9]short for neodymium-doped yttrium aluminum garnet

[10]the typical time between excitation and emission

[11]Referring to the manufacturer the coherence length of both, the Nd:YAG laser and the Nd:YLF laser, ranges between 2 and 4 centimeters.

mination lasers used in the present work. The boxes are placed at maximum credible power density, that is based on a third of the nominal laser output energy[12].

For photochemical and thermal effects, the utilized pulse duration is several orders of magnitude to short. For electromechanical effects, the power density is not high enough. In terms of power density and pulse duration, the illumination lasers do match the area of direct photoablative effects. The utilized wavelengths of 527 nm and 532 nm, however, do not match the absorption range of most biomolecules such as collagen. For photoablative surgery, exclusively UV-lasers are used. All four mechanisms can thus be excluded either based on pulse duration, power density, or wavelength.

4.1.4 Seeding

Natural Seeding Particles

Obviously, one can use the erythrocytes as tracers that are anyway present in the flow. See chapter 3.3 for numerous practical examples. Also in the scope of the present work, erythrocytes were used as tracer particles (section 5.2). Using erythrocytes has the advantage of only minimally affecting the biological system. The main disadvantages are low contrast images, fixed particle concentration, nonuniform cell distribution due to the Fåhraeus-Lindquist effect (sections 2.1 and 4.1.4), and a large correlation volume (section 4.5).

Using fluorescently labeled thrombocytes tackles the Fåhraeus-Lindquist effect and partially the problem of low signal to noise ratio. See section 2.1 for references that use thrombocytes to trace the movement of blood flow. Thrombocytes penetrate the whole flow domain because of their small size (section 2.1, [170, 171]). Further, fluorescence enables a clear distinction between blood cells and tissue on the one side and flow tracers on the other side by using appropriate filters. Size and number density of the particles can not be adjusted. The amount of fluorophores that can be attached to the platelets is limited.

Artificial Particles

The possibilities of particle image velocimetry can be exploited best, when small fluorescent particles with predefined properties are injected. Artificial particles can be

[12]Losses of at least two thirds will occur, if one assumes a mean transmissivity or reflectivity, respectively, of each optical component of roughly 90 % and a number of at least eleven optical components in the beam path. These are two YAG mirrors in a periscope that is used for guiding the beam to the illumination port of the microscope, one ordinary metallic mirror in the head of the microscope, a ten degrees diffuser plate, at least two lenses in the zoom section, another mirror and a dichroic beam splitter for coupling the laser light into the optical path of the objective, a $0.8\times$ magnification lens in the objective holder, the $5\times$ magnification objective, and the cover glass. In practice, losses will certainly be higher, because of the lower transmissivity of non-coated lenses and mirrors, the off-axis transition of the illumination beam in the zoom section, a number of unknown lenses and diaphragms in the microscope housing, a non optimized diverging angle of the diffuser plate, and misalignment.

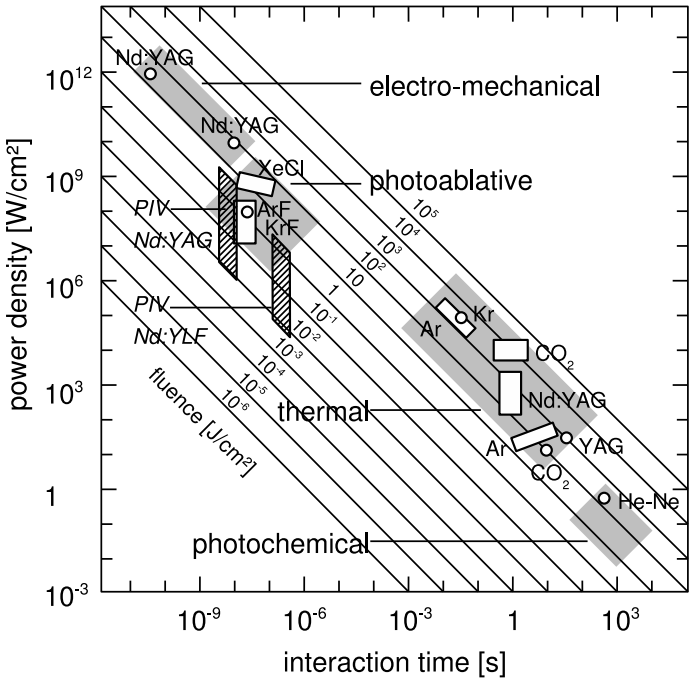

Figure 4.4: Medical interaction map of laser light based on figure 1 in [14]. The operational ranges of the two illumination lasers used in the present work are inserted as hatched boxes. The width of the boxes is determined by the manufacturers specifications for the pulse duration range. The upper threshold of the boxes is given by the minimal illumination spot size at a maximum magnification of 46×, the lower threshold indicates the power density at the lowest possible magnification of 2.8×.

equipped with fluorophores at high density. Using artificial particles, also the particle size and concentration can be adjusted to the well known rules published by Keane and Adrian (1990) [83] to achieve the best possible correlation results.

A simple experiment depicts the wider penetration domain of artificial tracer particles in comparison to erythrocytes (figure 4.5). The top left image shows a single image of blood cells that are moving through the vitelline vasculature of a chicken embryo. Taking the minimum grey value that occurred for each pixel of 200 such images, results in an image as shown at the top right of figure 4.5. Regions that were occupied by a blood cells in at least one of the 200 images appear dark in this image. The experiment was repeated using fluorescence illumination and an optical filter (second row of images). The left image shows 560 nm polyethylene glycol (PEG) coated polystyrene tracer particles in the same part of the vasculature as above. The right picture shows the maximum grey value that occurred for each pixel in a set of 200 images. The areas that were occupied by a fluorescent particle in at least one of the images appear as a bright region. From the minimum and the maximum image, binary masks are generated (figure 4.5, bottom left). The influence of the binarization threshold on the shape of the mask is low, due to the high contrast of the images. This is illustrated by the grey-value profiles next to the averaged images in figure 4.5, top right. The grey-value profiles are taken at an exemplary position as indicated by the vertical white lines in the averaged images. The binarization level is symbolized by a dashed line in the grey-value profile plots. Subtracting one binary mask from the other one highlights the areas that were solely penetrated by tracer particles during the measurement (figure 4.5, bottom right).

In the present thesis fluorescent liposomes [4, 153, 184] of 400 nm diameter, and fluorescent polystyrene particles of 500 nm diameter are used to resolve the velocity distribution in different situations. Figure 4.6 illustrates the principle structure of the fluorescent liposome tracer particles. The liposome membrane consists of phospholipids that form a spherically closed bi-layer to shield their hydrophobic tails against the surrounding aqueous solution. The rhodamine is tagged to the phospholipids. For the synthetic particles, the rhodamine is embedded in the polystyrene-matrix. Both particle types have in common that they are coated with a layer of polyethylene-glycol (PEG). PEG is a chemically inert, non-toxic, biodegradable, and strongly hydrophilic polymer. Coupling PEG molecules to larger molecules or particles is called PEGylation, a standard procedure in chemistry. In flowing blood, PEGylated particles circulate much longer than non-PEGylated particles. Because of their high affinity to water, PEGylated particles stay suspended in watery solutions rather than accumulating at interfaces. When an immune system is present, PEGylated particles are not detected as fast as most other contaminants because of their ability to bind a layer of water[13].

The main advantage of the liposomes over the polystyrene particles is that they are biodegradable. This qualifies the liposomes for non-final animal experiments. Their main disadvantages are that they are less bright than the polystyrene particles and

[13]Because of this property, PEGylated liposomes are widely called “stealth” liposomes [184].

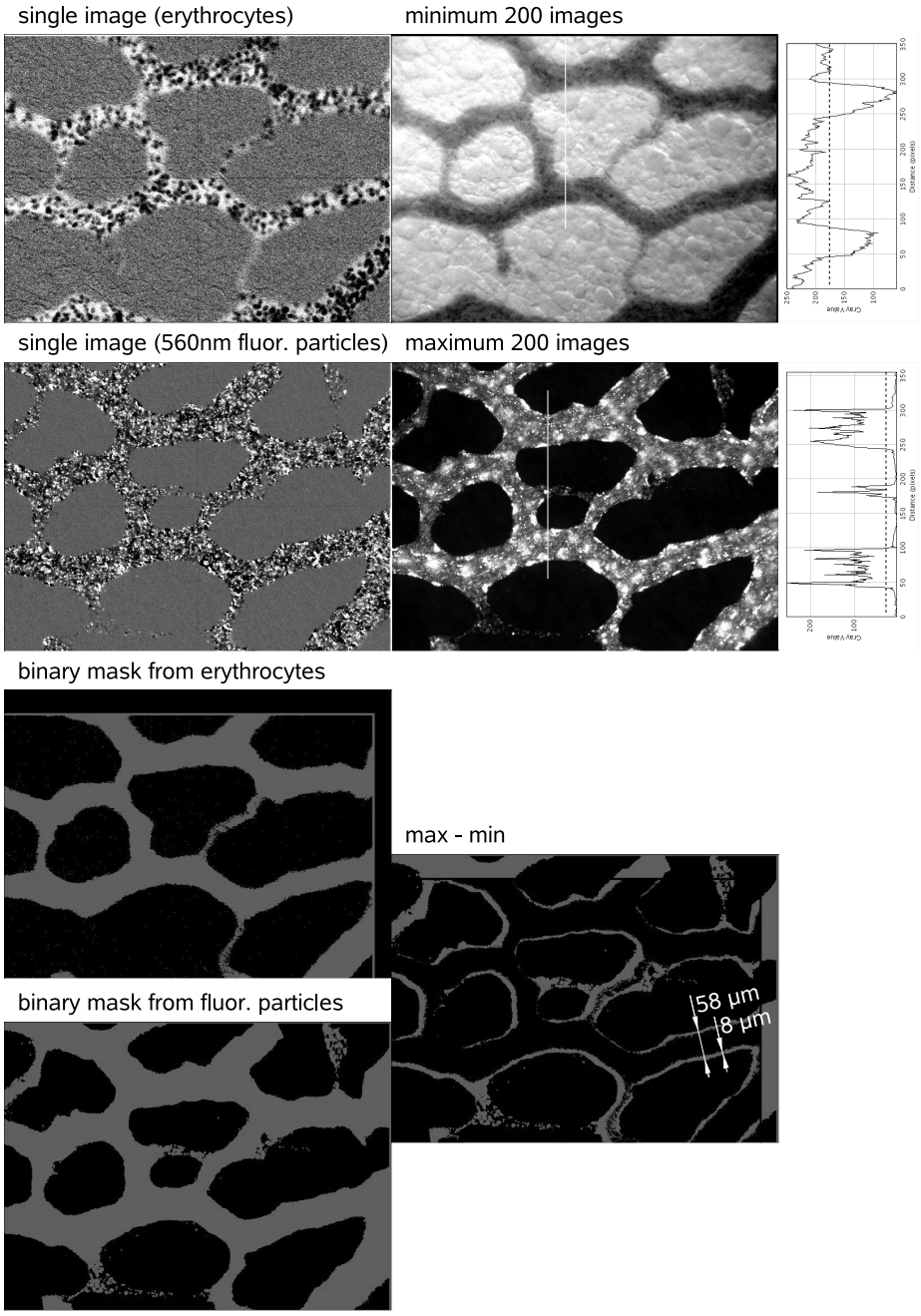

Figure 4.5: Visualization of the plasma rich layer. The magnification is 12×, the pixel size 12.9 μm, the camera frequency 10 Hz. The tracer particles were injected about two hours before the measurement. Please refer to the text on page 43 for a detailed explanation of the different photographs.

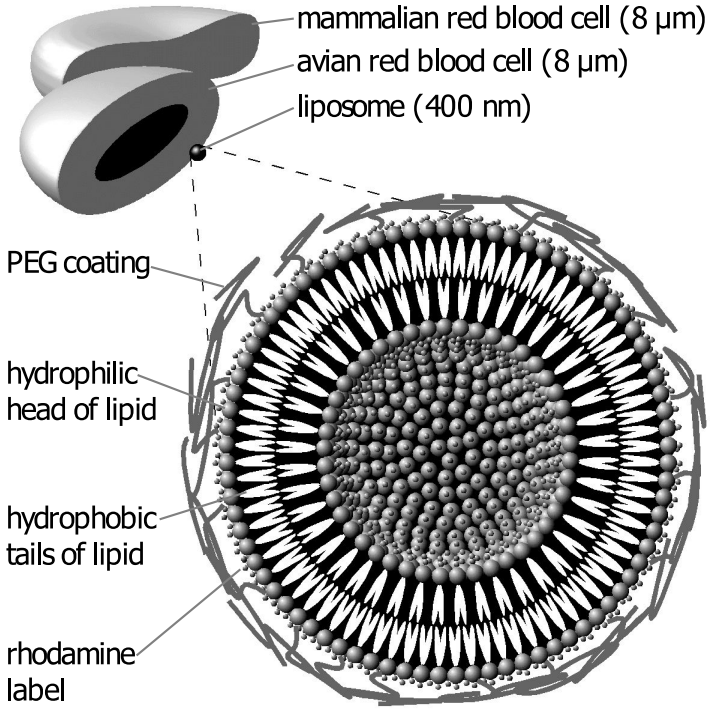

Figure 4.6: Schematic section of a PEG-coated liposome. The hydrophilic heads of the lipids are labeled with rhodamine molecules. The PEG-coating prevents the particles from adhering to the vessel walls.

that they are not as monodisperse. Furthermore the storage duration for polystyrene particles is in the order of months. The liposomes can be stored at most a few weeks. In terms of stability, coalescence is the biggest problem with the liposomes. The main stability limitation of the polystyrene particles is, that the rhodamine escapes from the particles with time. The particles can be washed by extracting the rhodamine contaminated solvent via a filter and replacing the extracted liquid by clean phosphate buffered saline (PBS), for example. In this way, the storage duration of the polystyrene particles can be increased beyond a year.

4.2 Triggered Measurement

In section 4.1.2 the cameras repetition rate of only 10 Hz was described as a shortcoming that had to be accepted because of light sensitivity reasons. Still, one of the demands on the current set-up is to enable at least a quasi continuous measurement of the blood flow in the pulsating embryonic chicken heart. Additionally, in section 4.4 it is shown that repetitive measurements at identical flow conditions can be used for the advantageous correlation averaging method.

For delivering the necessary triggering signal, an ultrasound Doppler velocimeter is chosen (figure 4.3). There are several reasons for preferring a sound based system over an electrical field based system or an optical method. Optical systems, using a photodiode for example [35], easily interfere with the pulsed laser illumination of the particle image velocimetry system. Furthermore, it would be necessary to place the optical sensor close to the heart, where the diameter change of the flow domain is strong enough to be optically detected. In this way, the microscope field of view may be impaired. Measuring the alternating electrical field of the heart would also deliver a triggering signal. Seidl et al. [146] report an electrocardiogram can be recorded for embryonic chicken hearts from HH-stage 11 onwards. The signal strength of a heart that has a mass 3000 times smaller than that of an adult human is extremely weak. The measurement of potential differences in the order of 10 μV require extensive electromagnetic shielding, that would heavily handicap the handling of the embryo and the optical assessment. Other cardiographic methods can be used for older embryos [69].

For the synchronization of the data-acquisition PC to the cardiac cycle of the chicken embryo, the acoustic probe of a 20-MHz ultrasound pulsed Doppler velocimeter (model 545C-4, Iowa Doppler Products) is placed close to the dorsal aorta of the embryo. The method is in detail described by Ursem et al. [172]. The tip of the probe holds a 750 μm piezoelectric crystal. The angle of insonation is approximately 30°. Moving blood cells reflect a frequency shifted echo that is transmitted to a computer after being quadrature demodulated, low-pass filtered and digitized. A LabVIEW (National Instruments) program extracts the maximum directional velocity from the audio signals in real-time by means of fast Fourier transformation (FFT) following the bispectral analysis methods demonstrated by Ursem et al. [172]. The camera and laser

are then triggered based on a threshold and slope criterion of the maximum velocity in conjunction with a constant, adjustable delay. The application of this technique is shown in section 5.1.

4.3 Non-triggered Measurement

Phase locking heart beat and image acquisition involves that the cameras repetition rate is matched to the heart rate, plus or minus a small phase shift. The data acquisition rate of the camera is thus not fully exploited. This may become a critical factor if one would like to use correlation averaging methods (see section 4.4) while resolving the temporal velocity distribution during a full cardiac cycle at a number of parallel planes. Simply because of the development of the chicken, the flow conditions can only considered to be constant during a time-period of order one hour. When minimization of the measurement duration is an issue, one might consider non-triggered measurements.

Non-triggered measurements rely on the accurate determination of the cardiac phase angle for each single measurement. If the heart rate would be perfectly constant, a simple frequency analysis would be sufficient for determining the position of each measurement within the cardiac cycle. The following procedure also accounts for a slight, natural frequency jitter[14].

1. Recording of image pairs at the technically highest possible framerate.
2. Evaluation of each single measurement on a coarse grid.
3. Plotting the average velocity of each measurement along a timeline[15] (figure 4.7, top graph).
4. Detection of all systolic peaks along the timeline.
5. Refinement of systolic peak position determination with sub-sample accuracy by a peak fitting procedure (figure 4.7, third graph). In this specific example, simple three point estimators tend to lock to the positions of the center samples. Therefore a flow model ([11], figure 4.8) is fit to a data segment that has the length of three periods, respectively. The four parameters offset, amplitude, angular frequency, and phase shift, are adjusted by a least square method during the peak detection procedure to fit the measurement data. An initial guess for the angular frequency is derived from a frequency analysis (figure 4.7, second graph).

[14] In figure 4.7, second graph, the width of the main peak at 1.5 Hz indicates a frequency variation of the heart rate of slightly less than 5 % of the pulse duration.

[15] One may alternatively use any other periodic property of the measurements that alternates with the same frequency as the heart beat. This may be the average brightness of the pixel images, the root mean square deviation of the velocity data, the average velocity at a predefined sub-region of the image, the average correlation peak height, etc.. The other steps of the evaluation procedure need to be adapted to this dimension, of course.

6. Assigning each measurement a cardiac phase angle between 0 and 1 according to their relative temporal position between two adjacent peaks.
7. Sorting all measurements according to their cardiac phase angle (figure 4.7 bottom graph).
8. Dividing the whole period into a number of time segments.
9. Evaluating each group (time segment) on a fine grid using correlation averaging (see section 4.4 for correlation averaging).

The application of the whole procedure is shown in section 5.3

4.4 Image Evaluation

The basic principle of a particle image velocimetry evaluation was explained in the first paragraph of section 3.3. As described by Meinhart et al. (2000) [117], the reliability of a particle image velocimetry evaluation can be significantly enhanced by taking the average of the correlation results of multiple measurements (ensemble correlation). This technique is especially advantageous at conditions with low seeding density and poor particle visibility over the background glow. These are typical conditions in blood flow applications. The average correlation technique requires a set of measurements at exactly the same flow conditions. This is a reason why proper phase-locking of the data-acquisition system to the periodic blood flow of the chicken heart (section 4.2), or alternatively, the exact reconstruction of the acquisition time in terms of cardiac phase (section 4.3) is important. An averaged-correlation function is gained by summing up all cross-correlation functions for a specific interrogation window over a number of individual image-pairs. The averaged-correlation function is characterized by a much higher signal-to-noise ratio than the instantaneous cross-correlation functions, so that the measurement reliability can be greatly improved (figure 4.9).

The velocity data may also be used for objectively determining the inner lumen boundary of the heart. Assuming the no-slip velocity condition at the wall, the wall position is readily available by extrapolating the measured velocity profile to zero. This approach was used by Stone et al. [159] to determine wall positions with an accuracy approaching tens of nanometers. This method is only valid when the vessel wall is not moving, or in other words, when the velocity of the vessel wall is small, when compared to the fluid velocity. The wall movement of a contracting heart is dominated by the radial velocity component[16]. A quick order of magnitude estimate for the ratio of the mean fluid velocity and the radial wall velocity can be made by considering a compressed tube[17] as sketched in figure 4.10. Volume conservation reveals that the

[16] A small oscillation of the whole heart between its anchor points leads to a negligible axial velocity component.

[17] Whether the embryonic heart is compressed in radial direction or flattened in two dimensions is without significant influence.

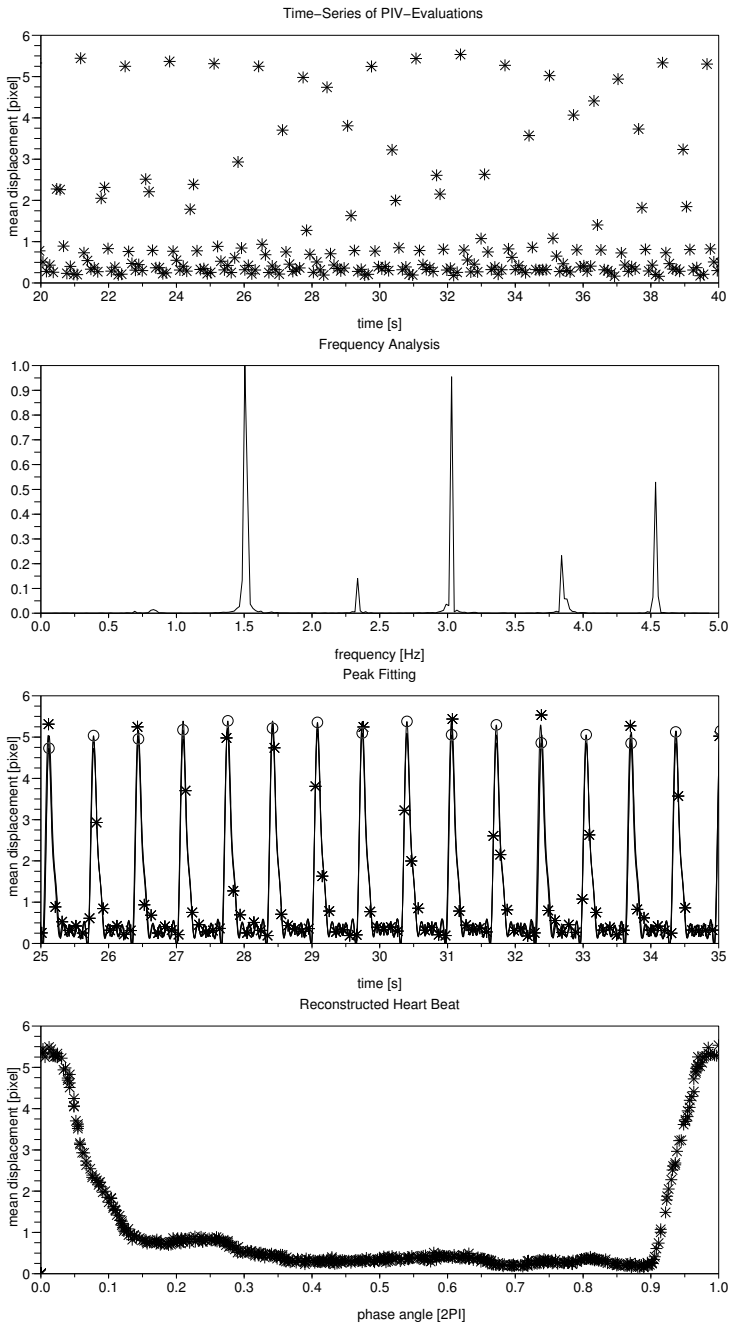

Figure 4.7: Data sorting procedure. Top graph: Mean displacement for each of 5000 single particle image velocimetry evaluations. Second graph: frequency analysis for estimating initial fitting parameters. Third graph: Determination of systolic peak flow positions on time axis. Bottom graph: Realignment of the single measurements along the cardiac cycle. To reveal more detail, just a fraction of the data points is shown in the top three graphs. The regular wave pattern of the measurement points in the top graph results from the camera frequency and the heart rate interfering with each other.

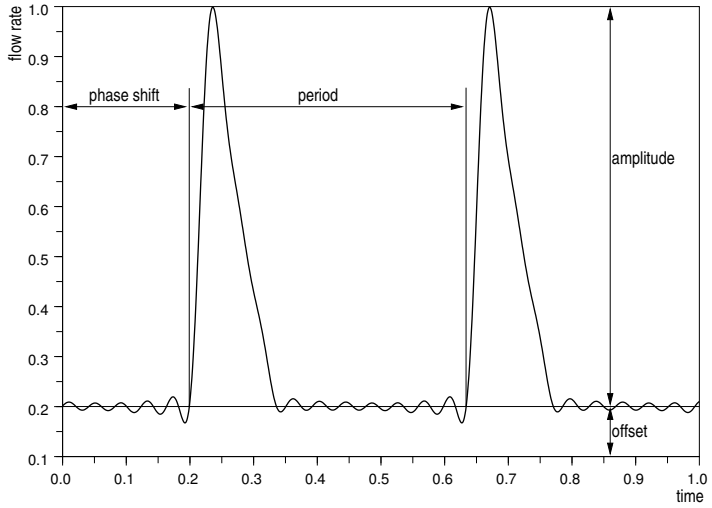

Figure 4.8: The aortic flow rate can be modeled by the superposition of harmonics [120]. Here, the first ten harmonics found by Milnor [120] are used. They are characterized by the modulus, r_n = 110, 202, 157, 103, 62, 47, 42, 31, 19, 15, 15, and the phase, p_n = 0, -0.78, -1.50, -2.11, -2.46, -2.59, -2.91, 2.92, 2.66, 2.73, 2.42, with $n = 0 \ldots 10$. The plot above is then given by $q = o + \Sigma_{n=0}^{10} a \cdot r_n \cdot [cos(p_n) \cdot cos(n\omega(t - s)) - sin(p_n) \cdot sin(n\omega(t - s))]$. The four parameters offset, o, amplitude, a, angular frequency, ω (or period, $p = 2\pi/\omega$), and phase shift, s, are adjusted by a least square method during the peak detection procedure to fit the measurement data. The time in the equation above is denoted by t.

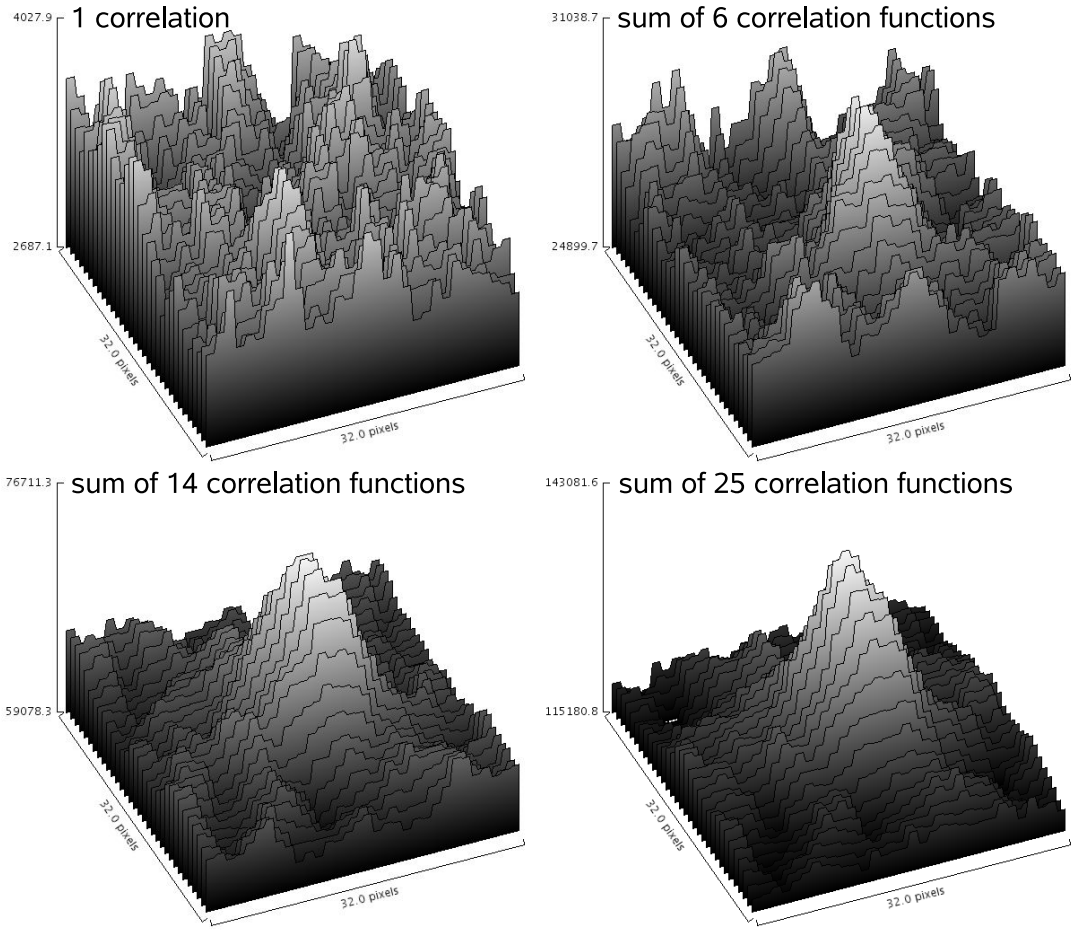

Figure 4.9: A typical example for averaging a correlation function. Noise is more effectively suppressed with increasing number of correlation instances. This example corresponds to the third evaluation pass of the vector in figure 5.7 that is marked with a white square. The sample is characterized by an intermediate displacement of about 14 pixel and rather large scanning depth (plane 11 out of 14). At a shorter displacement and a smaller scanning depth, the peak converges faster towards its final shape.

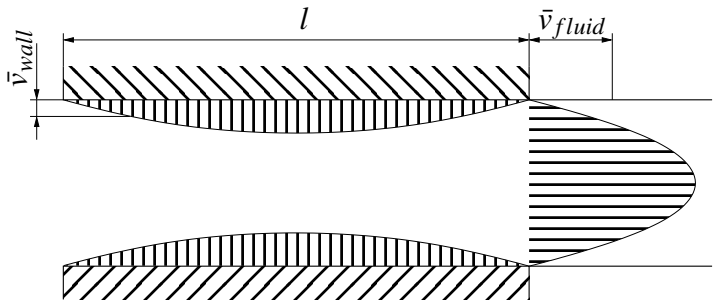

Figure 4.10: Simple approximation of a compressible tube to estimate the ratio of the mean velocities of the inwards moving wall $\bar{v}_{wall}$ and the expelled fluid $\bar{v}_{fluid}$. The fluid is completely ejected at one side of the tube. Volume conservation $\bar{v}_{wall} \cdot 2\pi rl = \bar{v}_{fluid} \cdot \pi r^2$ leads to $\bar{v}_{wall}/\bar{v}_{fluid} = r/2l$.

ratio of the mean velocities of the wall and the expelled fluid, $\bar{v}_{wall}/\bar{v}_{fluid}$, can be estimated by the ratio of the current tube radius and twice the length of compressed tube section $r/2l$. Assuming, that the length of the centerline of the embryonic hart is about 2 mm, the inner radius is at most 0.1 mm, and half of the length of the heart is compressed at a time, the velocity of the wall, $\bar{v}_{wall}$, is at most $1/20^{th}$ of the fluid velocity, $\bar{v}_{fluid}$. This ratio quickly decreases further with diminishing vessel radius.[18]

Alternatively the phase averaged image intensity can be utilized for determining the wall position: By averaging over all image frames of the ensemble, the plasma region containing the fluorescent tracer particles appears as a bright region, while the rest of the image remains dark. The inner lumen boundary is then determined as shown in Figure 4.11.

4.5 Resolution Aspects

Every velocity vector that is obtained by means of particle image velocimetry represents the average velocity of a particle pattern within a small evaluation volume. The size of the evaluation volume is defined in Cartesian coordinates. The axes x and y define the dimensions parallel to the imaging plane, z perpendicular to the image plane. The physical size of the evaluation volume, which is equivalent to the resolution of the measurement, is determined by four factors:

- the magnification of the microscope objective,

[18] In principal, only the axial velocity component is relevant for the wall shear stress. Decomposing the velocity in an axial and in a wall normal component and extrapolating the axial velocity profile to zero would indicate the current wall position, regardless of the radial wall movement. Given the small magnitude of the radial velocity component, this approach would not help. The uncertainty in the determination of the axial coordinate direction would lead to a radial velocity uncertainty of the same magnitude as the actual wall velocity.

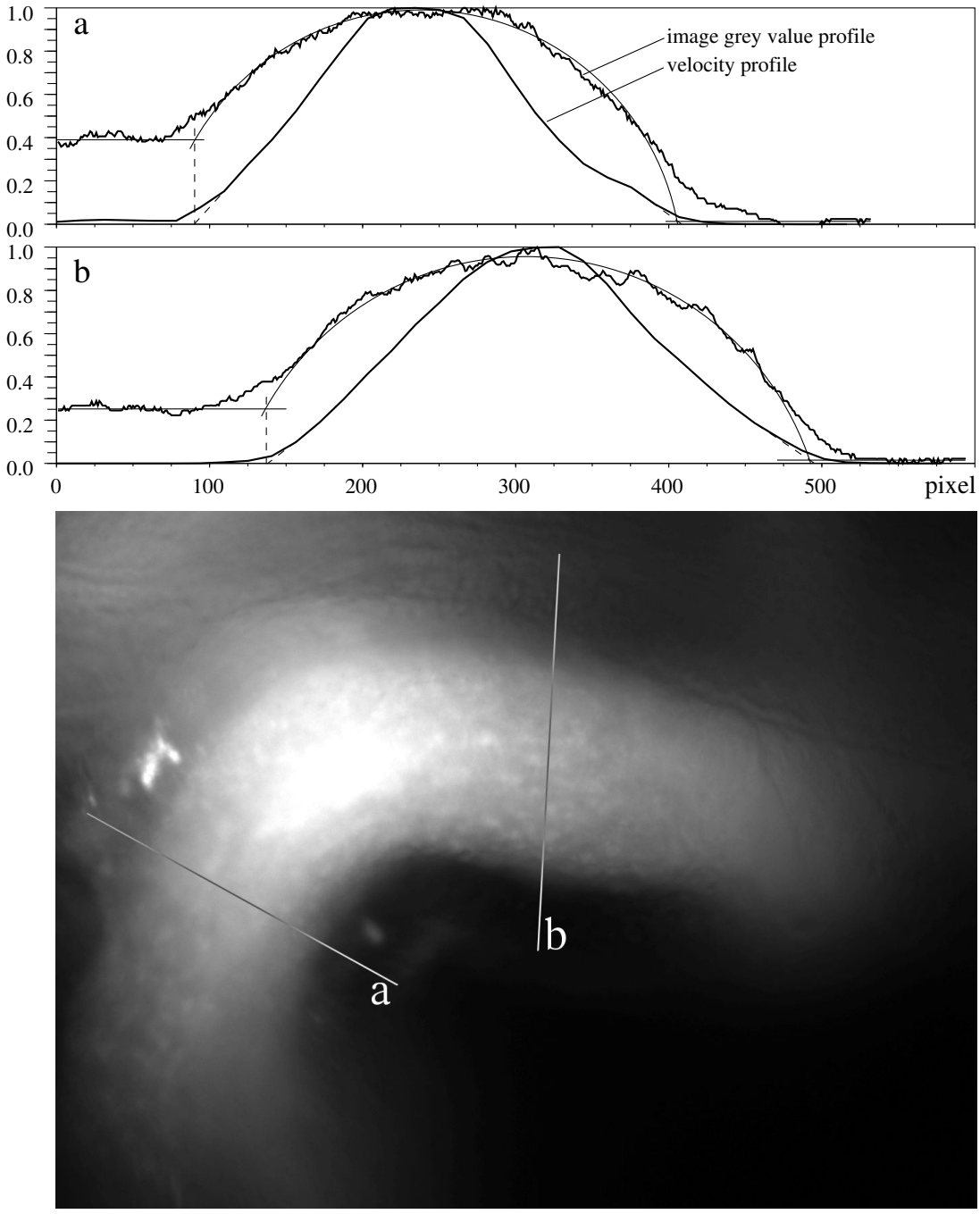

Figure 4.11: The average of 100 image frames at maximum systolic flow, reveals the inner lumen boundary as a bright region. Due to the approximately circular cross section of the vessel, also the theoretical grey value intensity function has a circular shape. The intersection points of the theoretical intensity profiles and the grey level offsets of the neighboring regions accurately define the position of the vessel wall. Additionally, the velocity profiles at the same positions are plotted. The extrapolation of the velocity profiles to zero, while omitting the vectors whose interrogation regions overlap with the wall, also reveals the flow boundary. Both detection mechanisms match fairly well, indicating that at maximum dilatation, the wall is indeed not moving.

- the pixel size of the camera,
- the width and the length of the correlation window,
- and the thickness of the correlation plane.

The dimension of the evaluation volume parallel to the image plane is directly defined by the first three factors magnification, pixel size, and correlation window dimension. The third dimension of the correlation volume can not be defined that clearly. Not only focused particles contribute to the correlation result, also defocused particles do, even though their influence diminishes with increasing distance to the focal plane. Theoretically, the thickness of the layer that influences the correlation result extends to infinity. However, when a threshold, ε, for the influence of defocused particles on the correlation is defined, a definite number for the thickness of the correlation layer, the depth of correlation, δ_{corr}, can be given. Olsen and Adrian [125] derived an expression (equation 4.1) for calculating δ_{corr} from the particle diameter, d_p, the optical magnification, M, the numerical aperture of the objective, NA, and the wavelength of the light emitted by the particles, λ. Equation 4.1 is a combination of geometric optics (first term, containing the particle diameter, d_p) and diffraction (second term, containing the wavelength, λ). As a threshold ε they suggested to use the ratio of the contribution to the correlation result of a particle at the edge of the measurement layer and a particle in the focal plane. Throughout this thesis a threshold of 0.01 is used. Thus, the boundary of the correlation layer is defined at the distance where particles have less than one percent of the influence on the correlation than a perfectly focused particle has.

$$\delta_{corr} = 2\left[\frac{1-\sqrt{\varepsilon}}{\sqrt{\varepsilon}}\left(\left(\frac{1}{2NA}\right)^2 d_p^2 + \frac{5.95(M+1)^2\lambda^2\left(\frac{1}{2NA}\right)^4}{M^2}\right)\right]^{\frac{1}{2}}. \qquad (4.1)$$

Figure 4.12 visualizes the influence of particle size and magnification on the depth of correlation. For a wide field of practically relevant magnifications above 10× and particle diameters below 1 μm, the z-dimension of the measurement volume, δ_{corr}, is found to be below 10 μm. For example, at a magnification of 20× and a particle diameter of 500 nm, δ_{corr} is about 9 μm. For erythrocytes of 8 μm diameter, however, the theoretical correlation depth would be almost 50 μm (beyond the plotting range in figure 4.12).

4.6 Parallel Plane Measurement

Measurements with a single camera in a single plane deliver information about the two-dimensional projection of three-dimensional velocities. Shear stress values can only be derived where the in-plane velocity component is known. For the embryonic chicken heart, this is only the case along lines with flow parallel to the imaging sensor.

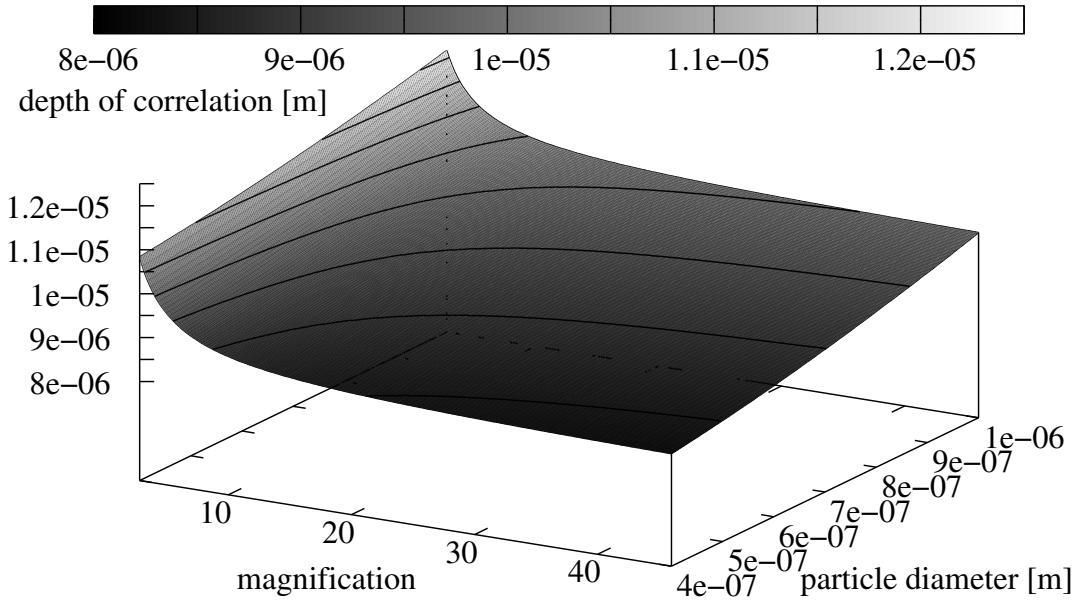

Figure 4.12: Depth of correlation for $\varepsilon = 0.01$, thus defining the influence of a particle image on the correlation function to be insignificant when it drops below one per cent of the influence that a perfectly focused particle has, $NA = 0.5$ (see section 4.1.2), and $\lambda = 560$ nm. Particle diameter and magnification are variable.

For accessing the whole three-dimensional velocity distribution, there are basically three possibilities[19].

1. Extending the single view, single plane measurements to single view, multiple planes, and deriving the third velocity component numerically using the continuity equation [23, 141].

2. Using a two-camera set-up for stereoscopic measurements, to determine all three velocity components by reconstruction from the two observed displacements like shown by Lindken et al. [100].

3. Performing tomographic or photogrammetric measurements with a minimum of two cameras [51, 101, 108].

The hardware, as described in section 4.1, in principle allows for the implementation of all three techniques. Each of those methods have a number of strong points and some limitations that should carefully be weighed against each other, before a method is chosen.

[19] A future possibility might be holographic particle image velocimetry. The current development status [126] in terms of spatial and temporal resolution does not allow the application on the problem treated in this thesis.

The main advantages of the first method over the other two is that for a single view optical system the highest optical resolution, the highest tracer particle density and the smallest particle diameter can be used. These advantages are related to the fact that an optical system with higher resolution and higher light efficiency can be used. A disadvantage is that certain assumptions about the flow need to be made. These assumptions are conservation of mass, incompressibility, and a boundary condition like known mass flux or known velocities in certain regions to start the integration. In practice, most micro particle image velocimetry applications use liquids as working fluids and confined channel geometries where the no slip condition holds within the measurement accuracy. The above mentioned prerequisites for the numerical reconstruction of the velocity field are therefore almost always fulfilled. The most severe disadvantage of this technique is that the accuracy of the reconstructed third velocity component is up to one order of magnitude lower than the two measured velocity components (derived in section 4.7.2).

Compared to the other two approaches, tomographic particle image velocimetry is the only really three-dimensional technique. The position of every tracer particle in space is reconstructed from two ore more camera images. Because no scanning is necessary, tomographic measurements are very useful for applications that demand high temporal resolution. The unambiguous reconstruction of the particle position requires unfortunately that the seeding density must remain below a specific value [51]. The application on the flow in the embryonic chick embryo would require a focal depth of 100 μm at a magnifications of 18 $\times$ (compare to section 5.3). This is currently not feasible. The mechanical set-up of a tomographic particle image velocimetry system is somewhat simpler than the other two approaches, because no movement of the camera or measurement volume is necessary. Stepping-motors or piezo-devices can thus be omitted.

An important advantage of stereoscopic measurements is, that every single measurement already delivers all three velocity components. For obtaining the three dimensional flow field in a volume, also this technique requires the successive measurement at a number of parallel planes. An important disadvantage is the usage of stereoscopic objectives which usually have a low numerical aperture and therefore large focal and correlation depth, which involves low light efficiency and larger averaging effects along the optical axis. The difficult optical conditions that are associated with measurements in the embryonic chicken heart currently do not allow the usage of standard stereoscopic optics. Therefore, the numerical reconstruction of the three dimensional flow field from multiple plane measurements is the only practical option.

4.7 Reconstruction of the Third Velocity Component

4.7.1 Method

Mass conservation for incompressible flow can be expressed mathematically, by stating that the divergence of a flow field equals zero.

$$\nabla \cdot \vec{u} = \frac{\partial u_x}{\partial x} + \frac{\partial u_y}{\partial y} + \frac{\partial u_z}{\partial z} = 0 \tag{4.2}$$

Here, $\vec{u}$, denotes a velocity vector in Cartesian coordinates, u_x, u_y, and u_z its components. For discretizing the equation on the measurement grid, the differentials are approximated by finite differences at each measured data point, $i(x,y,z)$, in the velocity fields (equation 4.3). Central differences are used as they are more accurate than first-order differences. The in-plane grid spacing is denoted by dx and dy, respectively, and the distance between the measurement planes by dz:

$$\nabla \cdot \vec{u} \approx \frac{u_{x_{(x_i+dx)}} - u_{x_{(x_i-dx)}}}{2dx} + \frac{u_{y_{(y_i+dy)}} - u_{y_{(y_i-dy)}}}{2dy} + \frac{u_{z_{(z_i+dz)}} - u_{z_{(z_i-dz)}}}{2dz} \tag{4.3}$$

The first two terms, i.e. the velocity gradients in x- and y- direction, can readily be computed from the measured in-plane velocity data (u_{x_i} and u_{y_i}) and the grid spacings. Solving equation 4.3 for $\nabla \cdot \vec{u} = 0$ gives the velocity gradient in z-direction for every data point. If the top measurement plane is just outside of the flow field, all values are zero in this plane. This plane can then be used as a starting point for integrating (summing) the velocity gradients along z to obtain absolute values for all u_{z_i}. The actual integration is done using forward differences.

4.7.2 Accuracy and Sensitivity

The accuracy of the reconstructed third velocity component is limited by

1. a systematic bias due to discretization,
2. noise that is introduced by the PIV evaluation, and
3. spatial averaging due to the finite interrogation window size of a PIV evaluation.

The sensitivity of the reconstruction method to discretization bias, noise and spatial averaging varies upon the grid spacing in plane and along z. This relation can be evaluated by means of artificially generated velocity data and synthetic particle images. To distinguish between the sensitivity to discretization bias, noise, and spatial averaging, the reconstruction is calculated for the following three cases:

1. artificially generated velocity data,

2. artificially generated velocity data plus homogeneous, random noise with a standard deviation of 0.1 pixel, and

3. PIV evaluations of synthetic particle images that were generated based on the artificially generated velocity data of point one.

All three cases are combined with various grid spacings (in-plane: 8, 16, 32, and 64 pixel, z-direction: equivalent to 8, 16, 32, 64, and 128 pixel). A Poiseuille flow through a circular cylinder is taken as a test case. The cylinder is tilted 45 degrees relative to the z-direction and turned 45 degrees relative to the in-plane grid orientation[20]. The top and bottom planes are completely outside the flow field. In the case of a z-grid spacing of 8 pixel, there are 220 planes in total. By adjusting the diameter of the tube and the maximum displacement, the velocity gradients and displacements are matched to the magnitudes of realistic in-vivo measurements in an embryonic chicken heart. The standard deviation of the reconstructed velocity component from reference data is plotted in figure 4.13. The left column (figure 4.13 a, c, and e) shows the deviation for the center plane (in the middle of the flow field), the right column (figure 4.13 b, d, and f) shows the deviation for the bottom plane. The first row (figure 4.13 a and b) represents the case of artificially generated data, the middle row (figure 4.13 c and d) the case of noisy data, and the last row (figure 4.13 e and f) the case of a reconstruction from PIV images.

Here a description is given of the results presented in figure 4.13.

- Figure 4.13 a and b: In general, the discretization error is lower for smaller grid spacings. A minimum bias exists for equal grid spacings in-plane and in the z-direction, indicating that the discretization errors in both directions compensate each other to some extent.

- Figure 4.13 c and d: A finer z-grid is generally beneficial, because random noise is canceled out when the number of integration planes becomes high. A fine in-plane grid appears to be contra-productive. Local velocity gradients are calculated from central velocity differences, divided by twice the grid spacing. The smaller the denominator (twice the in-plane grid spacing, $2dx$, $2dy$, respectively), the higher the influence of a noisy numerator.

- Figure 4.13 e and f: In addition to the disadvantageous influence of noise, especially at small in-plane grid spacings, there is a negative influence of spatial averaging for large grid spacings (large interrogation windows), so that there is an optimum at $dx = dy = 32$ pixel. The vertical grid spacing is without significant influence on the final accuracy (except for the case of 8 pixel in-plane grid spacing). Using a small z-grid spacing, the systematic deviation due to in-plane

[20] In such a symmetric case, most deviations become obvious on first sight. Here the velocity components in plane must be equal. The absolute in plane velocity must be identical to the z-component.

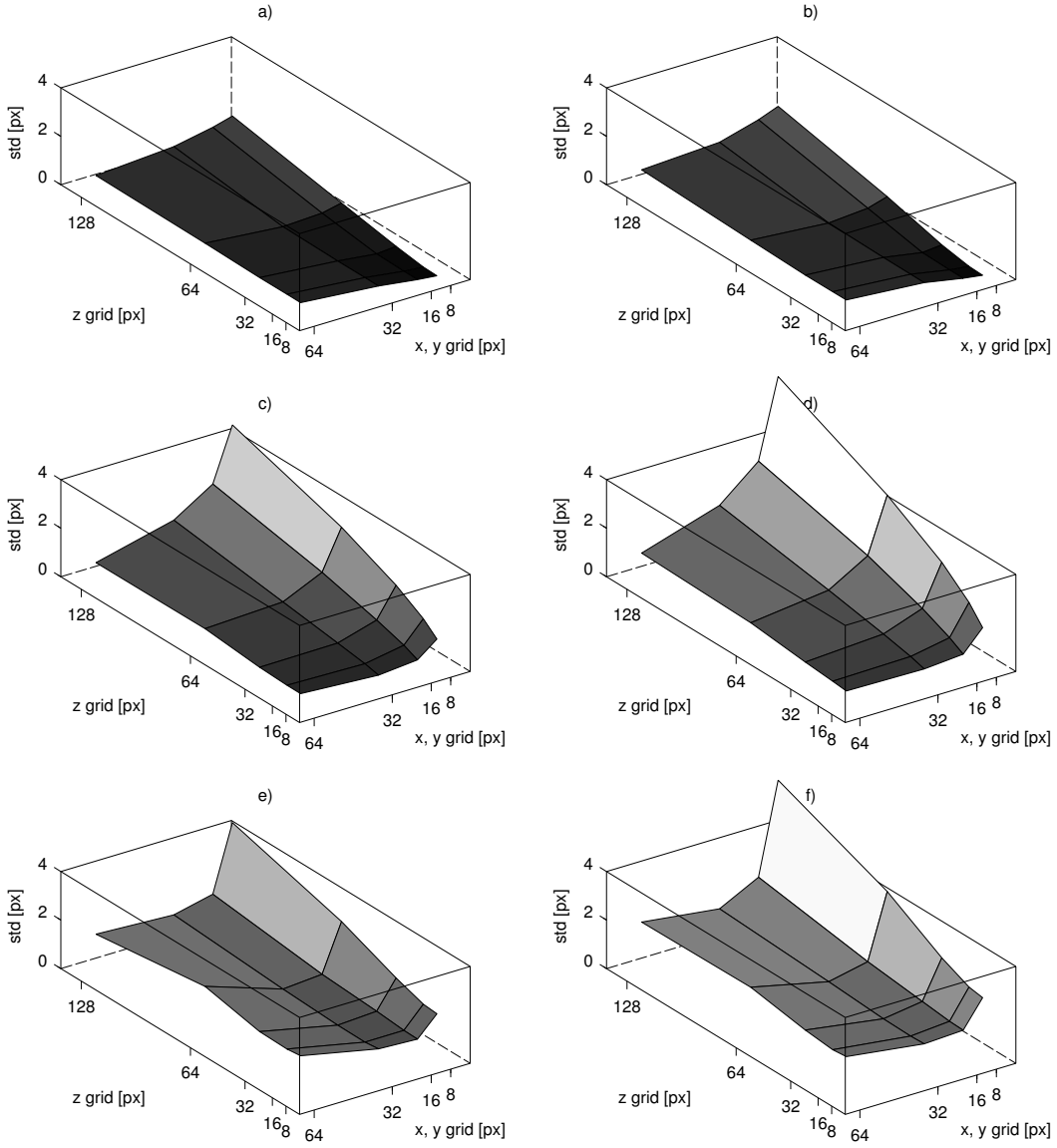

Figure 4.13: Standard deviation of the reconstructed out-of-plane velocities from reference data for various grid spacings in plane (x-, y-direction) and plane-normal (z-direction). The left column (a, c, e) shows the deviation for the central plane, in the middle of the flow field. The right column (b, d, f) shows the deviation of the bottom plane, outside the flow field. The first row (a, b) represents the reconstruction from exact data, the middle row (c, d) the reconstruction from noisy data, and the last row (e, f) the reconstruction from PIV evaluations.

spatial averaging adds up, random noise on the other hand is compensated. Using a large z-grid spacing, the systematic deviation due to in plane spatial averaging does not become significant, but random noise is not sufficiently suppressed. As long as the optimal range for the in-plane grid spacing is chosen, the value for the vertical spacing is not crucial, after all. For large in-plane grid spacings, the integrated effect of spatial averaging at smaller z-grid spacings might even be larger than the influence of non-compensated noise at a lower number of integrated planes, so that a slight local deviation maximum exists at a z and in-plane grid spacing of 64 pixel.

The quality of in-vivo PIV measurements is expected to be a bit lower than in the simulated case. This might lead to a larger loss of accuracy at small grid spacings. Therefore a grid spacing of 32 pixel seems to be optimal. Unfortunately, this is a rather coarse grid. The simulation showed, that random noise is the most severe problem at smaller grid spacings. To get both a flow measurement at a reasonable resolution and the benefit of large grid spacings to reduce the influence of noise, one could think of calculating the velocity gradients on a larger grid than the PIV evaluation. This can be done by not taking the central difference of points next to the central point, but one grid point further apart. To further suppress noise, the central difference approximations for $\frac{\partial u_x}{\partial x}$ and $\frac{\partial u_y}{\partial y}$ in equation 4.2 might be replaced by the gradient of a linear regression function over five points.

$$\frac{\partial u_x}{\partial x} \approx \frac{\sum_{n=-2}^{2} (x_{i+n} - x_i)\left(u_{xi+n} - \overline{u_x}\right)}{\sum_{n=-2}^{2} (x_{i+n} - x_i)^2}, \quad \frac{\partial u_y}{\partial y} \approx \frac{\sum_{n=-2}^{2} (y_{i+n} - y_i)\left(u_{yi+n} - \overline{u_y}\right)}{\sum_{n=-2}^{2} (y_{i+n} - y_i)^2} \tag{4.4}$$

This method has been tested and the results are plotted in figure 4.14. The impact of noise at small in-plane grid spacings is efficiently suppressed, while other regions of the study domain are not affected. This method is only useful for larger flow structures, of course, and will produce artifacts when discontinuities in the velocity field are present.

For the application of the numerical reconstruction on measurement data of the embryonic chicken heart, the linear regression scheme and an in-plane grid spacing of 16 pixel are optimal. The vertical grid spacing is without significant influence in this case.

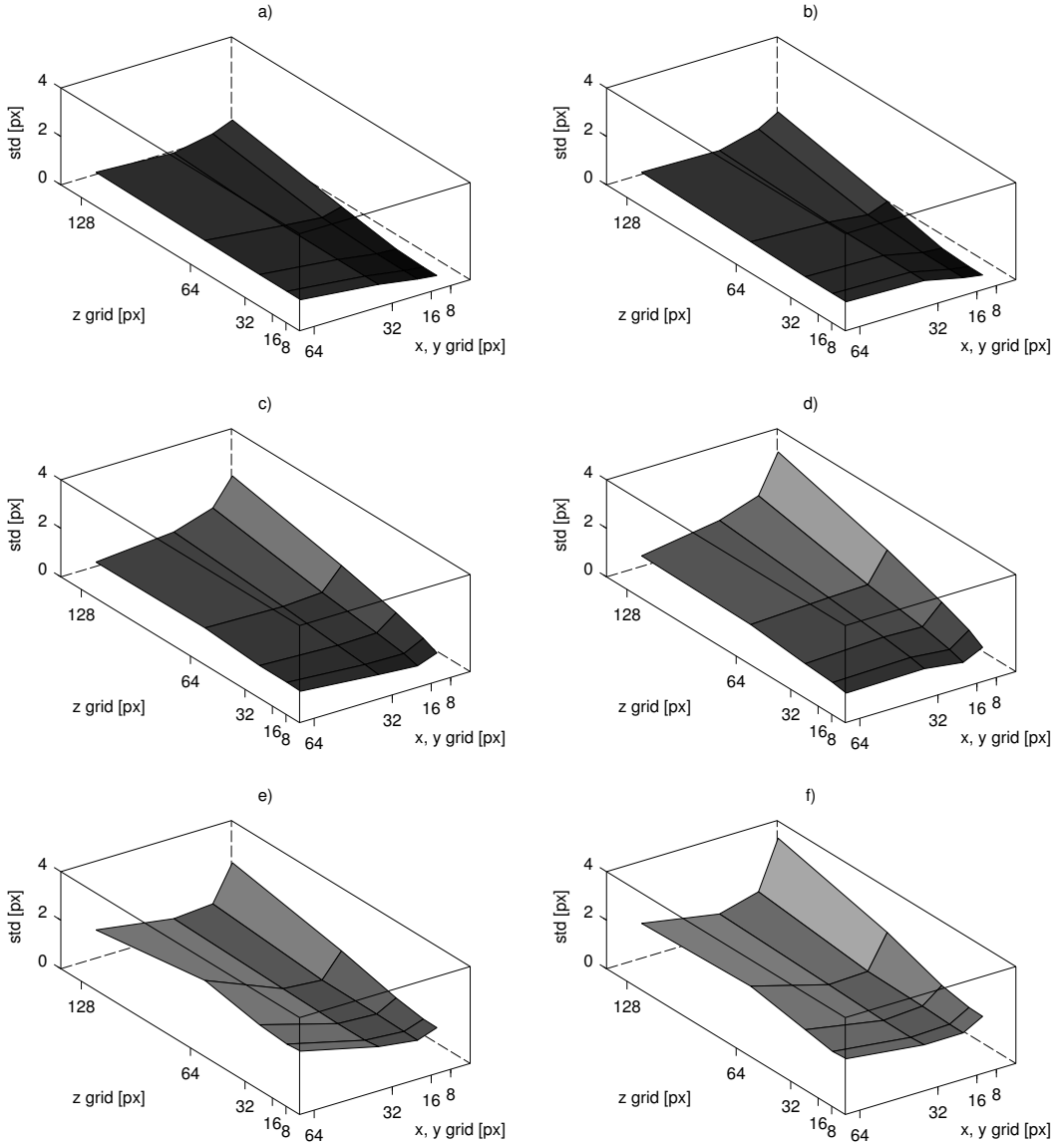

Figure 4.14: The standard deviation of the same cases as shown in figure 4.13 with the only difference that for the calculation of equation 4.3 the central difference approximations for $\frac{\partial u_x}{\partial x}$ and $\frac{\partial u_y}{\partial y}$ are replaced by equation 4.4. The standard deviation from reference data is reduced by a factor of two for small in-plane grid spacings.

Chapter 5

Applications

5.1 Triggered Measurements

This section was partially published previously in the Journal of Biomechanics [175]. The main purpose of these early published measurements are to demonstrate that micro particle image velocimetry has the potential to develop into a general tool for instationary flow conditions in complex flow geometries encountered in cardiovascular research and its capabilities to extract quantitative information of the velocity field and wall shear stress in in-vivo measurements in an embryonic chicken heart. Additionally, in relation to previously published gene-expression experiments [64], these first results underline the significance of fluid forces for embryonic cardiogenesis.

5.1.1 Animals

Fertilized White Leghorn eggs are incubated until they reach HH-stage 15. Part of the egg shell is removed like described in section 4.1.1 to establish optical access. Mineral oil is used to prevent desiccation by evaporation. A stable heart rate of about 120 ± 4 beats per minute indicated unperturbed conditions throughout the analysis. The cardiac outflow tract (developing right ventricle) containing the endocardial cushions is visualized without mechanical manipulation of the embryo (figure 4.1). High levels of mRNA from genes that have been shown to up-regulate expression under high shear stress conditions can be detected in this region of the embryonic heart [64]. The developing atrial compartment could be measured from an embryo that showed a natural "right-side-down" positioning on the yolk sac.

5.1.2 Experimental Set-Up

The experimental set-up is comparable to the final configuration as described in section 4.1 and illustrated in figure 4.3. The main difference is that for this first experiment a different microscope is tested (Leica DM4000B with Leica HC PLAN APO

10×/0.40). Triggering is done by means of an ultrasound Doppler velocimeter like described in section 4.2. The synchronization of the camera, the laser, data acquisition, and data storage are done by means of a commercially available computer system with a built in timing unit (LaVision PTU 8). Data-acquisition PC and cardiac cycle are synchronized like described in section 4.2. The liposome tracer particles (section 4.1.4) are injected into one of the vitelline veins using an approximately 10 μm thick glass-needle. A separate stereo-microscope is used for the injection.

5.1.3 Evaluation

As mentioned in section 4.4 the reliability of a particle image evaluation can be significantly enhanced by correlation averaging. This is especially advantageous at conditions with low seeding density and poor particle visibility over the background, which are typically found in blood flow applications. To ensure that the images of an averaged set are taken at identical flow conditions, phase locking is used as described in section 4.2. A set of 50 images is obtained within 25 seconds, which is a time period where variations in conditions and physiological changes of the developing heart can be considered negligible.

The effectiveness of the correlation averaging method is evaluated by considering a measurement in the fully dilated ventricle. At this point of the cardiac phase the velocity is maximized and the tangential and radial velocity of the wall is minimized. The final velocity field is shown in the left part of figure 5.1, and will be discussed in detail in the Results section. The interrogation window was selected to be 64×64 pixel in size, with 50 percent overlap between subsequent interrogations, which leads to a 32 pixel vector spacing, equivalent to 20.6 μm (about one tenth of the inner lumen diameter). With a time difference of 0.5 ms between two frames, a velocity of 20 mm/s corresponds to a particle displacement of about 16 pixel, in correspondence to the optimal displacement recommended by Keane and Adrian [85] for this interrogation window size. To get an estimate for the number of image pairs that are necessary to obtain a reliable velocity measurement, the percentage of valid data (where the correlated signal peak can be clearly identified with respect to the background noise) can be determined as a function of the number of image pairs that are considered for the ensemble correlation. In figure 5.2, the percentage of valid velocity vectors is plotted as a function of the number of summed correlation functions. Using a 64×64 pixel interrogation window size, only five image-pairs (corresponding to an acquisition time of 2.5 seconds) are sufficient to obtain more than 90 % valid vectors under the current optical conditions. Using fifty image-pairs increases the validity ratio close to 100 %, with little further improvement beyond this point. Smaller interrogation windows contain proportionally less information and, therefore obtaining a similar fraction of reliable vectors requires a corresponding increase in the number of images. Hence, the number of images that is required for the ensemble correlation further increases with decreasing size of the interrogation window (i.e. the curve in Figure 5.2 shifts to the right).

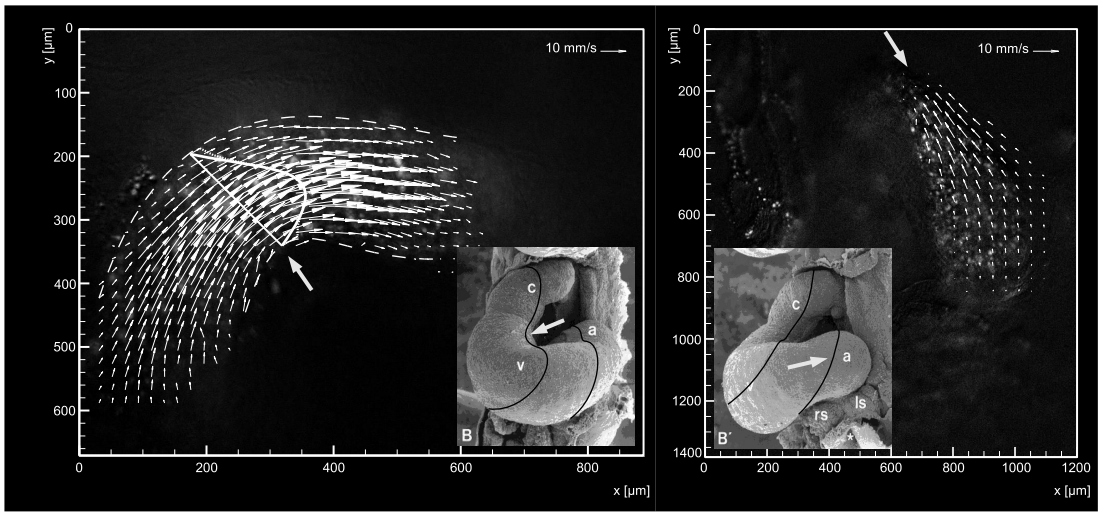

Figure 5.1: Velocity distributions in the developing ventricle (left, 10× magnification) and in the atrium (right, 5× magnification) of a HH-stage 15 chicken embryo. A representative profile depicting the local ensemble-averaged, axis-normal velocity magnitude is superimposed on the vector field. The approximate lumen boundary is indicated by two dashed lines that are readily determined by interpolating the velocity profiles to zero. The location and spatial orientation of the measurement planes relative to the looping heart are indicated in the scanning electron micrographs from [112].

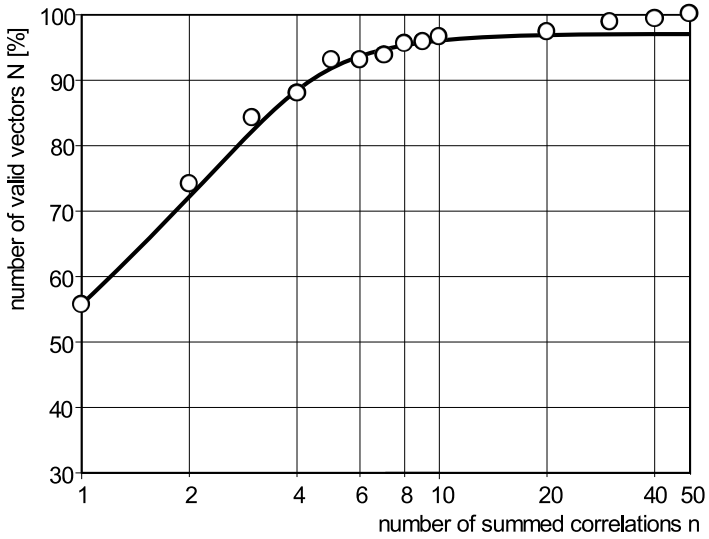

Figure 5.2: Percentage of reliable vectors as a function of the number of summed correlation functions. If interrogation areas of 64×64 pixel are used, 50 image pairs are sufficient to obtain close to 100 % reliable vectors.

5.1.4 Results

Measurements are made at nine discrete points in the cardiac cycle, and are separated from each other by 50 ms. Each measurement represents the correlation averaged evaluation of up to fifty image pairs with an interframing time of 0.5 to 4 ms, depending on the average magnitude of the velocities at a given point in the cycle. Given that a chicken embryo typically has a heart rate of 2 Hz, it follows that a single ensemble measurement requires 25 seconds to complete. The spatial resolution of the velocity data is estimated at $41 \times 41 \times 13$ μm^3 (see section 4.5).

Figure 5.3 gives an overview of the measured velocity distributions at different points in the embryonic cardiac cycle. The black lines mark the focused part of the inner surface of the endocardium. The flow enters from the left side of each image where the blood emerges perpendicular to the image plane. After crossing the measurement plane, the flow disappears again normal to the image plane in the direction of the pharyngeal arch arteries. The first frame of figure 5.3 shows the imaged part of the heart-tube being tightly closed. After 50 ms the tube is opened to a small slit, with the peak velocity rising to 3 mm/s.

It takes approximately 250 ms to fill the ventricle at these relatively low blood flow rates. When the imaged part of the tube is completely expanded (after 300 ms), a rapid peristaltic contraction has already started further upstream, providing a forward impetus that accelerates the fluid in the measurement plane to a peak velocity of 26 mm/s. The corresponding Reynolds number is about 0.5 at this point which indicates that this flow is mainly determined by viscous forces, but that inertia can not be fully ignored. The Womersley number for the adjacent arteries is of order 0.2. The velocity map corresponding to this point of the cardiac cycle is shown in more detail in the left part of figure 5.1. The background shows a sample particle image for orientation.

The dashed white lines in figure 5.1 mark the inner lumen boundary in the focused part of the endocardium. In this system only the velocity components parallel to the focal plane are measured. This explains why the axial velocity magnitude decreases to the left and to the right side of the flow field, as the main flow direction is not parallel to the focal plane in these regions. From the flow field, velocity profiles can be determined. At the cross-section indicated by a straight line, the flow is assumed to be parallel to the image plane, so that the third velocity component becomes zero. At this position a single velocity profile is superimposed as a continuous curve. The profile clearly shows an asymmetrical velocity distribution which suggests the highest shear stresses will appear at the inner curvature. This effect is also found by Bugliarellos group [79, 80]. Evidently, the conventional method of estimating the wall shear stress from the characteristic vessel diameter and the maximum velocity (as applies to fully developed laminar pipe flow) does not apply in this configuration.

The remaining portion of the cardiac cycle is depicted by the last two frames of figure 5.3. The peristaltic movement of the heart muscle enters the measurement plane from the left side and pushes the blood out to the right until the entire imaged portion of the tube is closed again.

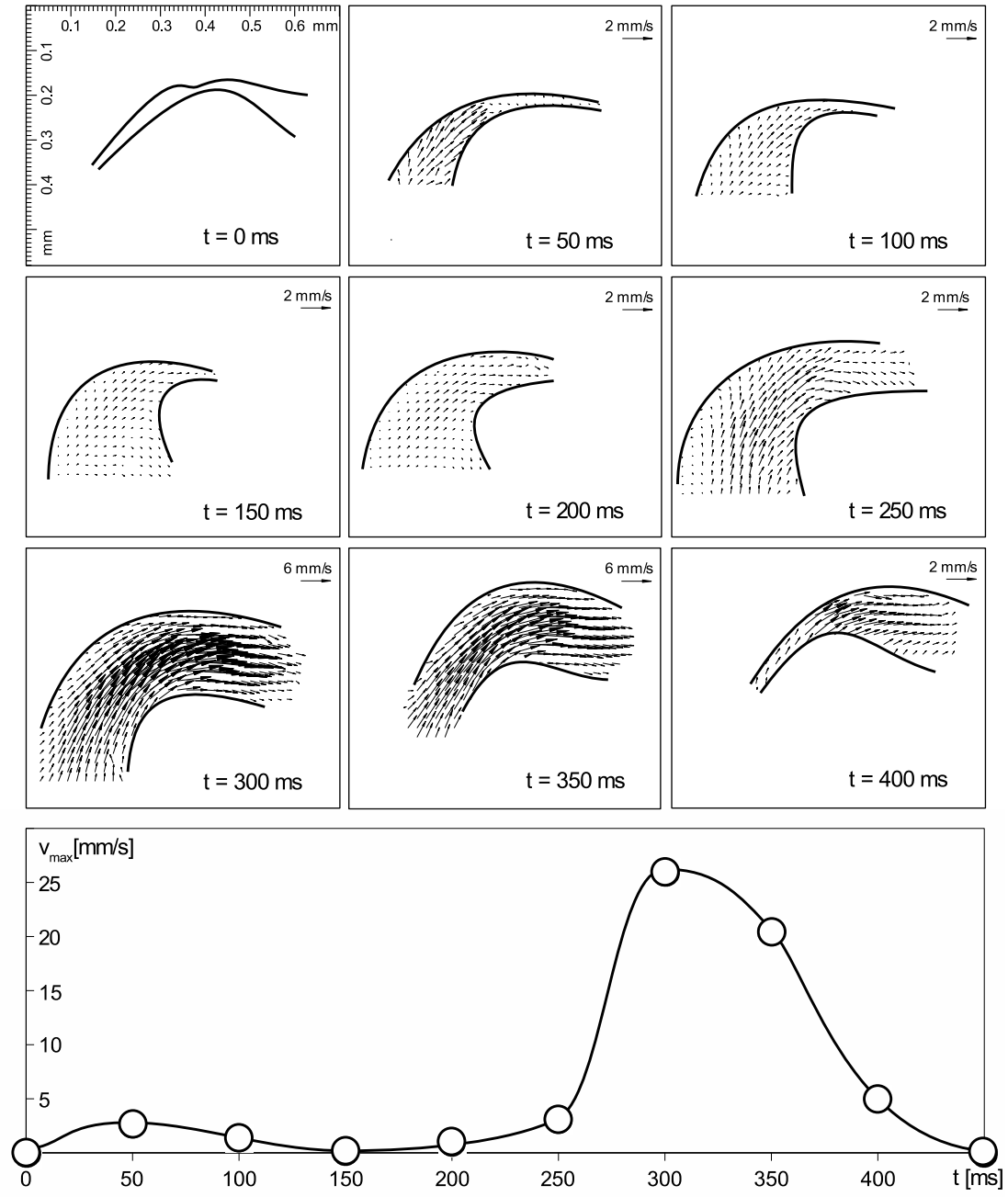

Figure 5.3: Velocity distribution in the developing ventricle at nine succeeding points of the cardiac cycle. The vector plot at $t = 300$ ms complies the left part of Figure 5.1. Note that the vector scale for $t = 300$ ms and $t = 350$ ms is reduced. The maximal velocity of each measurement is plotted over the time in the bottom part of the graph. The connecting curve serves to guide the eye.

Measurements in the developing atrium are found to be most successful in embryos that are lying on the side opposite the imaged atrium, with the head turned to the left, which naturally occurs in a small percentage of eggs. The right part of figure 5.1 shows an example of a velocity distribution in the expanding atrium. In contrast to the ventricle, the lumen boundary of the volume is more readily identified on the particle image of the atrium. This is explained by the smooth wall of the atrium, in contrast to the trabeculated myocardium of the ventricle. On the left side of the ventricle, just above the dashed line marking the inner ventricular wall, one can even see a group of particles trapped in the invaginations of the ventricle wall.

One of the goals of these measurements is to provide temporally and spatially resolved estimates of the velocity field. Under certain conditions these data can be used to access the local wall shear stress, τ (equation 1.1). The velocity gradient can be estimated by quadratically extrapolating the flow profile to zero (figure 5.1 continuous velocity profile). The relatively large interrogation windows of 64×64 pixel lead to an overestimate of the near-wall velocity when the interrogation region partially extends out of the flow region (figure 5.1 dashed velocity profile). Under such circumstances, the estimated velocity equals the average velocity of the particle-containing region of the window. This effect is accounted for by omitting the affected vectors during the interpolation of the velocity profile. Alternatively, this effect can be corrected by relocating each biased velocity vector to the area within the interrogation window that most contributed to the correlation result [99]. For the case shown in figure 5.1, this results in a maximum strain rate of $1.0 \cdot 10^3$ s^{-1} on the higher curvature wall. Here it should be pointed out that the strain rate can only be calculated for those regions where the main flow-direction is parallel to the image plane. The white, straight line in figure 5.1 indicates a section where the flow is perfectly aligned with the flow. Assuming an effective dynamic blood viscosity of 5 mPa·s leads to a maximum wall shear stress of 5 Pa. In comparison, the human vascular network experiences wall shear stress values up to approximately 7 Pa [111].

The assumption for the value of the dynamic blood viscosity represents a substantial contribution to the uncertainty of the shear stress estimate. Near the wall, a non-uniform distribution of erythrocytes accompanied by a spatial viscosity gradient must be expected, due to the Fåhraeus-Lindqvist effect. In the current estimate, a minimal value of the viscosity was assumed (corresponding to a magnitude slightly greater than that of clear plasma) in order to provide a conservative estimate of the wall shear stress. The non-Newtonian behavior of blood is less critical at shear rates that are relevant for the present study. In section 2.3 it is discussed that at a shear rate above $1.0 \cdot 10^2$ s^{-1} neither aggregation occurs, nor can the deformability of the erythrocytes further decrease the viscosity. Therefore, taking into consideration the high shear rates that were observed, the effective viscosity remains constant so that in this particular case the non-Newtonian behavior of blood can be ignored.

5.1.5 Discussion

The velocity has a maximum magnitude of 26 mm/s and peaks off-center at the side of the inner curvature wall. The eccentricity of the flow profile can be explained by the curvature of the heart. The micrograph in figure 5.1 shows that the heart resembles a curved tube. Dean [45] in 1927 introduced an analytical approximation for the fully developed, laminar velocity distribution in a coiled tube. The approximation is valid for low Dean numbers, Dn, defined as $Dn = \delta^{1/2}Re$. The curvature of the coil, δ (the ratio of coil and vessel radii, R/a), varies between about 1/2 and 1/4 for the case shown in figure 5.1. The Reynolds number, $Re = 2au/\nu$, with the mean velocity, u, and the kinematic viscosity, ν, is about unity. The left graph in figure 5.4 shows the axial velocity distribution along the vessel radius in the plane of coil curvature. The calculation [178] closely follows Deans analysis, higher order terms that were later added [44, 174] are omitted. The velocity is normalized by the mean velocity. As in the measurement, the location of the velocity maximum is shifted to the inner curvature wall. The second graph of figure 5.4 shows the radial position of the maximum velocity for different Reynolds numbers (curvature and vessel diameter remain at the current values). At higher Reynolds numbers (Re $>$ 20) inertia forces gain influence and the velocity peak shifts into the direction of the outer curvature wall. The right graph in figure 5.4 illustrates the influence of secondary flow. It shows the circumferential velocity component along the tube radius, perpendicular to the plane of coil curvature. The maximum circumferential velocity is lower than 1 % of the maximum velocity and can be neglected. It is therefore assumed that the velocity profile in figure 5.1 is oriented parallel to the optical plane of the camera. This qualifies the velocity profile for the determination of the local velocity gradient, du/dn, perpendicular to the wall. Under the assumption of an effective viscosity, η, the wall shear stress $\tau = \eta \cdot du/dn$ can finally be estimated as done in the previous section.

5.2 The Endothelin System in the Venous Clip Model

The measurements presented in this section are part of a publication in the Journal of Vascular Research [65]. The main goal of that article is to examine the mechanism between altered blood flow by venous clipping and cardiac maldevelopment. Especially the involvement of endothelin-1 (ET-1) in this process should be demonstrated.

5.2.1 The Venous Clip Model

The embryonic heart forms from an initially straight tube into a complex structure. This process is influenced by genetic and epigenic factors. Of interest to the functional aspects of gene expression are the physical determinants of gene expression regulation. One of the significant physical determinants in normal and abnormal human heart development is placental blood flow [74]. As already mentioned in section 1.2, a

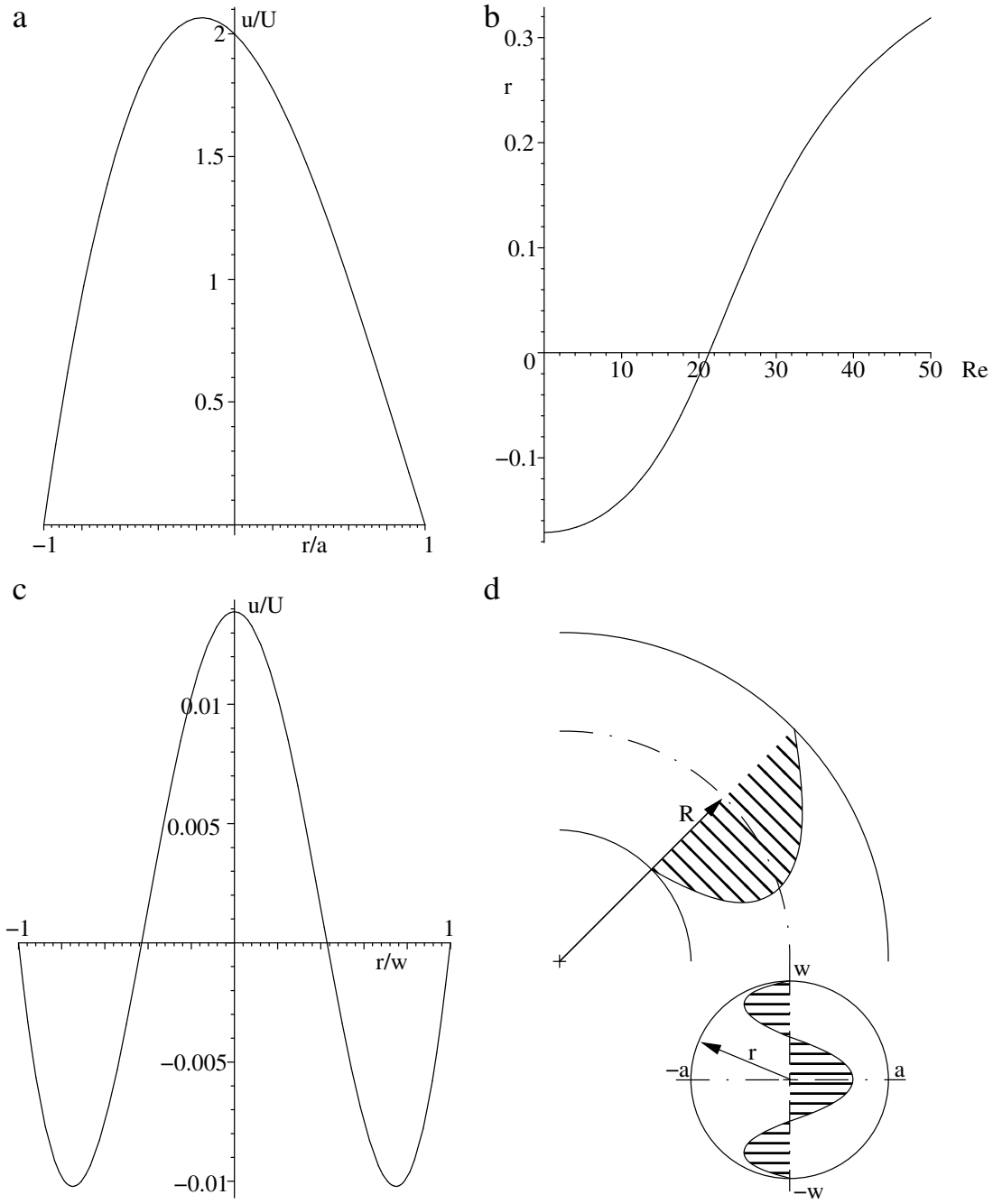

Figure 5.4: Theoretical flow profiles in an infinitely curved pipe (coil). The calculation closely follows Dean [45] and is explained in detail by Ward-Smith [178]. Deans solution is derived for small coil curvature, meaning that the tube radius a must be much smaller than the coil radius R. In the embryonic heart this condition is not strictly fulfilled ($R/a \approx 4$), still, Deans solution gives a good explanation for the experimental results. a: Axial velocity profile along the tube radius in the plane of coil curvature. b: Radial position for the velocity maximum in the plane of coil curvature at varying Reynolds numbers. c: secondary velocity profile in circumferential direction along the tube radius, perpendicular to the plane of coil curvature. (Please refer to figure part d for the nomenclature.)

chicken model is used for the experimental study of the relationship between gene expression and placental blood flow. Vitelline vessels serve the same function as the placenta in a mammalian embryo. It has been shown that obstructing flow, by closing one of these extraembryonic veins with a clip, results in re-routing of the venous return to the heart, the alteration of blood flow profiles through the heart, and the development of specific cardiovascular malformations [74].

Groenendijk et al. [64, 66] utilized the venous clip model to show that high levels of messenger ribonucleic acid (mRNA) for the Krüppel-like transcription factor (KLF-2) and endothelial nitric oxide synthase (NOS3) were localized in the outflow tract and in other narrow parts of the heart and vasculature. These genes have been shown to up-regulate expression under high shear stress conditions [47, 110]. In addition, these areas show low expression of endothelin-1, whose expression level has been shown to be negatively correlated with shear stress [64]. For example, knockout studies in mice show a crucial role of the strong vasoconstrictor ET-1 in cardiovascular development [185]. In vitro studies with cultured endothelial cells show a clear role for blood flow and shear stress on the regulation of ET-1 gene expression [166].

In combination with other studies [34, 91, 186] the hypothesis arises, that components of the so called ET-1 cascade might be involved in the development of malformations due to clipping. To test this hypothesis, ET-1 and three endothelin receptor antagonists (BQ-123, Bq-788, and PD145065)[1] were infused into the extraembryonic vasculature.

As a part of this study particle image velocimetry was used to measure the immediate effect of the injections on flow rate, vessel diameter, and heart rate. The conclusions in the original article [65] are also based on

- ultrasound measurements of heart rate and mean dorsal aortic velocity,
- the examination of the cardiovascular morphology at HH-stage 35 to study long term effects,
- the localization of ET_A and ET_B mRNA during the HH-stages 18 to 24 to analyze the capacity of embryonic heart tissue to respond to ET-1 and its antagonists, and
- additionally the determination of various endocardial gene expression quantities after ET-1 or ET-1 antagonist treatments in vitro.

In the scope of this thesis, only the particle image velocimetry measurements are discussed.

[1] Different endothelin receptor antagonists are used to differentiate between the two different endothelin receptors ET_A and ET_B. BQ-123 blocks the receptor ET_A, BQ-788 blocks the receptor ET_B, and PD145065 blocks both receptors.

5.2.2 Measurements

Micro particle image velocimetry measurements were performed at three time points per embryo: before infusion, 5 minutes after, and 30 minutes after infusion. At each time point, an optically accessible vein (40-100 μm), without interference of any underlying arteries, was analyzed. Each of the above mentioned four test substances was applied to three different embryos. Additionally the flow in a control (sham) embryo was measured. In total, 45 particle image velocimetry measurements were accomplished.

The tracer particles used in these experiments were the embryonic red blood cells. Here, the advantage of saving the time consuming injection of artificial tracers was important to promote a larger number of experiments. Secondly the impact on the embryo was minimized. These advantages, however, had to be paid with the disadvantages discussed in section 4.1.4. These are mainly a thick correlation volume, a non-uniform particle distribution, and low contrast images.

Each measurement of the current study is based on 500 sequential measurements at 10 Hz repetition rate. This corresponds to 50 seconds measurement duration. The individual evaluation of the measurements with coarse interrogation windows of 64×64 pixel was used to resolve the flow pulsation. The frequency analysis of this data resolves the heart rate. Afterwards the individual measurements were sorted according to their cardiac phase angle as described in section 4.3. The measurements were combined into groups of comparable flow conditions by separating the pulse into twelve segments of 50 ms length. Each group of individual measurements was evaluated by means of using correlation averages. Interrogation windows of 32×32 pixel (20×20 μm^2) were used. Figure 5.5 exemplarily shows one of the 45 time series. Note, that also little back-flow can be noticed during diastole.

5.2.3 Results and Discussion

The heart rate, the vessel diameter, the volume flow rate, and the mean wall shear stress in the vitelline veins are derived from the measured velocity data (figure 5.6). ET-1 infusion temporarily leads to an increased heart rate, and to a prolonged increase in volume flow rate. In contrast, both, BQ-123 and PD145065 infusions, lead to a prolonged decrease in heart rate. PD145065 also lead to a temporarily increased vessel diameter. In compliance with the decreased heart rate and the increased vessel diameter, the shear stress was significantly decreased 30 minutes after the PD145065 infusion. Blocking the ET_B receptor (BQ-788 infusion) does not show any significant effect at all.

A detailed interpretation can not be deduced solely from the particle image velocimetry measurements, but the results underline expected differences between the ET-1 mediated vasoregulation in the vitelline system and in the embryonic circulation that are related to the absence of ET_A receptors in the vitelline network. In [65] Groenendijk et al. postulate that ET-1-pathway-induced changes in hemodynamics in-

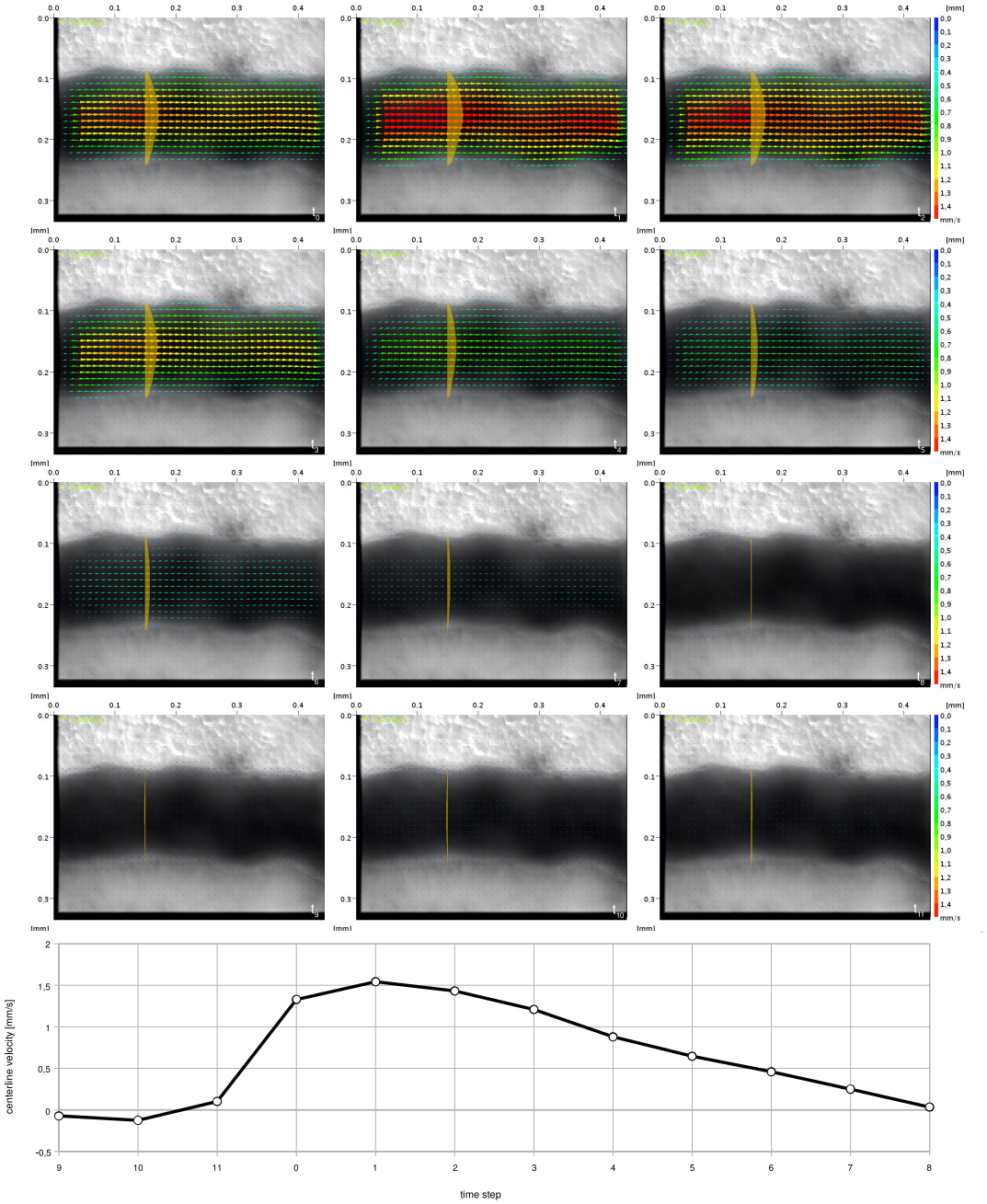

Figure 5.5: Typical velocity measurement using erythrocytes as tracer particles [65]. Little back-flow can be noticed during diastole.

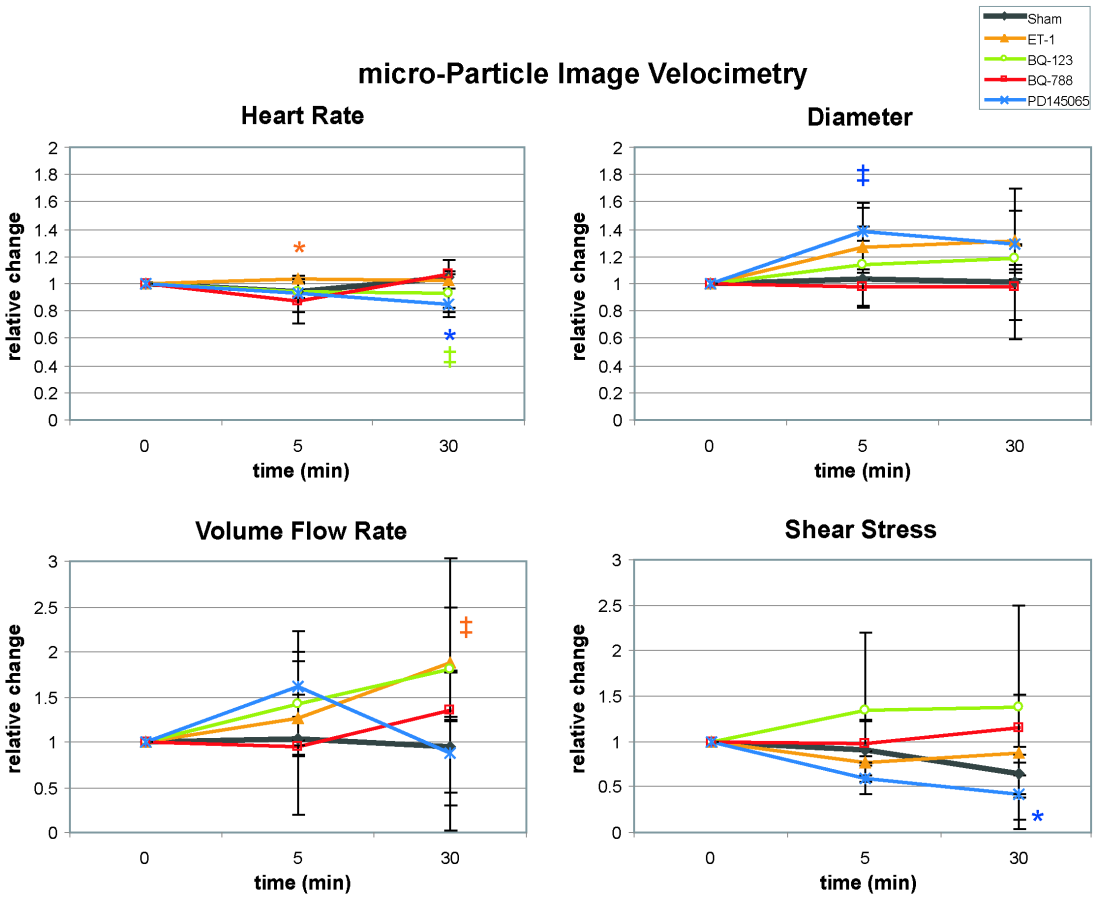

Figure 5.6: Changes in heart rate, vessel diameter, volume flow rate, and mean wall shear stress, derived from particle image velocimetry measurements. Each data point represents the median of three measurements in separate embryos. For comparability, all quantities are based on their initial value at time 0, so that the curves show the change of the median relative to the initial measurement. Statistically significant deviations are marked by *, trend-like deviations are marked by ‡, and bars represent the 25^{th} and 75^{th} percentiles (see [65] and the online supplement table 1 at `http://www.karger.com/doi/10.1159/000109077` for a detailed explanation of the statistical analysis).

fluence gene expression and flow patterns in the yolk sac resulting in changes in the intracardiac flow patterns. The authors further conclude that the balance-shift due to feedback mechanisms in receptor mRNA expression by ET-1 or receptor antagonists leads to impaired ventricular function and to morphological anomalies.

5.3 Assessment of three Dimensional Flow

5.3.1 Motivation

As shown in the previous sections, planar measurements are often sufficient to deliver the desired information, even though the real flow might be three dimensional. There are situations, however, where information about the remaining velocity component enables additional findings. Hogers et al. [74], for example, used ink to study the effect of various ligation positions of major embryonic chick vitelline veins on the flow pattern in the heart. The visualization of streaklines by means of ink heavily relies on the visual perception and the experience of the researcher. A computerized measurement and calculation of streamlines would provide quantitative results that are less dependent on the routine of the researcher. Also the direct comparison of measured shear stress with the visualization of three-dimensional gene expression patterns, like shown by Groenendijk et al. [64], or shear stress patterns derived by means of computational fluid dynamics (CFD) [66, 104], is much alleviated by representing the measurement data in a three-dimensional way.

5.3.2 Measurements

As a proof of principle, the methods compiled in section 4.7 are applied to the outflow section of the embryonic hart. The HH-stage 17+ embryo [68] was treated and accommodated as described in section 4.1. The microscopes magnification was set to 18×, corresponding to a resolution of 0.72 μm per image pixel[2]. In this way, the outflow tract of the heart just fits the cameras field of view of 493×373 μm^2. To save time for measurements at multiple planes (section 4.6), the untriggered measurement approach was chosen (section 4.3). PEGylated and fluorescent polystyrene tracer particles with a diameter of 1 μm were used as tracer particles.

The motorized stage of the microscope was utilized for stepping through 14 parallel measurement positions. Stepping down from the top of the heart and taking the first plane as a reference, the measurement positions were 0, -13, -25, -38, -51, -65, -76, -89, -102, -115, -127, -137, -151, and -162 μm. Due to the limited accuracy of the translation mechanism, the step size is slightly variable. Each measurement consists of 500 image pairs, taken at a frequency of 10 Hz with an interframing time of 0.5 ms. Thus, measuring one plane takes 50 seconds, and the whole measurement 12

[2]Four camera pixel were combined to one image pixel (2×2 hardware binning) to enhance light sensitivity and recording speed.

minutes. A velocity of 25.8 mm/s corresponds to a displacement of 18 pixel units. Rather large displacements are accepted in general to gain accuracy close to the wall, where velocities are small.

5.3.3 Results and Discussion

The evaluation procedure follows the description in section 4.3 (data sorting) and section 4.4 (ensemble evaluation). The sorted, quasi time resolved image data, is divided into twenty four groups (time periods). A finer temporal resolution is disadvantageous because a minimum of about 20 image pairs should be conserved for ensemble correlation. A minor dithering of the images relative to each other appears due to a slight movement of the embryo during the measurement. The dithering is compensated by shifting the images relative to the first image prior to the ensemble correlation. The shift vector is based on a correlation between the whole area of each image and the first image of an ensemble. To avoid velocity bias errors due to background intensity gradients, a background subtraction (ensemble minimum) is applied. The particle image evaluation consists of three iterative passes [117]. First, a coarse displacement field is calculated using 64×64 pixel non overlapping interrogation windows. After intensive outlier detection and smoothing, the result is interpolated on a grid with 16 pixel spacing. The last two passes use 32×32 pixel interrogation windows overlapping 50 % that are pre-shifted[3] according to the vector map of the preceding pass, respectively. The output of the last pass is solely subject to an outlier detection based on a normalized median filtering method [183]. The third velocity component was reconstructed as described in section 4.7[4].

Figure 5.7 exemplarily shows a three dimensional representation of the first out of twenty four time periods (peak systolic flow). Five arbitrary cuts through the data show the evolvement of the velocities in flow direction. A number of streamlines indicate the curvature of the flow. As already discussed in section 5.1.5, again the position of the peak velocity is found to be shifted from the center of the heart to the inner curvature wall (compare distance O and I).

The technique of this first assessment of accurate, three dimensional velocity information in the embryonic chicken heart forms the basis of ongoing research on the relation of fluid mechanics and biomedical phenomena. Local wall shear rates have been determined in the vitelline network of a chicken embryo [128, 129], as well as in the embryonic chicken heart [130]. Figure 5.8 exemplarily shows a color coded plot of the wall shear rate in a section of the outflow tract of the embryonic heart [130]. In a next step, the results from control embryos and embryos with an extraembryonic venous clip will be compared to histology experiments that give information about local gene expression.

[3] Central differences are used.

[4] See footnote 1 on page 5 for details about the software used for image evaluation, filtering, and third component reconstruction.

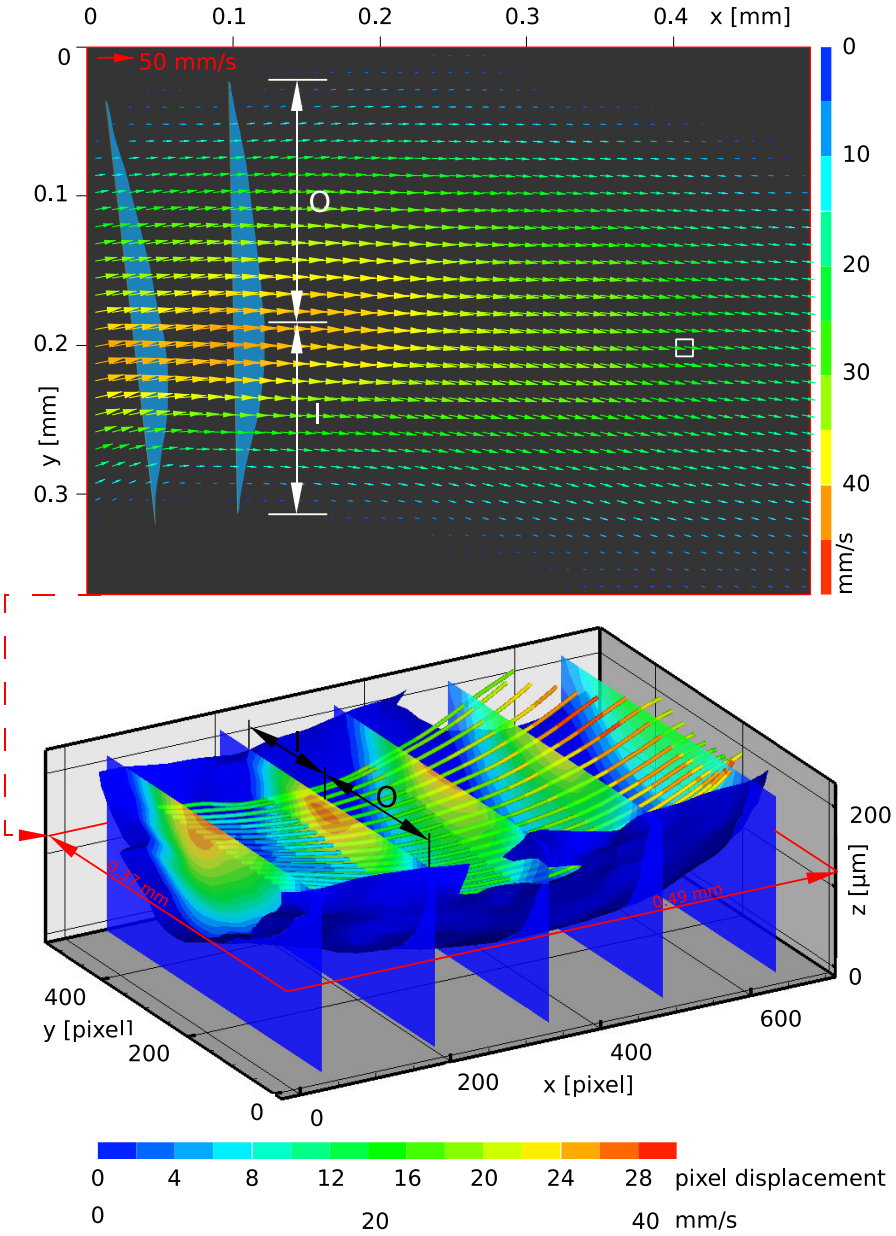

Figure 5.7: Example for the reconstructed, three dimensional flow distribution in the outflow tract of the embryonic heart at peak systolic flow (first time step out of twenty four). The vector field in the top part of the figure exemplarily shows the planar result of the eleventh plane from top (-127 μm). The position of this measurement plane in the three dimensional representation (bottom) is indicated by a red frame. Corresponding corners are connected by the red, dashed line. Note that the three dimensional reconstruction is turned bottom up. The flow boundary is represented by iso-contours just above noise level. The spatial resolution of the measurement (size of interrogation windows) is 32 pixel, corresponding to 23 μm. The color coding of the stream lines indicate the velocity component in z-direction (negative: blue, positive: red, not corresponding to the color bar). The correlation function corresponding to the vector marked by a white square is exemplarily plotted in figure 4.9.

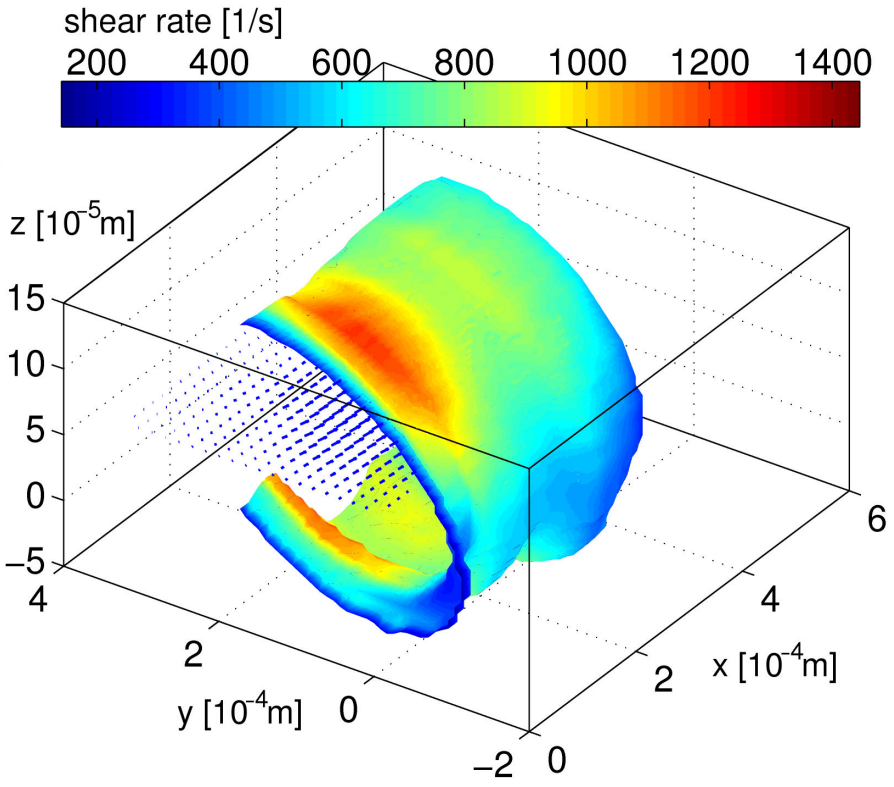

Figure 5.8: A segment of the outflow tract of the embryonic heart. The wall shear rate is color coded on the surface. Measurements were taken parallel to the x,z-plane [130].

Appendix A

Ethical Considerations

Using living organisms for experimental studies involves reflections on right or wrong action in a legal as well as in a moral sense. An answer on the legal dimension of this question is given in the applicable regulation of the European Union, the "council directive 86/609/EEC on the approximation of laws, regulations and administrative provisions of the Member States regarding the protection of animals used for experimental and other scientific purposes". In the second article is defined "'animal' unless otherwise qualified, means any live non-human vertebrate, including free-living larval and/or reproducing larval forms, but excluding foetal or embryonic forms;". According to law an embryo is thus not an animal and therefore not protected.

Conscience and religion are instances that might be consulted for answering the moral dimension of the question. A closer consideration of religion, however, must be left out in this thesis, because of the complexity and fuzziness of the debate [138]. Indication for finding an answer comes from Gruber and Hartung [67], Doerenkamp-Zbinden prize laureates for experimental animal free research in 2004 and 1996, respectively. They recommend the incubated chicken egg as an alternative to animal experiments, as long as the embryo is insensitive to pain. Rosenbruch [142] finds the onset of sensitivity to pain soonest at day eight of incubation. In the scope of this thesis eggs were usually incubated three days, at maximum five days.

Nevertheless, watching a chicken embryo through a microscope, recognizing the eye, the brain, the backbone, the circulating blood cells, and the ambitiously beating heart, increased my respect for the developing life.

Bibliography

[1] R J Adrian.
Particle-imaging techniques for experimental fluid mechanics.
Annual Review of Fluid Mechanics, 23:261–304, 1991.

[2] Y Aizu and T Asakura.
Coherent opticel techniques for diagnostics of retinal blood flow.
Journal of Biomedical Optics, 4(1):61–75, 1999.

[3] K H Albrecht, P Gaehtgens, A Pries, and M Heuser.
The Fahraeus effect in narrow capillaries (i.d. 3.3 to 11.0 micron).
Microvascular Research, 18(1):33–47, 1979.

[4] T M Allen.
Liposomal drug delivery.
Current Opinion in Colloid & Interface Science, 1:645–651, 1996.

[5] M P Arroyo and C A Greated.
Stereoscopic particle image velocimetry.
Measurement Science and Technology, 2:1181–1186, 1991.

[6] M Baker and H Wayland.
On-line volume flow rate and velocity profile measurement for blood in microvessels.
Microvascular Research, 7(1):131–143, 1974.

[7] J H Barbee and G R Cokelet.
The Fahraeus effect.
Microvascular Research, 3(1):6–16, 1971.

[8] O K Baskurt, R A Farley, and H J Meiselman.
Erythrocyte aggregation tendency and cellular properties in horse, human, and rat: a comparative study.
American Journal of Physiology, 273(6 Pt 2):H2604–H2612, 1997.

[9] A Basler.
Über die Blutbewegung in den Kapillaren.
Pflugers Arch, 171(1):134–145, 1918.

[10] W R Bauer, K H Hiller, P Galuppo, S Neubauer, J Köpke, A Haase, C Waller, and G Ertl.
Fast high-resolution magnetic resonance imaging demonstrates fractality of myocardial perfusion in microscopic dimensions.
Circulation Research, 88(3):340–346, 2001.

[11] D H Bergel and W R Milnor.
Pulmonary vascular impedance in a dog.
Circulation Research, 16:401–415, 1965.

[12] J J Bishop, P R Nance, A S Popel, M Intaglietta, and P C Johnson.
Effect of erythrocyte aggregation on velocity profiles in venules.
American Journal of Physiology - Heart and Circulatory Physiology, 280(1): H222–H236, 2001.

[13] J J Bishop, A S Popel, M Intaglietta, and P C Johnson.
Effects of erythrocyte aggregation and venous network geometry on red blood cell axial migration.
American Journal of Physiology - Heart and Circulatory Physiology, 281(2): H939–H950, 2001.

[14] J L Boulnois.
Photophysical processes in recent medical laser developments: a review.
Lasers in Medical Science, 1:45–66, 1986.

[15] C J Bourdon, M G Olsen, and A D Gorby.
Validation of an analytical solution for depth of correlation in microscopic particle image velocimetry.
Measurement Science and Technology, 15:318–327, 2004.

[16] C J Bourdon, M G Olsen, and A D Gorby.
Power-filter technique for modifying depth of correlation in microPIV experiments.
Experiments in Fluids, 37:263–271, 2004.

[17] W G Bradley and V Waluch.
Blood flow: magnetic resonance imaging.
Radiology, 154(2):443–450, 1985.

[18] P J Brands, A P Hoeks, L Hofstra, and R S Reneman.
A noninvasive method to estimate wall shear rate using ultrasound.
Ultrasound in Medicine & Biology, 21(2):171–185, 1995.

[19] P J Brands, A P Hoeks, J Willigers, C Willekes, and R S Reneman.
An integrated system for the non-invasive assessment of vessel wall and hemodynamic properties of large arteries by means of ultrasound.
European Journal of Ultrasound, 9(3):257–266, 1999.

[20] J D Briers.
Laser Doppler and time-varying speckle: a reconciliation.
Journal of the Optical Society of America A, 13(2):345–350, 1996.

[21] J D Briers.
Laser Doppler, speckle and related techniques for blood perfusion mapping and imaging.
Physiological Measurement, 22(4):R35–66, 2001.

[22] J D Briers, G Richards, and X W He.
Capillary blood flow monitoring using laser speckle contrast analysis.
Journal of Biomedical Optics, 4(1):164–175, 1999.

[23] Ch. Brücker.
Digital-Particle-Image-Velocimetry (DPIV) in a scanning light-sheet: 3D starting flow around a short cylinder.
Experiments in Fluids, 19:255–263, 1995.

[24] G Bugliarello.
Biofluidmechanics: quo vadimus?
Annals of Biomedical Engineering, 5(3):209–247, 1977.

[25] L Büttner and J Czarske.
Spatial resolving laser doppler velocity profile sensor using slightly tilted fringe systems and phase evaluation.
Measurement Science and Technology, 14:2111–2120, 2003.

[26] L Büttner and Jürgen Czarske.
Determination of the axial velocity component by a laser-doppler velocity profile sensor.
Journal of the Optical Society of America A, 23(2):444–454, 2006.

[27] L Büttner, J Czarske, and H Knuppertz.
Laser-Doppler velocity profile sensor with submicrometer spatial resolution that employs fiber optics and a diffractive lens.
Applied Optics, 44(12):2274–2280, 2005.

[28] V Cerný, Z Turek, and R Parízková.
Orthogonal polarization spectral imaging.
Physiological Research, 56:141–147, 2007.

[29] S E Charm and G S Kurland.
On the significance of the Reynolds Number in blood flow.
Biorheology, 3(3):163–164, 1966.

[30] S E Charm and G S Kurland.
Static method for determining blood yield stress.
Nature, 216(120):1121–1123, 1967.

[31] S E Charm and G S Kurland.
Blood Flow and Microcirculation.
Wiley, 1974.

[32] S E Charm, G S Kurland, and S L Brown.
The influence of radial distribution and marginal plasma layer on the flow of red cell suspensions.
Biorheology, 5(1):15–43, 1968.

[33] S Chien.
Shear dependence of effective cell volume as a determinant of blood viscosity.
Science, 168:977–979, 1970.

[34] D E Clouthier, K Hosoda, J A Richardson, S C Williams, H Yanagisawa, T Kuwaki, M Kumada, R E Hammer, and M Yanagisawa.
Cranial and cardiac neural crest defects in endothelin-a receptor-deficient mice.
Development, 125(5):813–824, 1998.

[35] WT Clusin.
Correlation between relaxation and automaticity in embryonic heart cell aggregates.
Proceedings of the National Academy of Sciences of the USA, 77(1):679–683, 1980.

[36] G R Cokelet, A R Pries, and M F Kiani.
Observations on the accuracy of photometric techniques used to measure some in vivo microvascular blood flow parameters.
Microcirculation, 5(1):61–70, 1998.

[37] A L Copley.
Fluid mechanics and biorheology.
Biorheology, 27(1):3–19, 1990.

[38] A L Copley and G W Scott Blair.
Hemorheology. An introduction.
Bibliotheca Haematologica, 13:6–23, 1962.

[39] A L Copley, L C Krchma, and M E Whitney.
Humoral rheology.
Journal of General Physiology, 26:49–64, 1942.

[40] A Cuocolo, W Acampa, M Imbriaco, N De Luca, G L Iovino, and M Salvatore.
The many ways to myocardial perfusion imaging.
Quarterly Journal of Nuclear Medicine and Molecular Imaging, 49(1):4–18, 2005.

[41] J Czarske.
Laser Doppler velocity profile sensor using a chromatic coding.
Measurement Science and Technology, 12:52–57, 2001.

[42] J Czarske, L Büttner an T Razik, and H Müller.
Boundary layer velocity measurements by a laser doppler profile sensor with micrometre spatial resolution.
Meas Sci Techol, 13:1979–1989, 2002.

[43] G. Danuser.
Coupling the dynamics of two actin networks-new views on the mechanics of cell protrusion.
Biochemical Society Transactions, 33(Pt 6):1250–1253, 2005.

[44] W R Dean.
The stream-line motion of fluid in a curved pipe.
Philosophical Magazine, 5(30):673–695, 1928.

[45] W R Dean.
Note on the motion of a fluid in a curved pipe.
Philosophical Magazine, 4(20):208–223, 1927.

[46] P Debaene, U Kertzscher, L Goubergrits, and K Affeld.
Visualization of wall shear flow.
Journal of Visualization, 8(4):305–313, 2005.

[47] R J Dekker, S van Soest, R D Fontijn, S Salamanca, P G de Groot, E Van Bavel, H Pannekoek, and A J G Horrevoets.
Prolonged fluid shear stress induces a distinct set of endothelial cell genes, most specifically lung Krüppel-like factor (KLF2).
Blood, 100(5):1689–1698, 2002.

[48] A du Pré Denning and J H Watson.
The viscosity of blood.
Proceedings of the Royal Society of London, Series B, 78:328–358, 1906.

[49] A K Dunn, A Devor, H Bolay, M L Andermann, M A Moskowitz, A M Dale, and David A Boas.
Simultaneous imaging of total cerebral hemoglobin concentration, oxygenation, and blood flow during functional activation.
Optics Letters, 28(1):28–30, 2003.

[50] F Durst and WH Stevenson.
Influence of gaussian beam properties on laser doppler signals.
Applied Optics, 18:516, 1979.

[51] G E Elsinga, F Scarano, B Wieneke, and B W van Oudheusden.
Tomographic particle image velocimetry.
Experiments in Fluids, 41:933–947, 2006.

[52] T J Essex and P O Byrne.
A laser Doppler scanner for imaging blood flow in skin.
Journal of Biomedical Engineering, 13(3):189–194, 1991.

[53] C A Ewald.
Über die Transpiration des Blutes.
Archiv für Anatomie und Physiologie, pages 208–249, 1877.

[54] J Feng and S Weinbaum.
Lubrication theory in highly compressible porous media: the mechanics of skiing, from red cells to humans.
Journal of Fluid Mechanics, 422:281–317, 2000.

[55] A F Fercher and J D Briers.
Flow visualization by means of single-exposure speckle photography.
Optics Communications, 37(5):326–330, 1981.

[56] K W Ferrara, B G Zagar, and J B Sokil-Melgar.
Estimation of blood velocity with high frequency ultrasound.
IEEE Transactions on Ultrasonics, Ferroelectrics, and Frequency Control, 43: 149–157, 1996.

[57] A Frydrychowicz, E Weigang, A Harloff, F Beyersdorf, J Hennig, M Langer, and M Markl.
Images in cardiovascular medicine. Time-resolved 3-dimensional magnetic resonance velocity mapping at 3 T reveals drastic changes in flow patterns in a partially thrombosed aortic arch.
Circulation, 113(11):e460–e461, 2006.

[58] A Frydrychowicz, E Weigang, M Langer, and M Markl.
Flow-sensitive 3d magnetic resonance imaging reveals complex blood flow alterations in aortic dacron graft repair.
Interactive Cardiovascular and Thoracic Surgery., 5:340–342, 2006.

[59] A Frydrychowicz, A Harloff, B Jung, M Zaitsev, E Weigang, T A Bley, M Langer, J Henning, and M Markl.
Time-resolved 3D MR flow analysis at 3T: Visualization of normal and pthological aortic vascular hemodynamics.
Journal of Computer Assisted Tomography, 31(1):9–15, 2007.

[60] P Gaehtgens, H Wayland, and H J Meiselman.
Velocity profile measurements in living microvessels by a correlation method.
In H Hartert and A L Copley, editors, *Theoretical and clinical hemorheology*, pages 381–384, University of Heidelberg, West Germany, 1971. The International Society of Hemorheology, Springer.

[61] P Gaehtgens, F Schmidt, and G Will.
Comparative rheology of nucleated and non-nucleated red blood cells I. microrheology of avian erythrocytes during capillary flow.
Pflügers Archiv - European Journal of Physiology, 390(3):278–282, 1981.

[62] R W Gill.
Measurement of blood flow by ultrasound: accuracy and sources of error.
Ultrasound in Medicine & Biology, 11(4):625–41, 1985.

[63] J W Goodman.
Statistical Optics.
Wiley Classics Library. John Wiley & Sons, 2000.

[64] B C Groenendijk, B P Hierck, A C Gittenberger-de Groot, and R E Poelmann.
Development-related changes in the expression of shear stress responsive genes KLF-2, ET-1, and NOS-3 in the developing cardiovascular system of chicken embryos.
Developmental Dynamics, 230(1):57–68, 2004.

[65] B C W Groenendijk, S Stekelenburg-de Vos, P Vennemann, J W Wladimiroff, F T M Nieuwstadt, R Lindken, J Westerweel, B P Hierck, N T C Ursem, and R E Poelmann.
The endothelin-1 pathway and the development of cardiovascular defects in the hemodynamically challenged chicken embryo.
Journal of Vascular Research, 45:54–68, 2008.

[66] Bianca C W Groenendijk, Beerend P Hierck, Johannes Vrolijk, Martin Baiker, Mathieu J B M Pourquie, Adriana C Gittenberger de Groot, and Robert E Poelmann.
Changes in shear stress-related gene expression after experimentally altered venous return in the chicken embryo.
Circulation Research, 96(12):1291–1298, 2005.

[67] F P Gruber and T Hartung.
Alternatives to animal experimentation in basic research.
ALTEX, 21 Suppl 1:3–31, 2004.

[68] V Hamburger and H L Hamilton.
A series of normal stages in the development of the chick embryo.
Journal of Morphology, 88:49–92, 1951.

[69] M A Haque, W Watanabe, H Ono, Y Sakamoto, and H Tazawa.
Comparisons between invasive and noninvasive determinations of embryonic heart rate in chickens.
Comparative biochemistry and physiology Comparative physiology, 108(2-3): 221–227, 1994.

[70] J Harkness.
The viscosity of human blood plasma; its measurement in health and disease.
Biorheology, 8(3):171–193, 1971.

[71] Eugene Hecht.
Optics.
Addison Wesley, 4 edition, 2002.

[72] D L Hitt, M L Lowe, J R Tincher, and J M Watters.
A new method for blood velocimetry in the microcirculation.
Microcirculation, 3(3):259–262, 1996.

[73] A P Hoeks, R S Reneman, and P A Peronneau.
A multigate pulsed doppler system with serial data processing.
IEEE Transactions on Sonics and Ultrasonics, SU-28(4):242–247, 1981.

[74] B Hogers, M C DeRuiter, A C Gittenberger-de Groot, and R E Poelmann.
Extraembryonic venous obstructions lead to cardiovascular malformations and can be embryolethal.
Cardiovascular Research, 41:87–99, 1999.

[75] B K P Horn and B G Schunck.
Determining optical flow.
Artificial Intelligence, 17:185–203, 1981.

[76] J R Hove.
In vivo biofluid dynamic imaging in the developing zebrafish.
Birth Defects Research Part C: Embryo Today, 72(3):277–289, 2004.

[77] J R Hove, R W Köster, A S Forouhar, G Acevedo-Bolton, S E Fraser, and M Gharib.
Intracardiac fluid forces are an essential epigenetic factor for embryonic cardiogenesis.
Nature, 421:172–177, 2003.

[78] K Hu, Lin Ji, K T Applegate, G Danuser, and C M Waterman-Storer.
Differential transmission of actin motion within focal adhesions.
Science, 315:111–115, 2007.

[79] T C Hung, T K Hung, and G Bugliarello.
Blood flow in straight and curved capillary glass tubes.
Journal of Biomechanics, 12(12):945–947, 1979.

[80] T C Hung, T K Hung, and G Bugliarello.
Blood flow in capillary tubes: curvature and gravity effects.
Biorheology, 17:331–342, 1980.

[81] H S Ji, J Y Lee, and S J Lee.
In-vitro study on the hemorheological characteristics of chicken blood in microcirculation.
Korea-Australia Rheology Journal, 19(2):89–95, 2007.

[82] L Ji and G Danuser.
Tracking quasi-stationary flow of weak fluorescent signals by adaptive multi-frame correlation.
Journal of Microscopy, 220(Pt 3):150–167, 2005.

[83] R D Keane and R J Adrian.
Optimization of particle image velocimeters. Part I: Double pulsed systems.
Measurement Science and Technology, 1:1202–1215, 1990.

[84] R D Keane and R J Adrian.
Optimization of particle image velocimeters. Part II: Multiple pulsed systems.
Measurement Science and Technology, 2:963–974, 1991.

[85] R D Keane and R J Adrian.
Theory of cross-correlation analysis of PIV images.
Applied Scientific Research, 49:191–215, 1992.

[86] R D Keane, R J Adrian, and Y Zhang.
Super-resolution particle imaging velocimetry.
Measurement Science and Technology, 6:754–768, 1995.

[87] H B Kim, J Hertzberg, C Lanning, and R Shandas.
Noninvasive measurement of steady and pulsating velocity profiles and shear rates in arteries using echo PIV: in vitro validation studies.
Annals of Biomedical Engineering, 32(8):1067–1076, 2004.

[88] H B Kim, J R Hertzberg, and R Shandas.
Development and validation of echo PIV.
Experiments in Fluids, 36:455–462, 2004.

[89] M Kleiber.
Body size and metabolism.
Hilgardia, 6:315–353, 1932.

[90] R Krams, G Bambi, F Guidi, F Helderman, A F W van der Steen, and P Tortoli.
Effect of vessel curvature on doppler derived velocity profiles and fluid flow.
Ultrasound in Medicine & Biology, 31(5):663–671, 2005.

[91] Y Kurihara, H Kurihara, H Oda, K Maemura, R Nagai, T Ishikawa, and Y Yazaki.
Aortic arch malformations and ventricular septal defect in mice deficient in endothelin-1.
The Journal of Clinical Investigation, 96(1):293–300, 1995.

[92] J Y Lee, H S Ji, and S J Lee.
Micro-PIV measurements of blood flow in extraembryonic blood vessels of chicken embryos.
Physiological Measurement, 28:1149–1162, 2007.

[93] HJ Levine.
Rest heart rate and life expectancy.
Journal of the American College of Cardiology, 30(4):1104–1106, 1997.

[94] B Lewy.
Die reibung des blutes.
Pflügers Archiv - European Journal of Physiology, 65:447–472, 1897.

[95] K Ley.
Molecular mechanisms of leucocyte rolling and adhesion to microvascular endothelium.
European Heart Journal, 14 Suppl I:68–73, 1993.

[96] D Liepsch.
An introduction to biofluid mechanics - basic models and applications.
Journal of Biomechanics, 35(4):415–435, 2002.

[97] D W Liepsch.
Flow in tubes and arteries - a comparison.
Biorheology, 23:395–433, 1986.

[98] B A Lin, S Einav, M M Zarandi, and M Gharib.
Digital ultrasound speckle image velocimetry for quantitative cardiovascular flow visualization.
In *5th International Symposium on Particle Image Velocimetry*, page Paper 3152, Busan, Korea, 2003.

[99] R Lindken, C Poelma, and J Westerweel.
Compensation for spatial effects for non-uniform seeding in PIV interrogation by signal relocation.
In *Proceedings of the 5th International Symposium on Particle Image Velocimetry*, Busan, Korea, 2003.

[100] R Lindken, J Westerweel, and B Wieneke.
Stereoscopic micro particle image velocimetry.
Experiments in Fluids, 41:161–171, 2006.

[101] R Lindken, J Westerweel, and B Wieneke.
3D micro-scale velocity methods: A comparison between 3D-μPTV, stereoscopic μPIV and tomographic μPIV.
In *13th Int. Symp. on Applications of Laser Techniques to Fluid Mechanics*, Lisbon, Portugal, 2006.

[102] H H Lipowsky.
Microvascular rheology and hemodynamics.
Microcirculation, 12(1):5–15, 2005.

[103] H H Lipowsky, S Usami, and S Chien.
In vivo measurements of "apparent viscosity" and microvessel hematocrit in the mesentery of the cat.
Microvascular Research, 19(3):297–319, 1980.

[104] A Liu, S Rugonyi, J O Pentecost, and K L Thornburg.
Finite element modeling of blood flow-induced mechanical forces in the outflow tract of chick embryonic hearts.
Computers and Structures, 85:727–738, 2007.

[105] M A Lodge, H Braess, F Mahmoud, J Suh, N Englar, S Geyser-Stoops, J Jenkins, S L Bacharach, and V Dilsizian.
Developments in nuclear cardiology: transition from single photon emission computed tomography to positron emission tomography-computed tomography.
The Journal of Invasive Cardiology, 17(9):491–496, 2005.

[106] D S Long, M L Smith, A R Pries, K Ley, and E R Damiano.
Microviscometry reveals reduced blood viscosity and altered shear rate and shear stress profiles in microvessels after hemodilution.
Proceedings of the National Academy of Sciences of the USA, 101(27):10060–10065, 2004.

[107] B Lucas and T Kanade.
An iterative image registration technique with an application to stereo vision.
In *International Conference on Artificial Intelligence*, pages 674–679, 1981.

[108] H G Maas, A Gruen, and D Papantoniou.
Particle tracking velocimetry in three-dimensional flows.
Experiments in Fluids, 15:133–146, 1993.

[109] D Magde, G E Rojas, and P G Seybold.
Solvent dependence of the fluorescence lifetimes of xanthene dyes.
Photochemistry and Photobiology, 70(5):737–744, 1999.

[110] A M Malek and S Izumo.
Control of endothelial cell gene expression by flow.
Journal of Biomechanics, 28:1515–1528, 1995.

[111] A M Malek, S L Alper, and S Izumo.
Hemodynamic shear stress and its role in atherosclerosis.
Journal of the American Medical Association, 282:2035–2042, 1999.

[112] J Männer.
Cardiac looping in the chick embryo: a morphological review with special reference to terminological and biomechanical aspects of the looping process.
The Anatomical Record, 259:248–262, 2000.

[113] M Markl, F P Chan, M T Alley, K L Wedding, M T Draney, C J Elkins, D W Parker, R Wicker, C A Taylor, R J Herfkens, and N J Pelc.
Time-resolved three-dimensional phase-contrast MRI.
Journal of Magnetic Resonance Imaging, 17(4):499–506, 2003.

[114] T McMahon and JT Bonner.
On Size and Life.
Scientific American Library, 1983.

[115] C D Meinhart, S T Wereley, and J G Santiago.
PIV measurements of a microchannel flow.
Experiments in Fluids, 27:414–419, 1999.

[116] C D Meinhart, S T Wereley, and M H B Gray.
Volume illumination for two-dimensional particle image velocimetry.
Measurement Science and Technology, 11:809–814, 2000.

[117] C D Meinhart, S T Wereley, and J G Santiago.
A PIV algorithm for estimating time-averaged velocity fields.
Journal of Fluids Engineering, 122:285–289, 2000.

[118] W Merzkirch.
Flow Visualization.
Academic Press, 1987.

[119] G Michelson, M Groh, M Langhans, and B Schmauss.
2-dimensional mapping and retinal and papillary microcirculation using scanning laser Doppler flowmetry (german language article).
Klinisches Monatsblatt der Augenheilkunde, 207(3):180–190, 1995.

[120] W R Milnor.
Hemodynamics.
Williams & Wilkins, 1989.

[121] P A G Monro.
Visual particle velocity measurements in fluid streams.
In A Copley, editor, *Symposium on Biorheology*, pages 439–449, 1965.

[122] C D Murray.
The physiological principle of minimum work: I. the vascular system and the cost of blood volume.
Proceedings of the National Academy of Sciences of the USA, 12(3):207–214, 1926.

[123] C J Murray and A D Lopez.
Mortality by cause for eight regions of the world: Global burden of disease study.
Lancet, 349(9061):1269–1276, 1997.

[124] R Nezafat, P Kellman, J A Derbyshire, and E R McVeigh.
Real-time blood flow imaging using autocalibrated spiral sensitivity encoding.
Magnetic Resonance in Medicine, 54(6):1557–1561, 2005.

[125] M G Olsen and R J Adrian.
Out-of-focus effects on particle image visibility and correlation in microscopic particle image velocimetry.
Experiments in Fluids, 29(7):166–174, 2000.
Suppl.

[126] T A Ooms, W D Koek, J J M Braat, and J Westerweel.
Optimizing fourier filtering for digital holographic particle image velocimetry.
Measurement Science and Technology, 17:304–312, 2006.

[127] S A Pape, C A Skouras, and P O Byrne.
An audit of the use of laser Doppler imaging (LDI) in the assessment of burns of intermediate depth.
Burns, 27(3):233–239, 2001.

[128] C Poelma, P Vennemann, R Lindken, and J Westerweel.
In vivo blood flow velocity measurement in the vitelline network.
In *7th International Symposium on Particle Image Velocimetry*, Rome, 2007.

[129] C Poelma, P Vennemann, R Lindken, and J Westerweel.
In vivo blood flow and wall shear stress measurements in the vitelline network.
Experiments in Fluids, online first, 2008.
doi: 10.1007/s00348-008-0476-6.

[130] C Poelma, P Vennemann, K van der Heiden, R Lindken, B Hierck, and J Westerweel.
Wall shear stress measurements using μpiv in the outflow tract of a chick embryo.
In *14th International Symposium on Applications of Laser Techniques to Fluid Mechanics*, Lisbon, 2008.

[131] J L Poiseuille.
Recherches expérimentales sur le mouvement des liquides dans les tubes de très-petits diamètres.
Comptes Rendus, Académie des Sciences, Paris, 12:112, 1841.

[132] J M Poiseuille.
Recherches expérimentales sur le mouvement des liquides dans les tubes de très-petits diamètres.
Imprimerie Royale, Paris, 1846.

[133] A S Popel and P C Johnson.
Microcirculation and hemorheology.
Annual Review of Fluid Mechanics, 37:43–69, 2005.

[134] A J Powell and T Geva.
Blood flow measurement by magnetic resonance imaging in congenital heart disease.
Pediatric Cardiology, 21:47–58, 2000.

[135] A K Prasad.
Stereoscopic particle image velocimetry.
Experiments in Fluids, 29:103–116, 2000.

[136] A R Pries, D Neuhaus, and P Gaehtgens.
Blood viscosity in tube flow: dependence on diameter and hematocrit.
American Journal of Physiology, 263(6 Pt 2):H1770–H1178, 1992.

[137] M Raffel, C Willert, and J Kompenhans.
Particle image velocimetry: A practical guide.
Springer, 1998.

[138] Tom Regan, editor.
Animal Sacrifices. Religious Perspectives on the Use of Animals in Science.
Temple University Press, 1986.

[139] R S Reneman, T Arts, and A P G Hoeks.
Wall shear stress - an important determinant of endothelial cell function and structure - in the arterial system in vivo. discrepancies with theory.
Journal of Vascular Research, 43(3):251–269, 2006.

[140] O Reynolds.
On the dynamical theory of incompressible viscous fluids and the determination of the criterion.
Philosophical Transactions, 186:123–164, 1895.

[141] O Robinson and D Rockwell.
Construction of three-dimensional images of flow structure via particle tracking techniques.
Experiments in Fluids, 14:257–270, 1993.

[142] Martin Rosenbruch.
The sensitivity of chicken embryos in incubated eggs.
ALTEX, 14(3):111–113, 1997.

[143] J G Santiago, S T Wereley, C D Meinhart, D J Beebe, and R J Adrian.
A particle image velocimetry system for microfluidics.
Experiments in Fluids, 25:316–319, 1998.

[144] G W Schmid-Schoenbein and B W Zweifach.
RBC velocity profiles in arterioles and venules of the rabbit omentum.
Microvascular Research, 10(2):153–164, 1975.

[145] R Schmidt and G Thews, editors.
Human Physiology.
Springer, 1987.

[146] W Seidl, M Schulze, G Steding, and D Kluth.
A few remarks on the physiology of the chick embryo heart (Gallus gallus).
Folia Morphologica, 29(3):237–342, 1981.

[147] A Serov, W Steenbergen, and F de Mul.
Laser Doppler perfusion imaging with a complimentary metal oxide semiconductor image sensor.
Optics Letters, 27(5):300–302, 2002.

[148] A Serov, B Steinacher, and T Lasser.
Full-field laser Doppler perfusion imaging and monitoring with an intelligent CMOS camera.
Optics Express, 13(10):1681–1689, 2005.

[149] K Shirai, T Pfister, L Büttner, J Czarske, H Müller, S Becker, H Lienhart, and F Durst.
Highly spatially resolved velocity measurements of a turbulent channel flow by a fiber-optic heterodyne laser-doppler velocity-profile sensor.
Experiments in Fluids, 40:473–481, 2006.

[150] Z P Shul'man, L V Markova, and A A Makhanek.
Rheological factor and Fahraeus-Lindquist effect.
Journal of Engineering Physics and Thermophysics, 68(3):353–363, 1995.

[151] J R Singer.
Blood flow rates by nuclear magnetic resonance imaging.
Science, 130:1652–1653, 1959.

[152] J R Singer and L E Crooks.
Nuclear magnetic resonance blood flow measurements in the human brain.
Science, 221(4611):654–656, 1983.

[153] A K Singh, E B Cummings, and D J Throckmorton.
Fluorescent liposome flow markers for microscale particle-image velocimetry.
Analytical Chemistry, 73(5):1057–1061, 2001.

[154] M Singh and B Prakash.
Analysis of blood flow field in glass capillaries and in vivo microvessels by axial tomographic and image velocimetry techniques.
In Dieter Liepsch, editor, *VDI-Fortschrittsberichte*, volume 17 of *Biotechnik*, pages 239–253, Munich, Germany, 1994. VDI Verlag.

[155] N J Sissman.
Developmental landmarks in cardiac morphogenesis: comparative chronology.
American Journal of Cardiology, 25:141–148, 1970.

[156] D W Slaaf, G J Tangelder, and R S Reneman.
Rheological behavior of blood platelets in vivo.
Biorheology, 1(Suppl.):145–149, 1984.

[157] M A Smith.
The measurement and visualisation of vessel blood flow by magnetic resonance imaging.
Clinical Physics and Physiological Measurement, 11(2):101–123, 1990.

[158] M L Smith, D S Long, E R Damiano, and K Ley.
Near-wall micro-PIV reveals a hydrodynamically relevant endothelial surface layer in venules in vivo.
Biophysical Journal, 85(1):637–645, 2003.

[159] S W Stone, C D Meinhart, and S T Wereley.
A microfluidic-based nanoscope.
Experiments in Fluids, 33:613–619, 2002.

[160] Y Sugii, S Nishio, and K Okamoto.
In vivo PIV measurement of red blood cell velocity field in microvessels considering mesentery motion.
Physiological Measurement, 23(2):403–416, 2002.

[161] Y Sugii, S Nishio, and K Okamoto.
Measurement of a velocity field in microvessels using a high resolution PIV technique.
Annals of the New York Academy of Sciences, 972:331–336, 2002.

[162] R Tabrizchi and M K Pugsley.
Methods of blood flow measurement in the arterial circulatory system.
Journal of Pharmacological and Toxicological Methods, 44(2):375–384, 2000.

[163] G J Tangelder, H C Teirlinck, D W Slaaf, and R S Reneman.
Distribution of blood platelets flowing in arterioles.
American Journal of Physiology, 248(3 Pt 2):H318–H323, 1985.

[164] G J Tangelder, D W Slaaf, A M Muijtjens, T Arts, M G oude Egbrink, and R S Reneman.
Velocity profiles of blood platelets and red blood cells flowing in arterioles of the rabbit mesentery.
Circulation Research, 59(5):505–514, 1986.

[165] G J Tangelder, D W Slaaf, T Arts, and R S Reneman.
Wall shear rate in arterioles in vivo: least estimates from platelet velocity profiles.
American Journal of Physiology, 254(6 Pt 2):H1059–H1064, 1988.

[166] J N Topper and M A Gimbrone Jr.
Blood flow and vascular gene expression: fluid shear stress as a modulator of endothelial phenotype.
Molecular Medicine Today, 5(1):40–46, 1999.

[167] J W Trevan.
The viscosity of blood.
Biochemical Journal, 12:60–71, 1918.

[168] C Tropea.
Laser doppler anemometry: recent developments and future challenges.
Measurement Science and Technology, 6:605–619, 1995.

[169] K Tsukada, H Minamitani, E Sekizuka, and C Oshio.
Image correlation method for measuring blood flow velocity in microcirculation: correlation 'window' simulation and in vivo image analysis.
Physiological Measurement, 21(4):459–471, 2000.

[170] W S Uijttewaal, E J Nijhof, P J Bronkhorst, E Den Hartog, and R M Heethaar.
Near-wall excess of platelets induced by lateral migration of erythrocytes in flowing blood.
American Journal of Physiology, 264(4 Pt 2):H1239–1244, 1993.

[171] W S Uijttewaal, E J Nijhof, and R M Heethaar.
Lateral migration of blood cells and microspheres in two-dimensional Poiseuille flow: a laser-Doppler study.
Journal of Biomechanics, 27(1):35–42, 1994.

[172] N T C Ursem, P C Struijk, R E Poelmann, A C Gittenberger-de Groot, and J W Wladimiroff.
Dorsal aortic flow velocity in chick embryo of stage 16 to 28.
Ultrasound in Medicine & Biology, 27(7):919–924, 2001.

[173] B M van den Berg, H Vink, and J A E Spaan.
The endothelial glycocalyx protects against myocardial edema.
Circulation Research, 92(6):592–594, 2003.

[174] M van Dyke.
Extended Stokes series: laminar flow through a loosely coiled pipe.
Journal of Fluid Mechanics, 86:129–145, 1978.

[175] P Vennemann, K T Kiger, R Lindken, B C W Groenendijk, S Stekelenburg-de Vos, T L M ten Hagen, N T C Ursem, R E Poelmann, J Westerweel, and B P Hierck.
In vivo micro particle image velocimetry measurements of blood-plasma in the embryonic avian heart.
Journal of Biomechanics, 39:1191–1200, 2006.

[176] P Vennemann, R Lindken, and J Westerweel.
In vivo whole-field blood velocity measurement techniques.
Experiments in Fluids, 42:495–511, 2007.

[177] A C Völker, P Zakharov, B Weber, A Buck, and F Scheffold.
Laser speckle imaging with an active noise reduction scheme.
Optics Express, 13:9782–9787, 2005.

[178] A J Ward-Smith.
Internal fluid flow.
Clarendon Press, 1980.

[179] K Wårdell, A Jakobsson, and GE Nilsson.
Laser Doppler perfusion imaging by dynamic light scattering.
IEEE Transactions on Biomedical Engineering, 40(4):309–316, 1993.

[180] H Wayland.
Rheology and the microcirculation.
Gastroenterology, 52(2):342–355, 1967.

[181] J Westerweel.
Fundamentals of digital particle image velocimetry.
Measurement Science and Technology, 8:1379–1392, 1997.

[182] J Westerweel.
On velocity gradients in PIV interrogation.
Experiments in Fluids, page online first, 2007.
doi: 10.1007/s00348-007-0439-3.

[183] J Westerweel and F Scarano.
Universal outlier detection for PIV data.
Experiments in Fluids, 39:1096–1100, 2005.

[184] M C Woodle and D D Lasic.
Sterically stabilized liposomes.
Biochimica et Biophysica Acta, 1113(2):171–199, 1992.

[185] H Yanagisawa, R E Hammer, J A Richardson, S C Williams, D E Clouthier, and M Yanagisawa.
Role of endothelin-1/endothelin-A receptor-mediated signaling pathway in the aortic arch patterning in mice.
The Journal of Clinical Investigation, 102:22–33, 1998.

[186] H Yanagisawa, M Yanagisawa, R P Kapur, J A Richardson, S C Williams, D E Clouthier, D de Wit, N Emoto, and R E Hammer.
Dual genetic pathways of endothelin-mediated intercellular signaling revealed by targeted disruption of endothelin converting enzyme-1 gene.
Development, 125(5):825–836, 1998.

[187] S Yuan, A Devor, D A Boas, and A K Dunn.
Determination of optimal exposure time for imaging of blood flow changes with laser speckle contrast imaging.
Applied Optics, 44(10):1823–1830, 2005.

[188] M Zamir and E L Ritman.
The Physics of Pulsatile Flow.
American Institute of Physics, 2000.

[189] H Zhao, R H Webb, and B Ortel.
Review of noninvasive methods for skin blood flow imaging in microcirculation.
Journal of Clinical Engineering, 40(1):40–47, 2002.

[190] H Zheng, O Mukdadi, H Kim, J R Hertzberg, and R Shandas.
Advantages in using multifrequency excitation of contrast microbubbles for enhancing echo particle image velocimetry techniques: initial numerical studies using rectangular and triangular waves.
Ultrasound in Medicine & Biology, 31(1):99–108, 2005.

[191] H Zheng, L Liu, L Williams, J R Hertzberg, C Lanning, and R Shandas.
Real time multicomponent echo particle image velocimetry technique for opaque flow imaging.
Applied Physics Letters, 88:261915(1)–261915(3), 2006.

Acknowledgments

Although being responsible for the content of this thesis, I can not consider it to be my work alone. A bit simplified, my main contribution to the progress described in this thesis was to convert diffuse input into concentrated output. In the Laboratory for Aero- and Hydrodynamics I was lucky to be part of a very fertile environment that always provided a lot of high quality input. This is not only true because of the composition of the group, but also because the laboratory is part of the J. M. Burgerscentre (JMBC), and because it is carefully embedded in a valuable network of scientific relations with other research groups. Therefore I first want to thank those people who created and constantly maintain this environment.

One of these persons was Frans Nieuwstadt, who unfortunately is not with us anymore. He took care of maintaining a professionally well-balanced, and multicultural group of researchers. He also initiated the co-operation with the Department of Anatomy and Embryology, Leiden University MC, and the Department of Obstetrics and Gynecology, Erasmus MC in Rotterdam, which was essential for my work. Here I also want to thank Rob Poelmann and Nicolette Ursem who represent the co-operating departments. The person I have to thank most is my promoter Jerry Westerweel. To me, Jerry always appears to be an inexhaustible source of ideas. He continued to develop our group and substantially expanded the communication with other research centers like the Department for Experimental Surgical Oncology, and the Thoraxcenter (both Erasmus MC), the Department for Medical Physics (Amsterdam MC), and the Department of Biophysics of the University in Maastricht. Again, I do not want to forget to thank the persons who represent those groups. These are Timo ten Hagen, Rob Krams, Hans Vink, and Rob Reneman, respectively. Also the JMBC, represented by Gijs Ooms, plays an essential part in the development of the scientific environment I benefited of. Activities of the JMBC established contacts to the groups of Frans van der Vosse (Biomechanics and Tissue Engineering, Technical University of Eindhoven), Anton van Steenhoven (Mechanical Engineering, Technical University of Eindhoven), and Michel Versluis (Physics of Fluids Group, University of Twente). These contacts and the JMBC training program certainly left their traces in this thesis.

The JMBC also enabled the stay of Ken Kiger (Mechanical Engineering, University of Maryland) in our group during his sabbatical. Ken is substantially responsible for the good start of this project and the early preparation of the publication for the Journal of Biomechanics [175]. His dedicated and professional way of working still

serves as an example to me. Barely less important for the success of the presented measurements was the engagement of Beerend Hierck (Anatomy and Embryology, Leiden University MC). Beerend's input always lead to noticeable progress. He was around when needed and, as Ken, spent a remarkable amount of time in our dark and tiny micro particle image velocimetry laboratory.

I am particularly indebted to Bianca Groenendijk, Kim van der Heiden (both from the Department for Anatomy and Embryology, Leiden University MC), and Els Bon (from the Department for Obstetrics and Gynecology, Erasmus MC) who spent many days together with me at the micro particle image velocimetry set-up. Thank you for literally "getting up with the chickens", commuting to Delft, and transporting whole laboratory equipments with your cars. Above all, I thank you for your skilled preparation of the embryos and your patience with me. At this point I also would like to thank Nicolette Ursem and Sandra Stekelenburg-de Vos (Obstetrics and Gynecology, Erasmus MC), as well as Timo ten Hagen (Experimental Surgical Oncology, Erasmus MC) for making a lot of valuable laboratory equipment available to us, like a microscope and the ultrasound Doppler velocimeter. Special thanks goes to Ann Seynhaeve (Experimental Surgical Oncology, Erasmus MC) for preparing the liposomal formulations that were used for the measurements published in the Journal of Biomechanics [175].

Many more people will find their influence on this work back in the thesis. By explaining things to me, giving hints or just asking questions, Mathieu Pourquie, René Delfos, and especially Ralph Lindken certainly belong to the major contributors to this work. Thank you René for patiently listening to my first attempts to explain something in Dutch. This thesis would also look different without the LabView programming and equipment maintenance of Wilco Tax. I also thank Cor Gerritsen for solving many problems with electronics, especially when ad hoc solutions had to be implemented, because the embryos could not wait. I also would like to thank Joop Bodde for his helpfulness in the workshop, and the team of secretaries Ria van der Brugge-Peeters, Caroline Legierse, and Jamina for their countless support beginning from finding a room for me as I started my PhD, to the organization of the paperwork for the defense just a few weeks ago. I am also grateful to Bernd Wieneke and Uwe Dierksheide (LaVision) for their support and the possibility to test various cameras. I also will not forget Monica Mentink, who taught me how to do injections into a vitelline vein of a HH-stage 17 chicken embryo, and Ina Ekeberg who prepared her excellent masters thesis in the scope of this project. Here I also want to thank Thomas Ooms for proofreading my "samenvatting".

I do not want to miss the occasion to mention that I am very happy that Christian Poelma took this project over and continues the measurements together with Kim van der Heiden and Beerend Hierck. It is very satisfying to have written a thesis about research that is living on.

I also owe this unique time in the Netherlands to Franz Peters, my supervisor in Essen, who encouraged me to do a PhD, and to Ralph Lindken, who established the contact to Delft.

My period at the Laboratory for Aero- and Hydrodynamics was accompanied by colleagues and friends who made this time worth living. Worrying to omit someone accidentally I rather would like to stop here with listing names, but I am very happy that you have been my room mate, that we went to the pub together, enjoyed the atmosphere on the Beestenmarkt, went cycling, had BBQ's in your backyard, or in the Delftse Hout, that we went to the painting course of the Cultureel Centrum, saw movies together, played cards, mixed cocktails, that you invited me to your home, showed me your village in Zeeland, that we listened to jazz music in Kijkduin, that we went to the beach together, that you dropped by to have a chat, that you took me to that special restaurant, thanks for the walk on Mount Lowe, or on the island Storholmen, I enjoyed to play snooker with you, and proving your special liqueur, I was happy to be invited to your wedding, and impressed that you came along all the way from Germany, Denmark, and Austria to visit me in Holland.

I am grateful to my parents who gave me all the support they could give.

Finally I want to thank Kirsten for all her love and patience, especially during the last months while I spent evenings and weekends to finish this text.

About the Author

Peter Vennemann,
born on Monday, August 12, 1974
in Ascheberg (Westphalia), Germany

since 2007	RWE-Power AG Renewable Power Generation, Essen
2003 - 2007	Delft Technical University Lab. for Aero- and Hydrodynamics PhD thesis: Particle Image Velocimetry for Microscale Blood Flow Measurements
2002 - 2003	University Duisburg-Essen, Fluidmechanics research contract: Modelluntersuchungen zur Bestimmung des Volumenstroms in systemisch-pulmonalen arteriellen Shunts
1996 - 2002	University Duisburg-Essen diploma thesis (mechanical engineering): Simulation und experimentelle Überprüfung der homogenen Tropfenkondensation und -verdampfung in einer zylindrischen Kammer second semester paper: Erzeugung eines pulsenden Fluidstromes zur experimentellen Untersuchung von Lungenfisteln first semester paper: Topographical Measurements of Water Waves at a Matrix of Measuring Points Heriot Watt University Fluid Loading and Instrumentation Centre, Edinburgh
1995 - 1996	alternative service in a kindergarten, Münster
1994 - 1995	technical secondary school, Münster
1991 - 1994	Schlering GmbH, Drensteinfurt apprenticeship as a heating mechanic
1985 - 1991	secondary school, Ascheberg

journal publications

C Poelma, P Vennemann, R Lindken, J Westerweel
In vivo blood flow and wall shear stress measurements in the vitelline network
Experiments in Fluids, online first, 2008
DOI:10.1007/s00348-008-0476-6

BCW Groenendijk, S Stekelenburg-de Vos, P Vennemann, JW Wladimiroff, FTM Nieuwstadt, R Lindken, J Westerweel, BP Hierck, NTC Ursem, and RE Poelmann
The endothelin-1 pathway and the development of cardiovascular defects in the hemodynamically challenged chicken embryo
Journal of Vascular Research, 45:54-68, 2008

P Vennemann, R Lindken, J Westerweel
In vivo whole-field blood velociy measurement techniques
Experiments in Fluids, 42:595-511, 2007

P Vennemann, KT Kiger, R Lindken, BCW Groenendijk, S Stekelenburg-de Vos, TLM ten Hagen, NTC Ursem, RE Poelmann, J Westerweel and BP Hierck
In vivo micro particle image velocimetry measurements of blood-plasma in the embryonic avian heart
Journal of Biomechanics, 39(7):1191-1200, 2006

conference contributions and unrefereed articles

C Poelma, P Vennemann, K van der Heiden, R Lindken, BP Hierck, J Westerweel
Wall shear stress measurements using microPIV in the outflow tract of a chick embryo
14^{th} International Symposium on Applications of Laser Techniques to Fluid Mechanics, Lisbon, Portugal, 7-10 July, 2008

C Poelma, P Vennemann, R Lindken, J Westerweel
In vivo measurements of blood flow in the vitelline network
Proceedings of the 60^{th} Annual Meeting of the Division of Fluid Mechanics APS-DFD, Abstract BD.01, Salt Lake City, UT, USA, November 18-20, 2007

P Vennemann, M Pourquie, R Lindken, J Westerweel
Blood velocity measurement in microvessels
JMBC 15 years, 274-275, 2007

C Poelma, P Vennemann, R Lindken, J Westerweel
In vivo blood flow velocity measurements in the vitelline network
7^{th} International Symposium on Particle Image Velocimetry, Rome, Italy, September 11-14, 2007

C Poelma, P Vennemann, R Lindken, J Westerweel
Flow studies in a vitelline vessel network
Second symposium on Biomechanics in Cardiovascular Disease: Shear Stress in Vascular Biology. Rotterdam, Netherlands, April 19-20, 2007

P Vennemann, R Lindken, J Westerweel
In vivo micro-PIV measurements in the embryonic chicken heart
PivNet2 Final Workshop, Göttingen, Germany, September 7-8, 2006

R Lindken, M Rossi, I Ekeberg, P Vennemann, BP Hierck, J Westerweel
In vitro Messung der Wandschubspannungsverteilung auf einer Endothel Zellschicht mittels Micro Particle Image Velocimetry (μPIV)
14. Fachtagung Lasermethoden in der Strömungsmesstechnik, GALA, Braunschweig, Germany, September 5-7, 2006

P Vennemann, R Lindken, J Westerweel
Multi-plane Particle Image Velocimetry im embryonalen Hühnerherzen
14. Fachtagung Lasermethoden in der Strömungsmesstechnik, GALA, Braunschweig, Germany, September 5-7, 2006

P Vennemann, R Lindken, BP Hierck, J Westerweel
Volumetric particle image velocimetry in the developing chicken heart
Journal of Biomechanics, 39(Suppl 1):S616, 2006

M Pourquie, F Nieuwstadt, P Vennemann, J Westerweel, R Lindken, R Poelmann, BCW Groenendijk, BP Hierck, S Stekelenburgh-de Vos
Flow and blood shear stress in a chicken embryonic heart, experiments and numerical modeling
Journal of Biomechanics, 39(Suppl 1):S405, 2006

R Lindken, M Rossi, BP Hierck, P Vennemann, J Westerweel
Measurement of shear stress on endothelium in a flow chamber and its gene expression response
Journal of Biomechanics, 39(Suppl 1):S302, 2006

P Vennemann, R Lindken, J Westerweel
Hemodynamics of the embryonic chicken heart
EUROMECH Fluid Mechanics Conference 6, Stockholm, Sweden, June 26-30, 2006

M Rossi, I Ekeberg, P Vennemann, R Lindken, J Westerweel, BP Hierck, EP Tomasini
In vitro study of shear stress over endothelial cells by micro-particle image velocimetry
13th International Symposium on Applications of Laser Techniques to Fluid Mechanics, Lisboa, Portugal, 26-29 June, 2006

P Vennemann, M Pourquie, J Westerweel
Blood flow measurements in micro vessels
ERCOFTAC Bulletin 68:17-19, 2006

I Ekeberg, M Rossi, P Vennemann, R Lindken, J Westerweel
Micro Particle Image Velocimetry (μPIV) in an endothelial flow chamber
1^{st} Mini Symposium Lab-on-Microchip, book of abstracts p31, Siegen, Germany, 2005

P Vennemann, KT Kiger, NTC Ursem, TLM ten Hagen, S Stekelenburg-de Vos, BCW Groenendijk, R Lindken, RE Poelmann, J Westerweel, BP Hierck
In vivo micro PIV in the embryonic avian heart
6^{th} International Symposium on Particle Image Velocimetry, Pasadena, USA, September 21-23, 2005

M Pourquie, FTM Nieuwstadt, P Vennemann, J Westerweel, R Lindken, R Poelmann, BCW Groenendijk, BP Hierck, S Stekelenburg-DeVos, NTC Ursem
Blood shear stress in a chicken embryo, experiments and numerical modeling
Turbulent and Shear Flow Phenomena, 2005

P Vennemann and J Westerweel
Full-Field Blood Velocity Measurement Techniques
in: Tomasz A. Kowalewski (ed.). ABIOMED Lecture Notes 6, Blood Flow Modelling and Diagnostics
IPPT PAN, CoE ABIOMED, Warsaw, Poland 91-108, 2005

PB Hierck, BCW Groenendijk, S Stekelenburg-De Vos, M Pourquie, R Lindken, P Vennemann, KT Kiger, J Westerweel, NTC Ursem, FTM Nieuwstadt, AC Gittenberger-De Groot, RE Poelmann
A combined technical and biological approach to link physiological and genetic data to cardiovascular development
European Journal of Morphology, 42(3):143-161, 2005

BP Hierck, BCW Groenendijk, S Stekelenburg-de Vos, P Vennemann, M Baiker, R Lindken, M Pourquie, NTC Ursem, KT Kiger, J Westerweel, F Nieuwstadt, AC Gittenberger-de Groot, RE Poelmann
Cardiovascular Development Controlled by Fluid Shear Stress. A Functionomic Approach
Journal of Vascular Research, 42(Suppl.2):9, 2005

P Vennemann, KT Kiger, BP Hierck, NTC Ursem, TLM ten Hagen, S Stekelenburg-de Vos, BCW Groenendijk, R Lindken, RE Poelmann, J Westerweel
In vivo micro PIV in the embryonic avian heart
Joint International PIVNET II / ERCOFTAC Workshop on Micro PIV and Applications in Microsystems, Delft, The Netherlands, April 7-8, 2005

BCW Groenendijk, S Stekelenburg-de Vos, P Vennemann, M Pourquie, R Lindken, K van der Heiden, NTC Ursem, AC Gittenberger-de Groot, FTM Nieuwstadt, KT Kiger, J Westerweel, R Poelmann, BP Hierck
Shear stress envisioned: a link between blood flow and cardiovascular development
Abstracts of the 15th Endothelial Cell Research Symposium, p175, 2004

R Lindken, PF Geelhoed, C Rops, P Vennemann, J Westerwee
μ-PIV and Heat Transfer Measurements in Microchannels
Proceedings of the International Workshop on Size Effects in Microfluidics and Micro Heat Transfer. Fundamental and Practical Aspects, Kielce, Poland, 2004

R Lindken, P Vennemann, KT Kiger, BP Hierck NTC Ursem, S Stekelenburg-deVos, TLM tenHagen, RE Poelmann, J Westerweel
In vivo Micro Particle Image Velocimetry (μ-PIV) Messungen in dem Herzen eines Hühnerembryos
12. Fachtagung "Lasermethoden in der Strömungsmechanik", book of abstracts, p 40.1-40.7, Karlsruhe, Germany, September 7-9, 2004

P Vennemann, KT Kiger, BP Hierck, NTC Ursem, S Stekelenburg-de Vos, RE Poelmann, TLM ten Hagen, R Lindken, J Westerweel, BCW Groenendijk
In vivo PIV measurments in the embryonic chicken heart
Euromech Colloquium 456: Experimental and computational biofluid mechanics, Aachen, October 4, 2004

P Vennemann, KT Kiger, BP Hierck, NTC Ursem, TLM ten Hagen, J Westerweel
In vivo PIV measurements in the embryonic chicken heart
XXI International Congress of Theoretical and Applied Mechanics, Warsaw, August 15-21, 2004

K Kiger, P Vennemann, R Lindken, J Westerweel, BP Hierck, B Groenendijk, RE Poelmann, NTC Ursem, S Stekelenburg-de Vos, TLM ten Hagen
Development of in vivo PIV methods for measurement of wall shear stress in embryonic animal models
57th Annual Meeting of the APS Division of Fluid Dynamics, Seattle, Washington, November 21-23, 2004

BP Hierck, BCW Groenendijk, P Vennemann, R Lindken, M Pourquie, S Stekelenburg-De Vos, NTC Ursem, K Kiger, J Westerweel, FTM Nieuwstadt, AC Gittenberger-De Groot, RE Poelmann
Fluid shear stress in cardiovascular development. The challenge of linking physics to genetics
Cardiovascular Pathology, 13(3S) 187, 2004

R Lindken, P Vennemann, J Westerweel, NTC Ursem, S Stekelenburg-de Vos, RE Poelmann
In vivo micro-PIV measurements in the embryonic avian heart
Bulletin of the American Physical Society, 48(10):226-227, 2003

Index

3d-reconstruction, 57
  discretization error, 58
  random noise, 58
  spatial averaging, 58

bio-fluid mechanics, 1
blood, 9, 10
  aggregation, 9, 12
  rouleaux, 9, 10
  viscosity, 10, 12, 13
    scaling, 15
  yield stress, 15

camera, 38
  interframing time, 39
  quantum efficiency, 39
chicken embryo, 35, 36
cross-correlation, 25, 39

Dean number, 69, 70
depth of correlation, 54, 55
dichroic mirror, 38
diffuser plate, 40
divergence, 57

endothelial cells, 11
ensemble correlation, 48, 64
erythrocytes, 9
  avian, 12

fibrinogen, 11
frog, 26
Fåhraeus-Lindquist effect, 10

glycocalyx layer, 11, 28

Hamburger and Hamilton, 35
hematocrit value, 9

illumination, 39

keyword query, 1, 2
Kleiber's quarter power law, 3

laser
  beam waist, 19, 22
  coherence, 40
  Gaussian wave fronts, 21, 22
  impact on organic system, 40
  speckle, 22
    far-field speckle, 24
    image speckle, 22
laser Doppler velocimetry, 18
  laser Doppler imagers, 19
  multi-probes, 20, 21
  profile sensor, 21
  scanning, 19
laser speckle contrast imaging, 22, 23
leukocytes, 10
life expectancy, 3
light
  penetration depth, 18, 40
light sensitivity, 38
linear regression, 60

Michelson interferometer, 24
microscope, 36
mineral oil, 36

nuclear magnetic resonance imaging, 30

optical flow, 25

particle image velocimetry, 25
  biomedical research, 35
  micro scale, 25

stereoscopic, 26, 56
tomographic, 55, 56
ultrasound, 30
particle tracking, 25
phase velocity cine magnetic resonance imaging, 31
phosphate buffered saline, 36
photoablative effects, 41
photochemical effects, 41
planapochromat, 37
platelets, 10
polarization spectral imaging, 17
polyethylene-glycol, 43
positron emission tomography, 17

radionuclide perfusion imaging, 17
Rayleigh length, 19
red blood cells, 9
Reynolds number, 14

seeding, 41
single photon emission computed tomography, 17
spin wash-out, 31

terahertz imaging, 32
thrombocytes, 10
time-varying speckle, 23
tracer particles
artificial, 41
erythrocytes, 28, 41
fluorescent, 32
gas bubbles, 30
thrombocytes, 41
triggering, 39, 46

ultrasound Doppler velocimetry, 46

venous clip model, 69

wall shear stress, 4
white blood cells, 10
Womersley number, 14

zebrafish, 29

ISBN 978-90-9022974-4